UNIVERSIDADE DE LISBOA
INSTITUTO SUPERIOR TÉCNICO
Università degli Studi di Padova

Tokamak Magnetic Control Simulation: Applications for JT60-SA and ISTTOK Operation.

Doménica Corona Rivera

Supervisor:Prof. Horácio Fernandes
Co-Supervisor: Prof. Nuno Cruz
External supervisor: Prof. Alfredo Pironti

Thesis specifically prepared to obtain the PhD Degree in
Technological Physics Engineering

Month 2020

ABSTRACT

Abstract en ingles

Keywords:Real-time control, plasma current, centroid position, state-space

RESUMO

Abstract em tuga

Palavras-chave:

SOMMARIO

Abstract em italiano

Parole chiave:

ACKNOWLEDGEMENTS

This work was supported by Fundação para a Ciência e a Tecnologia (FCT) under the grant No.**PD/BD/114306/2016** carried out as part of the training in the framework of the Advanced Program in Plasma Science and Engineering (APPLAuSE, sponsored by FCT under grant No. PD/00505/2012).

CONTENTS

LIST OF FIGURES

LIST OF TABLES

LIST OF ABBREVIATIONS

- AC - Alternating Current
- ADC - Analog to Digital Converter
- ATCA - Advanced Telecommunications Computing Architecture
- CCS- Couchy Condition Surface
- CREATE - Consorzio di Ricerca per l'Energia, l'Automazione e le Tecnologie dell'Elettromagnetismo
- DDB - Dynamic Data Buffer
- DAC - Digital to Analog Converter
- ELM - Edge Localized Mode
- EO - Electronic Offset
- GAM - Generic Application Module
- IST - Instituto Superior Técnico
- JET - Joint European Torus
- LCFS- Last Closed Flux Surface
- LQR - Linear Quadratic Regulator
- MARTe - Multi-threaded Application Real-Time executor
- MIMO - Multiple-Input Multiple-Output
- PCS - Plasma Control System
- PF - Poloidal Field
- PID - Proportional - Integrative - Derivative
- QST - National Institutes for Quantum and Radiological Science and Technology
- RAPTOR - RApid Plasma Transport simulatOR
- RFM - Reflective Memory
- RMSE - Root Mean Squared Error

- SISO- Single-Input Single-Output
- SCD - Systéme de Contrôle Distribué
- SOF - Start Of Flattop
- XSC - eXtreme Shape Controller
- WO - Wiring Offset

LIST OF VARIABLES

@TODO: Review variable lists as writing the thesis

VARIABLES:

- I_p - Plasma current
- B_p - Poloidal magnetic field
- μ_0 - Vacuum permeability
- β_p - Poloidal beta
- l_i - Internal inductance
- I_{PF} - Poloidal Field coils current

1

INTRODUCTION

1.1 TOKAMAK PLASMA CONTROL

1.2 BEHIND THE PLASMA CURRENT

1.3 THESIS OUTLINE

2

PLASMA CONTROL SYSTEMS

2.1 OVERVIEW OF CONTROL SYSTEMS

The control of plasma position, shape and current among other parameters is one of the essential engineering problems for present and future magnetic confinement devices. The Plasma Control Systems (PCS) lead with the overall control of fusion devices being responsible also for the plasma configuration and scenarios algorithms [1, Chapter 8]. Even thought this entire work mainly focuses on position and shape control it is also important to mention the relevance of density control for tokamak operation for the gas feeding feedback [2]. Industrial control systems in fusion devices like water cooling and power supply control usually are controlled outside the domain of the PCS. Currently different PCS's are use in the tokamaks around the world. In this chapter the "DIII-D-like" PCS, the Systéme de Contrôle Distribué (SCD) and the Multi-threaded Application Real-Time executor (MARTe) will be approach, this last one being of special interest due to its extensive utilization in this work, likewise this chapter presents an overview of the equilibrium and control algorithms used for the reconstruction of plasma parameters and the controllers use for position,shape and plasma current among other parameters.

2.1.1 *DIII-D Plasma Control System*

The DIII-D-like PCS is use in various fusion research facilities such as EAST (China), K-STAR (South Korea), NSTX (USA) and MAST (UK). Early documentation regarding the PCS in DIII-D[1] reefers to digitalization of analog signals transmitted to a high speed processor executing a shape control algorithm and then writing the result to a digital to analog converter for driving the controlled systems . The real-time computer used allowed to performed operations with vectors and matrices required for the plasma shape control algorithm [3]. Figure 2.1 shows the block diagram of the DIII-D PCS 30 years ago.

In recent years the DIII-D PCS had extensive software and hardware upgrades. The PCS actual software consists of an infrastructure library core which provides all the routines that are necessary for implementing a basic and generic control system. The current PCS hardware configuration uses a collection of Intel Linux based multi-processor computers running in parallel to perform the real-

1 DIII-D is a D-shape tokamak operated by General Atomics in San Diego, California.

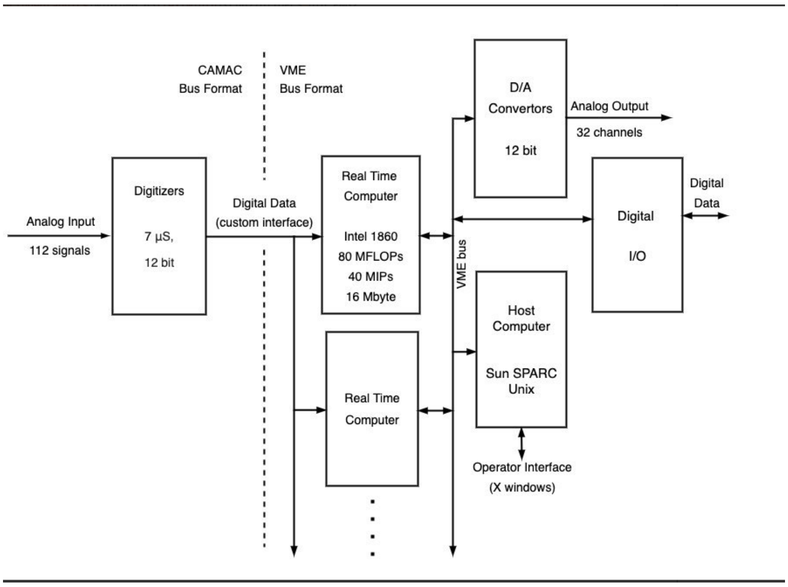

Figure 2.1.: DIII-D digital PCS in 1991 [3].

time analysis and feedback control [4]. New digitizers have been added to the real-time network to increase the number of signals acquired an to control hardware on real-time, several real-time control algorithms were added and real-time data was added to external entities such as web server. [5]. In the current version of the PCS, a Myricom[2] network has been replaced with a 40 Gb/sec InfiniBand[3] network based on the Mellanox Connect-X 3[4] hardware set. Figure 2.2 shows the currently overall networking diagram of DIII-D PCS .

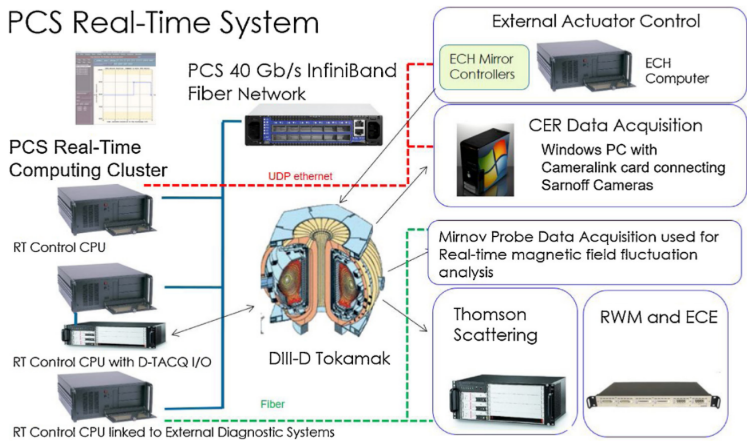

Figure 2.2.: Actual DIII-D PCS real-time systems [5].

2 Myricom networks also called Myrnet are high speed networking systems used to interconnect machines to form computer clusters.
3 Is a network architecture from Mellanox designed to support I/O connectivity and reliability, availability, and serviceability Internet requirements [6].
4 The Connect-X from the Mellanox company are Ethernet network interface cards with PCI Express.

2.1.2 *Systéme de Contrôle Distribué*

The TCV[5] distributed control system uses a modular network of real time PC nodes liken by a real time network to provide feedback control over all of the actuator systems. Each node consists of a Linux PC either embedded on a Compact-PCI module or as a desktop computer with Intel CPU. A fiber optic ring network links the reflective memory (RFM) network cards in each node [7]. The design of the diagnostic signal processing and control algorithms is performed in Matlab-Simulink software. During the real-time execution C/C++ code is generated from the Simulink and compiled into a Linux shared library and distributed to target nodes providing the input/output interface to the control algorithm code [8]. Figure 2.3 depicts the TCV SCD layout with the connectivity to diagnostics and actuators.

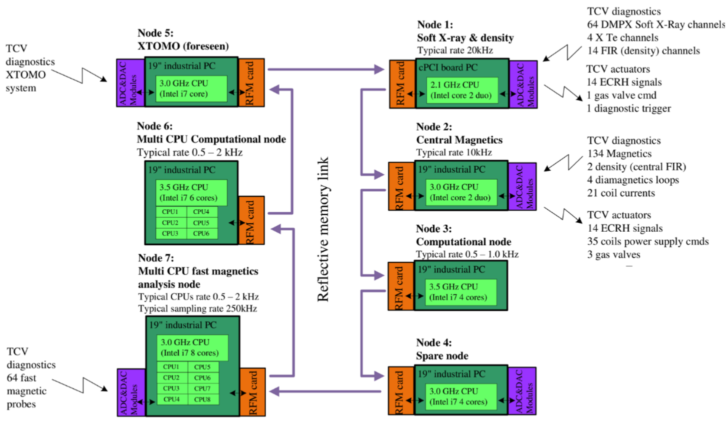

Figure 2.3.: TCV SCD. Real-time network nodes connection. The nodes configurations are shown together with the typical diagnostic and actuator systems to which they are connected [8].

2.2 MARTE FRAMEWORK

Regardless the nature of a real-time system, the design of it is usually related to the specific requirements it has, commonly this implies to have customized hardware and software which causes a lack in modularity and portability. When systems become bigger is convenient to provide a common library containing shareable functionalities and which also allows for modular implementations. In order to deal with this the MARTe framework was designed about a decade ago. MARTe was developed in order to standardize general real-time control systems for the execution of control algorithms and is based on a multiplatform C^{++} library [9]. Previous implementations for a software framework similar to MARTe were developed some years before for the JET tokamak. JETRT was a software framework used to develop real-time control and data acquisition systems which laid the foundation for current MARTe framework [10]. MARTe is currently used in several tokamaks such as JET, FTU, COMPASS and ISTTOK.

5 The Tokamak á configuration variable (TCV) is a medium size tokamak localized in Lausanne,Switzerland. It is characterized by a highly elongated, rectangular vacuum vessel.

2.2.1 *MARTe architecture*

The unitary MARTe component is the Generic Application Module (GAM), each of the C++ programmed GAMs usually performs an specific task of the control system, the collection of interconnecting GAMs builds MARTe [11]. The GAMs have an entry point to receive data driven configuration and a set of input and output channels to interface with other GAMs. The Dynamic Data Buffer (DDB) is a generic memory data bus where each GAM receives and produce data using DDB named channels. Usually each GAM is associated with a special function of the system like processing data of an specific diagnostic or perform some control algorithm. MARTe hardware data interface and synchronization for inputs and outputs is performed using a special GAM called IOGAM.

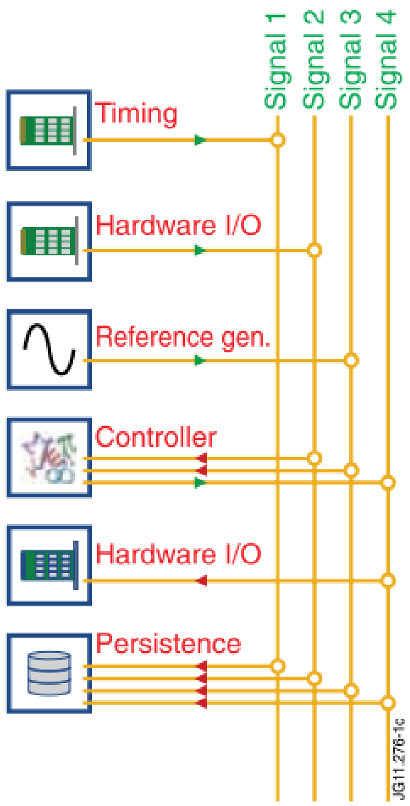

Figure 2.4.: Example of a set of GAMs connected to the DDB. Timing and hardware GAMs provide the I/O interface to the exterior, whereas a generic waveform GAM inputs the reference for a PID controller. Finally, the output is sent to a DAC and the data is stored for analysis by a collection GAM. It should be noticed that the reference generation and the controller GAM are not aware of the changes in the data providers and data consumers. [12]

2.2.2 *Hardware containers*

The MARTe hardware containers

2.2.3 *MARTe 2.0*

Software Quality Assurance (QA)[6] processes are being applied to the development of a new version of the MARTe framework also called MARTe 2.0. The main objective is to provide a QA certifiable environment from where it is possible to develop, with less effort, certifiable applications. The MARTe QA version can be easily adapted to the development of many types of software which are common in the fusion community, in particular for software related to control and data acquisition systems that is to be shared among different teams [14]. MARTe 2.0 will be the result of reduction exercise of the core framework based on the lessons learned from MARTe. This version will incorporate and implement an integral quality assurance process for the development of the framework (e.g. unit tests and coding standard) [15].

In order to develop robust code and to avoid common errors and pitfalls, a controlled subset of the C++ language must be defined for the MARTe framework. This subset will be define by means of a list of coding rules, which will address all dangerous aspects of the C++ language for critical systems. Thus, the C++ version used on MARTe will be defined by the standard ISO/IEC 14882:2003 aka as C++03, while the coding rules will be those defined by the standard MISRA C++:2008 [16]. The MARTe project manager is responsible for appointing a quality office (QO) for the QA process. The QO will guarantee that the QA activities are executed accordingly to the software development process, it will also conduct independent reviews and audit all data and processes involving the development, production and maintenance of MARTe deliverables [17]. The overall advantage of the new MARTe version is that the common faced difficulties of distributing and maintaining a software without the continuous support of the original developers will be overcome following a complete QA system.

2.3 TOKAMAK EQUILIBRIUM CODES

Tokamak equilibrium codes are used for retrieving information about plasma current, shape and position and pressures profiles among other parameters. Usually these codes use as input data as the machine geometry, the PF coils currents and the flux and magnetic field diagnostics measurements. The importance of these codes is that since some of the parameters necessary for an accurate feedback control are not directly measured from the diagnostics, these data has to be fitted on real-time somehow to the Grad-Shafranov equilibrium model [18]. In this section some of the most implemented and reported codes for tokamak plasma equilibrium reconstruction will be briefly described.

The EFIT (Equilibrium Fitting) code is used to efficiently reconstruct the current profile parameters, the plasma shape and a current density profile satisfying the MHD equilibrium constraint based on a

6 Software QA is a set of activities or processes that define and assess the adequacy of software processes to provide evidence that establishes confidence that the software processes are appropriate for and produce software products of suitable quality for their intended purposes [13, Chapter 5.1].

Picard iteration[7] approach which approximately conserves the external magnetic measurements [19]. EFIT has served as the de-facto standard technique to infer equilibrium from experimental diagnostics and there have been many different code implementations of this technique, all EFIT versions are able to solve the MHD force balance and most experiment-specific customizations are made for the addition of experimental constraints peculiar to the experiment being modelled [20]. EFIT reconstruction code is used in tokamaks such as DIII-D and the National Spherical Torus Experiment (NSTX). For the specific NSTX case they implemented a special real-time EFIT version called rtEFIT developed at General Atomics, the rtEFIT code provides the shape of the plasma boundary that is used as input to an isoflux control algorithm that generates voltage requests to the power supplies. The reconstruction of plasma boundaries in real-time compare well to those reconstructed using the EFIT code offline in between plasma discharges [21].

The RAPTOR (RApid Plasma Transport simulatOR) is a model-based control-oriented code that predicts tokamak plasma profile evolution on real-time, it predicts the evolutions of several parameters, thanks to its accurate yet simplified physics model [22]. The physical model of the plant is derived from a spatially discretized partial differential equation (PDE), yielding a nonlinear set of ordinary differential equations (ODEs) for which the derivatives are evaluated analytically by the RAPTOR code. One of the main RAPTOR features is that while the plasma is evolving RAPTOR has full knowledge of the plasma profiles and the available real-time diagnostic data can be included in a natural way to improve the accuracy of the estimation, in control engineering this approach is known as dynamic state observer and is used to estimate unmeasured or poorly states of a dynamical system [23]. This dynamic state observer consists on an extended Kalman filter which estimates an augmented state consisting of physical states and random-walk disturbances [24]. The concepts of states-space systems and Kalman filtering will be addressed in the next subsections. Figure 2.5 scheme shows the carries out integration of the RAPTOR code on top of the MARTe framework at the Italian tokamak RFX-mod.

For the case of JET a boundary reconstruction package called XLOC has been used to localized the X-point position and plasma boundary [25]. A newer code relying on XLOC called Equinox was designed and implemented in C++ using a finite element method and a non linear fixed point algorithm associated to a least square optimization procedure to reconstruct the plasma equilibrium in less than 50ms for the real-system [26].

The CREATE codes (CREATE-L [27] and CREATE-NL [28]) are equilibrium solvers that will be widely described in next chapter and its application for the plasma control shape and position in JT60-SA tokamak.

7 Picard iterations is a method based on successive approximations to obtained a set of conditions under which an initial value problem has a unique solution.

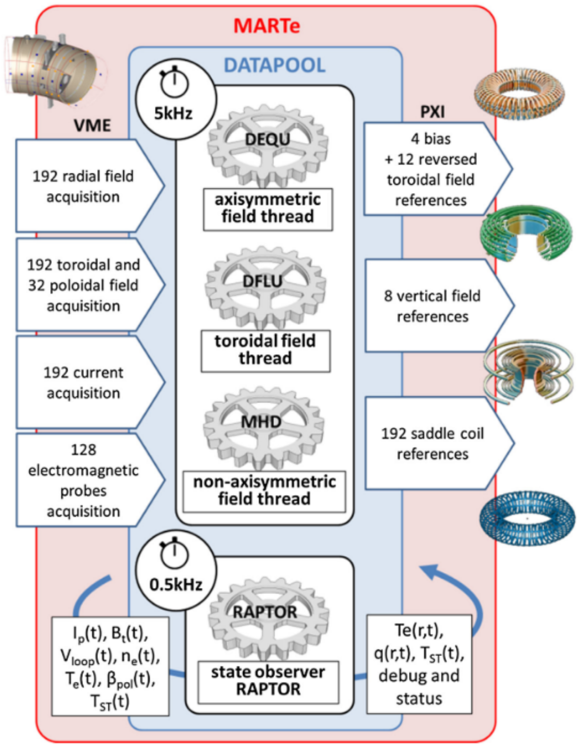

Figure 2.5.: Skectch of the integration of the state observer RAPTOR in the RFX-mod real-time control system based on the MARTe framework. experimental [22]

2.4 CONTROL TECHNIQUES AND STATE-SPACE MODELS

This section will summarize some systems dynamics and control concepts which will be applied on the next chapters. Applying a feedback control loop to a system brings a link between the output and input signals , this action corrects the error in between the system output and a desired set-point, eventually the objective of any closed loop controller is to take and maintained the output signal at a prescribed value. The reduction of the system error is merely one of the many important effects that feedback may have upon a system, that is the reason why this sections will deepen in several control techniques [29, Chapter 1]. This section will also delve into the state-space models concepts since it will be a recurrent representation for several systems presented in next chapters.

2.4.1 *State-Space models*

State-space models will be crucial for the overall development of the work presented on this thesis whether they will be use to describe a tokamak linear model for plasma position and shape control or use to model some other relevant variables. The first concepts to be summarized on this section are the state variable and state equation definitions ([29, Chapter 10], [30, Chapter 2]).

Let the n state equations of nth-order dynamic system be represented as:

$$\frac{dx_1(t)}{dt} = f_i[x_1(t), x_2(t), ..., x_n(t), u_1(t), u_2(t), ..., u_p(t), w_1(t)w_2(t), ..., w_v(t)] \tag{2.1}$$

where $i = 1, 2, .., n$. The ith state variable is represented by $x_i(t)$; $u_j(t)$ denotes the jth input for $j = 1, 2, .., p$; and $w_k(t)$ denotes the kth disturbance input, with $k = 1, 2, .., v$.

Let $y_1(t), y_2(t), ..., y_q(t)$ be the q system output variables. The output variables are functions of the state variables and the input variables. The output equations can be expressed as:

$$y_j(t) = g_j[x_1(t), x_2(t), ..., x_n(t), u_1(t), u_2(t), .., u_p(t), w_1(t)w_2(t), ..., w_v(t)] \tag{2.2}$$

where $j = 1, 2, .., q$.

The set of n state equations from 2.1 and the q output equations in 2.2 together they form the *dynamic equations*. In order to have an easier form of expression and manipulations of these equations is common to represent them in vectors and matrices as follows: **State vector:**

$$x(t) = \begin{bmatrix} x_1(t) \\ x_2(t) \\ \vdots \\ x_n(t) \end{bmatrix} \quad (n \times 1) \tag{2.3}$$

Input vector:

$$u(t) = \begin{bmatrix} u_1(t) \\ u_2(t) \\ \vdots \\ u_p(t) \end{bmatrix} \quad (p \times 1) \tag{2.4}$$

Output vector:

$$y(t) = \begin{bmatrix} y_1(t) \\ y_2(t) \\ \vdots \\ y_q(t) \end{bmatrix} \quad (q \times 1) \tag{2.5}$$

Disturbance vector:

$$w(t) = \begin{bmatrix} w_1(t) \\ w_2(t) \\ \vdots \\ w_v(t) \end{bmatrix} \quad (v \times 1) \tag{2.6}$$

Using these defined vectors, equation 2.1 can be write for the n states like:

$$\frac{dx(t)}{dt} = f[x(t), u(t), w(t)] \tag{2.7}$$

where f is a vector containing the functions $f_1, f_2, .., f_n$ as elements. In the same way the equations from 2.2 become:

$$y(t) = g[x(t), u(t), w(t)] \tag{2.8}$$

where g is a vector containing the functions $g_1, g_2, .., g_n$ as elements.

For a system that is time-invariant and linear like the ones that will show on next chapter, the equations can be re-write as:

$$\frac{dx(t)}{dt} = Ax(t) + Bu(t) + Ew(t) \tag{2.9}$$

$$y(t) = Cx(t) + Du(t) + Hw(t) \tag{2.10}$$

where A is the state matrix, B is the input matrix, C is the output matrix,D is the feed-forward matrix and E and H are disturbances matrices. For simplification is usual the study state-space and controllers concepts under the assumption that $w(t) = 0$ which leads to the form:

$$\frac{dx(t)}{dt} = Ax(t) + Bu(t) \tag{2.11}$$

$$y(t) = Cx(t) + Du(t) \tag{2.12}$$

When applying the Laplace transform to system from 2.12 it leads to:

$$x(s) = (sI - A)^{-1}[x(0) + Bu(s)] \tag{2.13}$$

$$y(s) = C(sI - A)^{-1}[x(0) + Bu(s)] + Du(s) \tag{2.14}$$

where $x(0)$is the initial state or initial conditions from the system [31, Chapter 4]. The representation of the system from equation 2.14 shall be use in next subsections.

State-space dynamics can describe Multiple-Input Multiple-Output (MIMO) models where a number of inputs $n_{\ inputs} > 1$ can relate through the dynamics matrices of the system to a number of outputs $n_{\ outputs} > 1$. Given the physical conditions of the systems that will be analyzed and controlled on this work MIMO models will show several times.

2.4.2 *PID control*

This subsection will shortly address the Proportional-Integral-Derivative (PID) control concepts. PID controllers are now at days the most common ones in industrial applications and they are use several times through all this work. The PID controller has three parameters; proportional gain, integral gain, and derivative gain, they have proved through the years to provide a suitable control for a variety of systems despite not being optimal always. The usefulness of PID controls lies in their general applicability to most control systems. In particular, when the mathematical model of the plant is not known and therefore analytical design methods cannot be used, PID controls prove to be most useful.

The closed-loop systems compensate the disturbances by measuring the output response, feeding that measurement back through a feedback path, and comparing that response to a reference or set point. If there is any difference between the two signals, the system drives the plant, via the actuating signal, to make a correction. If there is no difference, the system does not drive the plant, since the plant's response is already the desired set point [32, Chapter 1]. Closed-loop systems also focus on achieving the stability as a system must be stable in order to produce the proper transient and steady-state response [32, Chapter 3], thus if the closed-loop system poles are in the left half of the plane the feed-back system will be stable.

Systems that feed the error forward to the plant are called proportional control systems. Systems that feed the integral of the error to the plant are called integral control systems. Finally, systems that feed the derivative of the error to the plant are called derivative control systems [32, Chapter 9]. A PID controller consists on a feedback control loop where the current, previous and future error signal which originates from the difference between the output of the system and a given set point, is multiplied by the proportional, integral and derivative gains and then sum converting this signal into the system input, the effects on the feedback loop from each one of the gains will be described. When the model of the system plant is known is possible to apply designing techniques for the PID gains like the Ziegler-Nichols method, when is not the case analytical or even intuition arising from the physics and numerics of the problem should be applied. Figure 2.6 shows the block scheme of a PID controller with a system plant $G(s)$ on the Laplace domain.

An only proportional controller relates the output of the system to the input by a proportional constant, and even though it performs a first approach to follow the set point and stabilizes, it results in a steady-state error or offset, such error may be eliminated with integral control action, see figure 2.7.

The integral gain produces a signal that is proportional to the time integral of the error system, the offset or steady-state error can be eliminated by the sum of an integral action, the integral term also tends to produce and oscillatory response. This is an important improvement over the proportional control alone, which gives an offset. Since the PI controller is also a low-pass filter, it helps filtering out the high-frequency noise [29, Chapter 9], [33, Chapter 5]. Figure 2.8 shows the block scheme of a PI controller and its response to a unitary step.

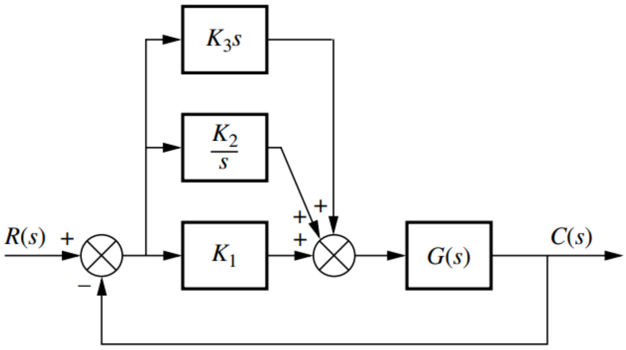

Figure 2.6.: Plant and PID controller block scheme on Laplace domain [32, Chapter 9].

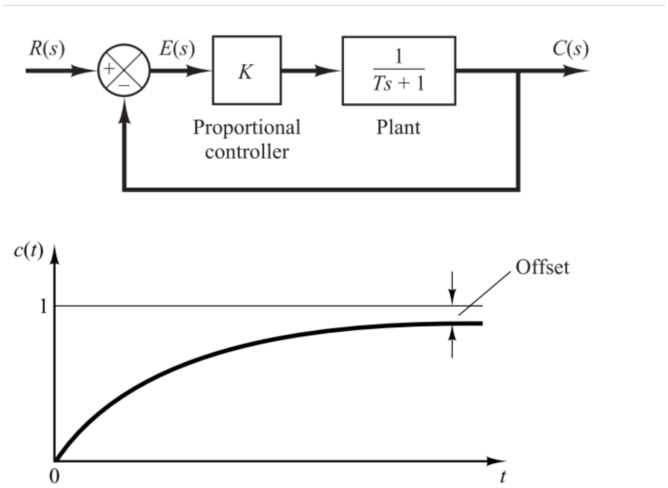

Figure 2.7.: Plant with a proportional (P) control scheme on the Laplace domain and its response to a unit-step. The offset or error between the steady-sate response is also pointed out [33, Chapter 5].

The derivative gain added to a proportional controller gives a more sensitive controller which responds to the rate of change of the error and can produce a significant correction before the magnitude of the error becomes to large. In general, derivative control anticipates the actuating error, adds damping and tends to increase the system stability, figure 2.9 depicts the scheme and system response with a PD controller. The PD control uses the error derivative $de(t)/dt$ which allows the control to anticipate the error direction, it initiates an early corrective action which means an improvement on the transient response [29, Chapter 9], [32, Chapter 9]. Normally in linear systems when the slope of $e(t)$ is large overshoots may occur, when using a PD controller it also corrects the overshoot.

A PID controller improves the steady-state error and the transient response. Figure 2.10 shows the response time traces of the same system with a PID, PD and D controllers to a unit step.

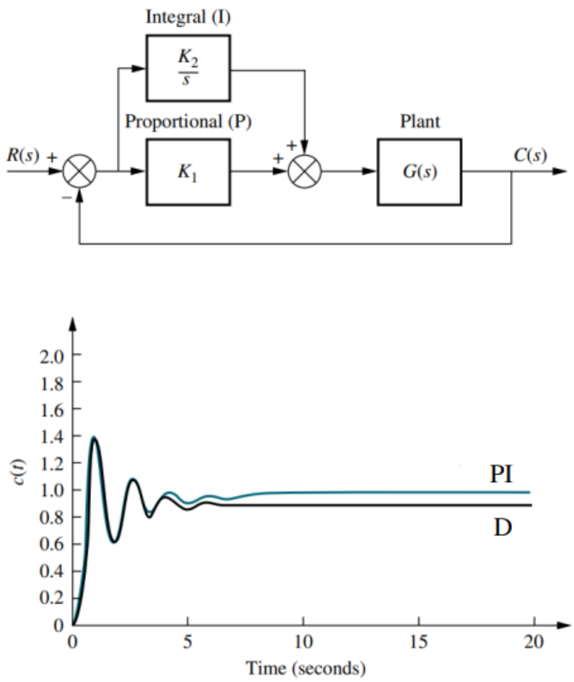

Figure 2.8.: Plant scheme of a plant with a proportional-integral (PI) control on the Laplace domain. Bottom graph corresponds to a step response to closed-loop systems with D and a PI controller [32, Chapter 9], a visible improvement on the state-state error with the PI control is observable.

2.4.3 *Multiple-Input Multiple-Output control*

This subsection will discuss the pole-place method and the linear quadratic optimal regulator (LQR) for control systems in state-space already discussed in subsection 2.4.1. State feedback controllers basically relocate the eigenvalues of the given system through a state-feedback multiplication by a constant gain matrix K so the system can follow a reference and be stabilized if necessary.

The concept of pole should be introduced as it will be related to the definitions of the MIMO control methods. The poles p_i of state-space system are the eigenvalues $\lambda_i(A)$, $i = 1, .., n$ of the system matrix A. Poles are important for establishing the stability of a system, for continuous systems a linear dynamic system $\dot{x}(t) = Ax(t) + Bu(t)$ is stable if and only if all poles are in the open left half plane (LHP), that is $\mathbb{R}e\ \lambda_i(A) < 0, \forall i$. Eigenvalues in the right half plane(RHP) with $\mathbb{R}e\ \lambda_i(A) \geq 0$ give raise to unstable modes since for this case $e^{\lambda_i(A)\ t}$ is unbounded as $t \to \infty$, eigenvalues in the open LHP give raise to stable modes where $\mathbb{R}e\ \lambda_i(A) \to 0$ as $t \to \infty$ [34, Chapter 4].

Consider the system:

$$\dot{x}(t) = Ax(t) + Bu(t) \tag{2.15}$$

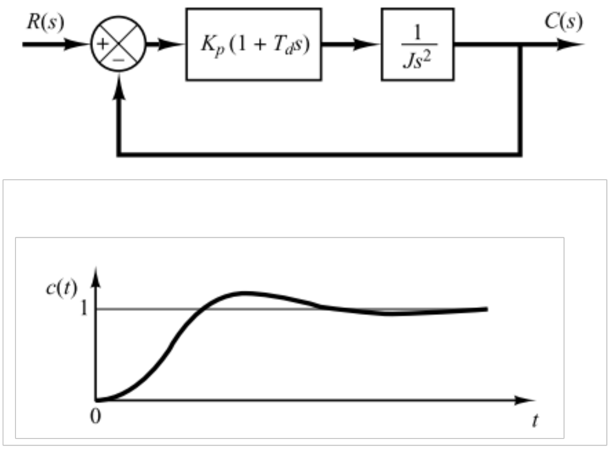

Figure 2.9.: The top scheme shows a PD controller for a plant that is only modeled as an inertial load, on the graph below is shown the system response where it is possible to observe an offset reduction and a controlled transient as compared with the P controller [33, Chapter 5].

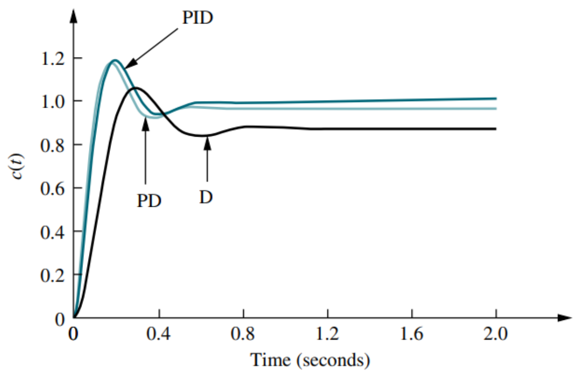

Figure 2.10.: Step response to closed-loop systems with D,PD and PID controllers [32, Chapter 9].

$$y(t) = Cx(t)$$

where it is assumed that $D = 0$. In state feedback, the input $u(t)$ is given by:

$$u(t) = r(t) - Kx(t) = r(t) - [k_1 \; k_2 \; \cdots \; k_n]x(t) = r - \sum_{i=1}^{n} k_i x_i \tag{2.16}$$

as shown in figure 2.11. Each feedback gain k_i is a real constant.This is called the constant gain negative state feedback or in a simpler form *state feedback* [31]. Substituting equation 2.15 into 2.16 its obtained:

$$\begin{aligned} \dot{x}(t) &= (A - B\,K)x(t) + Br(t) \\ y(t) &= Cx(t) \end{aligned} \tag{2.17}$$

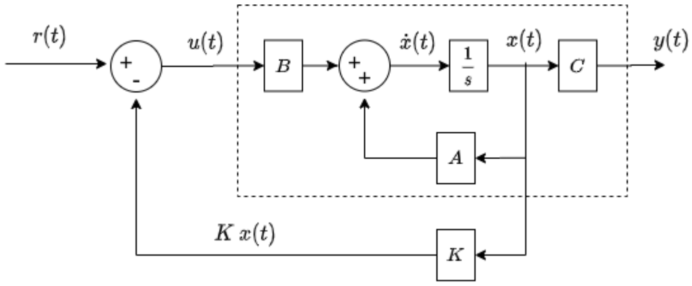

Figure 2.11.: State-space model with a K gain matrix feedback scheme.

The first control MIMO algorithm to be addressed is the pole-placement method which consists in placing the closed-loop system poles in certain location by means of state feedback through an appropriate state feedback gain matrix K, the design objective of the pole-placement design is to find K such that the eigenvalues or poles of $(A - BK)$, or the closed-loop system, are of certain prescribed values. For this method the eigenvalues of the closed-loop system can assigned arbitrarily as long as they are stable [29, Chapter 10]. The determination of the desired closed-loop poles is based on the transient-response and/or frequency-response requirements, such as speed, damping ratio, or bandwidth, as well as steady-state requirements [33, Chapter 10].

Let's consider the system given in equation 2.17 and the feedback control input from 2.16, by substituting one on the other the closed-loop system is represented by the equation:

$$\dot{x}(t) = (A - BK)x(t) + Br(t) \quad , \tag{2.18}$$

K is the $1 \times n$ feedback matrix that can give an arbitrary set of eigenvalues or poles of $(A - BK)$, which are the n roots of the Laplace equation [29, Chapter 10]:

$$|sI - A + BK| = 0 \quad . \tag{2.19}$$

From the canonical representation of equation 2.15 its obtained ([29, Chapter 10] , [31, Chapter 4]) :

$$A = \begin{bmatrix} 0 & 1 & 0 & \cdots & 0 \\ 0 & 0 & 1 & \cdots & 0 \\ \vdots & \vdots & \vdots & \ddots & \vdots \\ 0 & 0 & 0 & \cdots & 1 \\ -a_0 & -a_1 & -a_2 & \cdots & -a_{n-1} \end{bmatrix} \quad B = \begin{bmatrix} 0 \\ 0 \\ \vdots \\ 0 \\ 1 \end{bmatrix} \quad . \tag{2.20}$$

Then the gain feedback matrix K is expressed as:

$$K = [k_1 \; k_2 \; \cdots \; k_n] \tag{2.21}$$

where $k_1, k_2, \cdots, k_n$ are real constants, this leads to the expression:

$$A - BK = \begin{bmatrix} 0 & 1 & 0 & \cdots & 0 \\ 0 & 0 & 1 & \cdots & 0 \\ \vdots & \vdots & \vdots & \ddots & \vdots \\ 0 & 0 & 0 & \cdots & 1 \\ -a_0 - k_1 & -a_1 - k_2 & -a_2 - k_3 & \cdots & -a_{n-1} - k_n \end{bmatrix} \tag{2.22}$$

The eigenvalues or poles of $A - BK$ can be found from the characteristic equation:

$$|sI - A + BK| = s^n + (a_{n-1} + k_n)s^{n-1} + (a_{n-2} + k_{n-1})s^{n-2} + \cdots + (a_0 + k_1) = 0 \tag{2.23}$$

since the elements $k_1, k_2, \cdots, k_n$ are isolated in each coefficient of the characteristic equation the eigenvalues can be arbitrarily assigned to any set of stable poles [29, Chapter 10], [33, Chapter 10].

Another control technique for state-space feedback is the optimal control refereed as Linear Quadratic Gaussian (LQG) or Linear Quadratic Regulator (LQR). It is assumed that the plant dynamics are linear and there are noise measurements and disturbance signals stochastic with known statistical properties [34, Chapter 9].

Consider the system:

$$\dot{x}(t) = Ax(t) + Bu(t) \tag{2.24}$$

that has an initial condition $x(t_0) = x_0 \neq 0$. Therefore $x(t) \neq 0$, $t \geq t_0$ and the regulator problem is to apply an input signal $u(t)$ that takes the system back to the zero state in an optimal manner. The manner the LQR regulator achieves this is by minimizing the deterministic cost [34, Chapter 9], [29, Chapter 3]:

$$J_r = \int_0^\infty (x(t)^T \, Q \, x(t) \; + \; u(t)^T \, R \, u(t) dt \tag{2.25}$$

where Q is a positive-definite Hermitian or real symmetric matrix and R is a positive-definite Hermitian or real symmetric matrix. The optimal solution is for any initial state $u(t) = -K_r x(t)$ where:

$$K_r = R^{-1} \, B^T \, X \tag{2.26}$$

and $X = X^T \geq 0$ is the unique positive-semidefinite solutions of the algebraic Ricatti equation

$$A^T X \; + \; XA \; - \; XBR^{-1}B^T X \; + Q = 0 \quad . \tag{2.27}$$

In order to design the optimal K_r feedback gain the Ricatti equation 2.27 has to be solved for the matrix X and then substitute into equation 2.26.

2.4.4 *Observers and Kalman filters*

In practical real systems that have been modeled as state-space it may occur that the states vector, which is vital for performing the feedback control of the methods just presented, is not fully measurable, when this occurs is necessary to retrieve the states-vector $x(t)$ from the system outputs $y(t)$ and is obtained through an state estimator also called observer to estimate not measurable state variables [31, Chapter 8]. A state observer estimates the state vector based on the measurements of the output and inputs system signals. The inputs of the observer are the output $y(t)$ and the control input $u(t)$. Similarly with the construction of a state-space controller, the observer uses an observer gain matrix K_{obs} which is a weighting matrix to the correction term involving the difference between the measured output $y(t)$ and the estimated output $C\ x_{est}(t)$, where $x_{est}(t)$ are the estimated states [33, Chapter 10].

Through the observer gain matrix K_{obs} is possible to retrieve an estimated state-space model which will have as output the reconstructed states $x_{est}(t)$ and the reconstructed outputs $y_{est}(t)$, the estimation error or observation error is the difference between $y(t))$ and $y_{est}(t)$. Figure 2.12 shows a scheme of state-space plant model and a observer block to reconstruct the states.

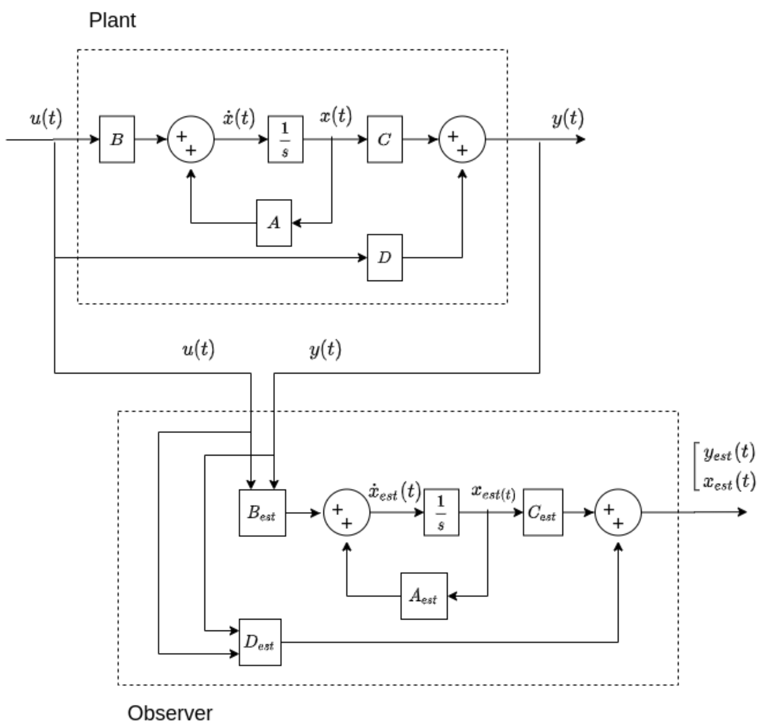

Figure 2.12.: Scheme of a state-space model plant and its observer or state estimator.

Kalman filters have the structure of an ordinary state estimator but they take into account the process and measurement noise(ω_d , ω_n) from the inputs signals. In Kalman filters the optimal choice of K_{obs}, which minimizes the covariance $E[x - x_{est}]^T\ [x - x_{est}]$, is given by [34, Chapter 9]:

$$K_{obs} = Y\, C^T\, V^{-1} \tag{2.28}$$

where $Y = YT\ \geq 0$ is the unique positive-semidefinite solution of the algebraic Ricatti equation:

$$YA^T\ +\ AY\ -\ YC^TV^{-1}CY\ + W = 0 \tag{2.29}$$

where W is a positive-definite Hermitian or real symmetric matrix and V is a positive-definite Hermitian or real symmetric matrix, solving equation 2.29 for Y and substituting on 2.28, gives the optimal K_{obs} for reconstructing the states of the original system . The combination of an optimal state estimator or Kalman filter and an optimal state feedback or LQR controller is commonly called LQG, this type of compensator-estimator configuration will be used ahead for implementation of plasma position controllers.

3

JT60-SA CONTROL DESIGN

3.1 MACHINE DESCRIPTION

JT60-SA is a superconductive tokamak located at one of the facilities from the National Institutes for Quantum and Radiological Science and Technology (QST) at Naka, Japan whose principal purpose is the contribution to early realization of fusion energy by supporting the exploitation and resolving key physics for the ITER reactor. JT60-SA construction has been successfully completed by the end of March 2020 and its first plasma is expected for late 2020. Figure 3.1 shows the overall general configuration and the most remarkable elements of the machine. The JT-60SA vacuum chamber will have a major radius of 2.96 m and a Minor radius of 1.18 m with an overall plasma volume of 132 m^3 [35] . Jt60-SA will become the largest tokamak ever built so far.

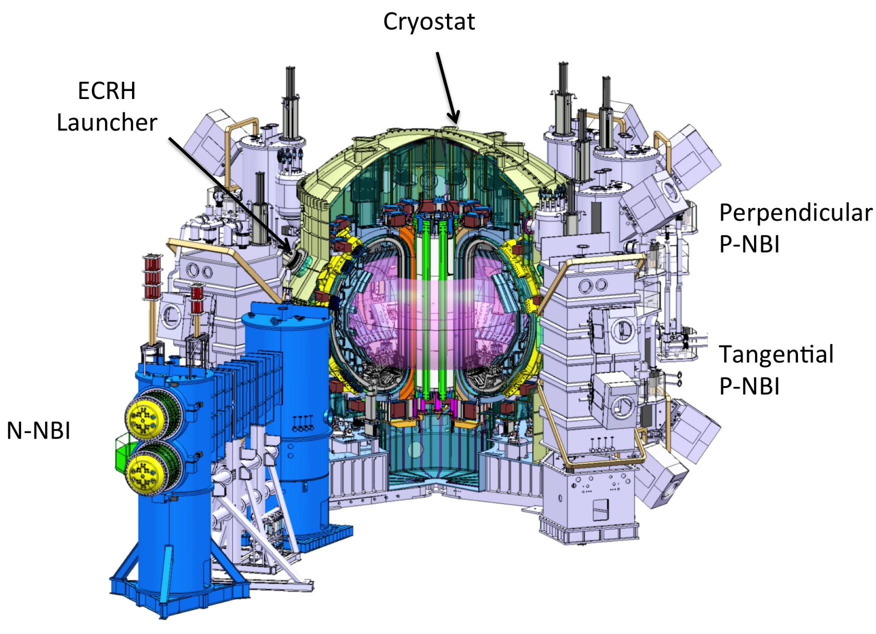

Figure 3.1.: JT60-SA tokamak configuration and its main elements [36].

The Poloidal Field (PF) coils shown in JT60-SA cross-section from figure 3.2 consist of two sets of superconductive coils: the Equilibrium Field Coils (EF1–6) and the Central Solenoid (consisting of

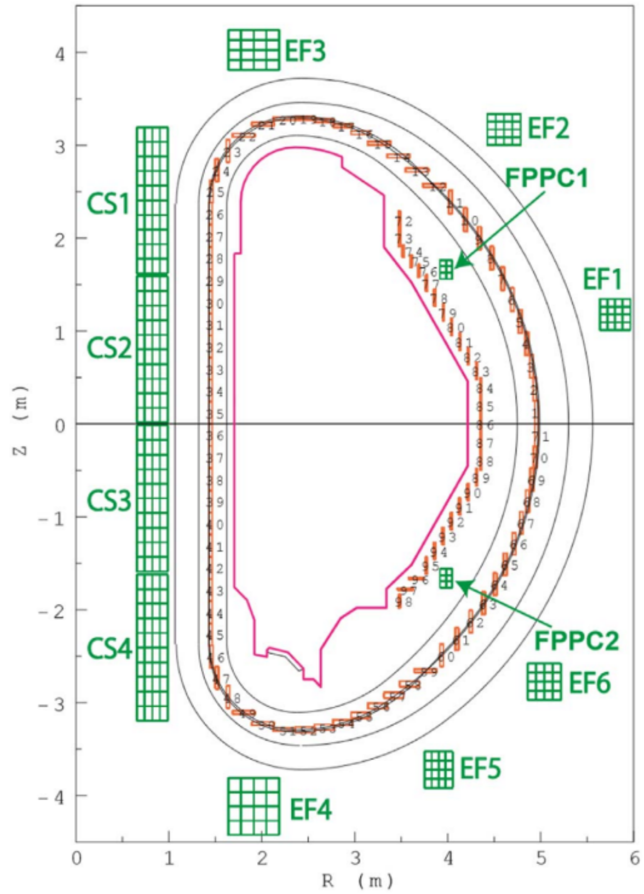

Figure 3.2.: JT-60SA poloidal cross-section and layout of the Poloidal Field coils system [37].

four independent coils, named CS1–4). Furthermore, two in-vessel Fast Plasma Position Copper Coils (FPPC1–2) will also be installed [37].The total of 12 PF coils have independent power sources for the control of the plasma current, position and shape.

JT-60SA shall be capable of investigating different design scenarios. As refereed in [38] it exists a set of 6 reference scenarios, additional ones, including some with a shorter repetition rate will be defined in future. For the control study in this section all simulations will be built based on the Scenario 2 characteristics. In particular, Scenario 2 refers to a 5.5 MA inductive lower single null discharge. The Scenario 2 its divided in 5 time snapshots with different equilibrium each one starting at t=-40 s until t= 177.96 s. The different Last Closed Flux Surfaces (LCFS) for each time window are shown in figure 3.3, the time sequence starts at the X-point formation (XPF) followed by the Start of Heating(SOH), the Start of Flattop (SOF), End of Flattop (EOF), End Of Cooling(EOC) and finishing with the End of Currents in the PF coils (EOC). In this section, reconstruction methods and control algorithms will be based on the *Start of Flattop* (SOF) equilibrium shown in figure 3.4. The nominal values for the plasma current, the poloidal beta and the internal inductance for Scenario 2 at SOF are $I_{p_{eq}} = 5.5$ MA, $\beta_{p_{eq}} = 0.53$, and $l_{i_{eq}} = 0.85$.

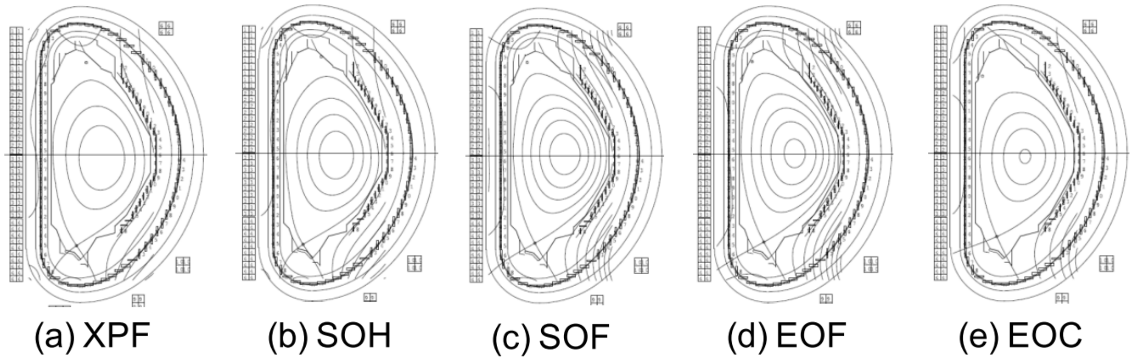

Figure 3.3.: LCFS Equilibria corresponding to the different Scenario 2 snapshots: X-point formation (XPF), Start of Heating(SOH), the Start of Flattop (SOF), End of Flattop (EOF), End Of Cooling(EOC) and End of Currents in the PF coils (EOC) [38].

This chapter will address two different approaches for the LCFS reconstruction along with different plasma current, shape and position controllers for JT60-SA in order to achieve and maintain the desired operational scenario given the plasma equilibrium in the SOF while the performance of the controllers is compared .

3.2 CREATE MAGNETIC RECONSTRUCTION TOOLS

CREATE-NL is a finite elements method (FEM[1]) solver implemented on MATLAB. It deals with the free boundary dynamic plasma equilibrium problem i.e. the MHD (Magneto-Hydro-Dynamics) time evolution of 2D axisymmetric plasmas in tokamaks, including eddy currents in the passive structures, and feedback control laws for current, position and shape control [39].

Using the CREATE codes [27,39] it is possible to retrieve a linearized state-space model for a reference configuration that describes the plasma magnetic behavior around that equilibrium[2]. It should be noted that CREATE-NL equilibrium solver has been validated on several tokamaks such as JET and EAST. A JT60-SA CREATE-NL electromagnetic linear model around the equilibrium from the Scenario 2- SOF for the plasma-circuit response has been used for designing the controller presented in next section.

3.3 CONTROLLER DESIGN

The JET (Joint European Torus) tokamak was the first machine where around 2005 a new model based plasma current and shape controller was set up and tested with the existing active circuits and

1 It is well known that many physical and engineering systems are expressed in terms of partial differential equations which cannot be solved via analytical methods. One of the most recurrent techniques is numerical discretization to approximate the solution of the partial differential equations, the FEM is commonly used to solve these approximations in two or three space variables, in this particular case for a numerical solution of the well-known Grad-Shafranov equation.

2 Reference [37, Sec. 3] can be consulted for more details about the use of the CREATE equilibrium codes to retrieve plasma linearized models.

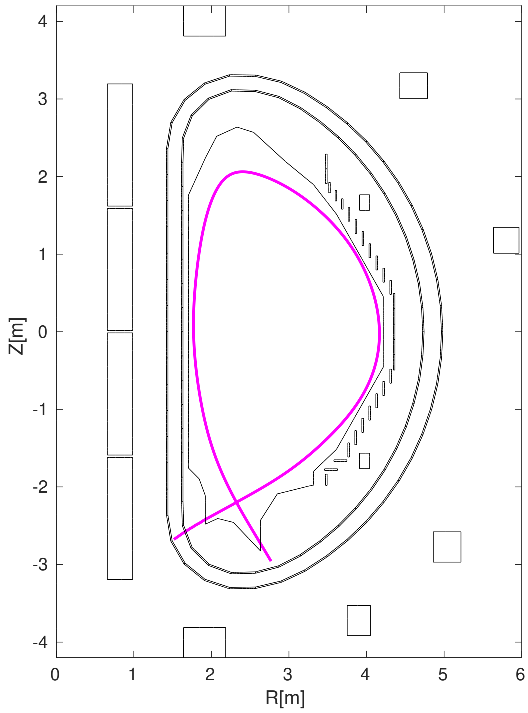

Figure 3.4.: Poloidal cross-section of the JT-60SA plasma at the Start of the Flat Top (SOF) for reference Scenario 2. At SOF, the nominal plasma current is 5.5 MA, while the nominal values for poloidal beta β_p and internal inductance l_i are 0.53 and 0.85, respectively.

control hardware. The novelty controller was the eXtreme Shape Controller (XSC) and its aim was to improve the performance of the, back then, present controller to allow the control of extremely shaped plasmas with higher values of elongation and triangularity [40]. More recently this control approach was utilized at TCV [41]. At JET, the XSC recently enabled the control of high triangularity shapes with both strike points in the divertor corner, which has a large impact in the H-mode confinement in the case of the ITER-like wall at JET [42].

Usually the controlled shape geometrical descriptors are the distances between the plasma boundary and the vessel at some specific points. These plasma-wall distances are called gaps [43]. The gaps are segments that can be used to describe the shape of the plasma boundary. Being g_i the abscissa along the i-th control segment, we assume that $g_i = 0$ at the first wall. *Gap-based* plasma shape control is achieved by controlling to zero the difference $g_{i_{ref}} - g_i$ on a sufficiently large number of gaps, being g_{i_ref} the value of the abscissa on the i-th control segment for the reference shape. Figure 3.5 shows a poloidal cross-section of JT-60SA together with a set of 85 gaps used for the assessment of the plasma shape control.

The XSC algorithm can be used either to implement a gap-based control strategy, or an isoflux one, as it has been proposed in [37]. The isoflux strategy consists in controlling the X-point position along with a set of flux differences between the flux at some selected control points along the desired plasma

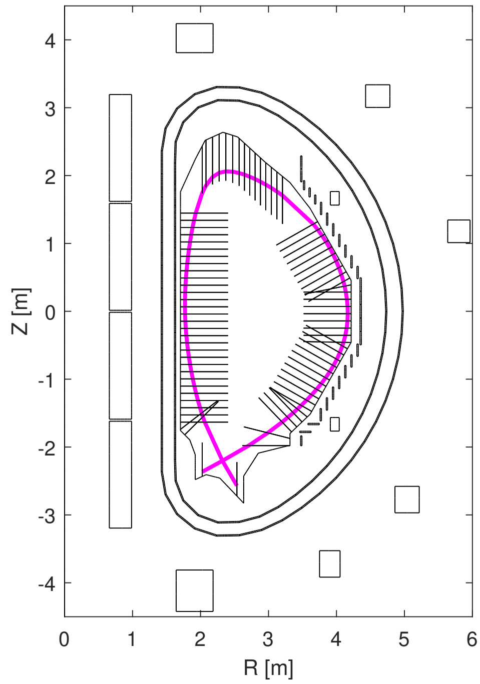

Figure 3.5.: Poloidal cross-section of the JT-60SA plasma at the Start of the Flat Top (SOF) for reference Scenario 2. At SOF, the nominal plasma current is 5.5 MA, while the nominal values for poloidal beta β_p and internal inductance l_i are 0.53 and 0.85, respectively. In this figure the 85 gaps used to assess the plasma shape controller performance are shown.

boundary and the X-point flux. Thus the XSC block inputs are the error between the X-point flux and the fluxes in the control points, and the X-point position error.

The peculiarity of the XSC approach is that it permits to control a number of plasma shape descriptors that is greater than the number of available actuators, i.e. of PF Circuits, this is basically tackled by using a singular value decomposition (SVD) to identify the principal directions of the algebraic mapping between coil currents and geometrical descriptors [40]. The XSC control relies on the PFC decoupling controller (more details can be found in [37, Section 4.4]), since it is assumed that each PF coil can be treated as an independent single-input-single-output (SISO) channel whose dynamic response is modeled in the Laplace domain by

$$I_{PF_i}(s) = \frac{I_{PF_{ref,i}}(s)}{1 + s\tau_{PF}},$$

where I_{PF_i} and $I_{PF_{ref_i}}$ are the Laplace transform of the measured and reference current in the i-th PFC, respectively, and where it is assumed that all the PFC exhibit the same bandwidth (i.e., they have the same time constant τ_{PF}).

Denoting by $\delta Y(s)$ the Laplace transform of the variations of the n_G shape descriptors to be controlled, it is possible to exploit the CREATE electromagnetic linear model [37] that links the variation of the PFC reference currents $\delta I_{PF_{ref}}$ to $\delta Y(s)$, i.e.

$$\delta Y(s) = C\frac{\delta I_{PF_{ref}}(s)}{1+s\tau_{PF}},$$

which, at steady-state, implies $\delta Y(s) = C\delta I_{PF_{ref}}(s)$.

If the number of controlled plasma shape descriptors n_G is such that $n_G > n_{PF}$, the XSC computes the additional current references as

$$\delta I_{PF_{ref}} = C^{\dagger}\delta Y\,. \tag{3.1}$$

where the matrix $C^{\dagger}$ denotes the pseudo-inverse of C[3] that can be computed via the singular value decomposition (SVD). As a result, the XSC algorithm minimizes the following steady-state performance index

$$J_{XSC} = \lim_{t\to+\infty}(\delta Y_{ref} - \delta Y(t))^T(\delta Y_{ref} - \delta Y(t))\,, \tag{3.2}$$

where δY_{ref} are constant references for the geometrical descriptors. When the SVD of the C matrix is used to minimize (3.2), it may happen that some singular values (depending on the plasma configuration) are one order of magnitude smaller than the others. This fact implies that minimizing the performance index (3.2) retaining all the singular values results in a large control effort at the steady-state, that is a large request on some PFC currents which have only a minor effect on the plasma shape. In order to minimize also the control effort, the additional references (3.1) are generated by using only the $\bar{n} < n_{PF}$ linear combinations of PF currents which are related to the largest singular values of the C matrix. This is achieved by using only the $\bar{n}$ singular values when computing the pseudo-inverse $C^{\dagger}$.

Moreover, the PFC current variations given by (3.1) are summed to the scenario currents and sent to the PFC decoupling controller as references to be tracked. It is worth to remark here that the dynamnic behavior of the XSC is improved by adding a set of proportional-integral-derivative (PID) controllers on each PF coil channel (see [44] for a complete description of the XSC control scheme).

For the development of this work both approaches of the XSC strategy were studied and simulated for a different number of control points: isoflux and gap-based controllers. In addition, a second controller developed by the QST team was implemented in the simulations, the features of this controller will be detailed in the next section.

3.4 QST RECONSTRUCTION AND CONTROL IMPLEMENTATION

Along with the CREATE tools presented on last section for the reconstruction of the LCFS and the XSC for plasma shape control, a reconstruction code and controller provided by the QST team

3 C is the output matrix from the state-space linearized CREATE model for JT60-SA.

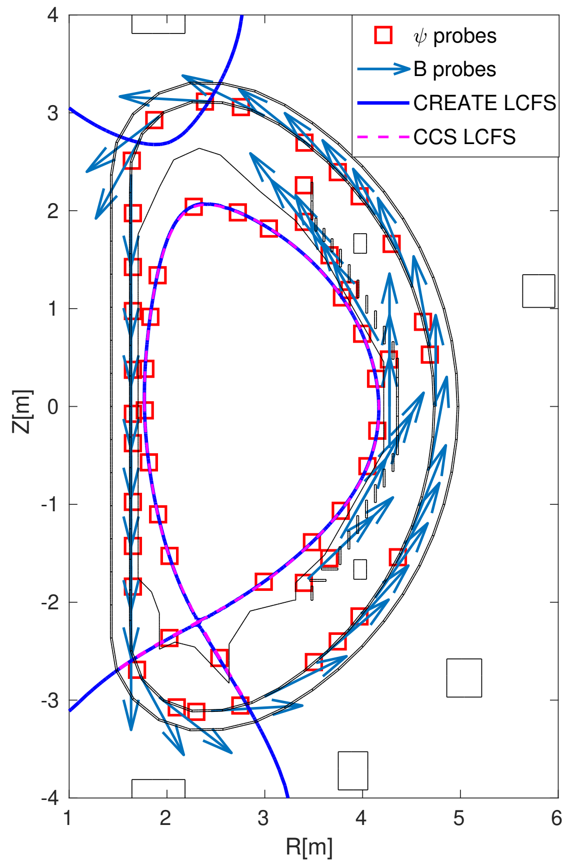

Figure 3.6.: SOF equilibrium reconstructed from CREATE-NL and the CCS code along with the magnetic field and flux sensors locations.

were implemented, tested and compared. This section will briefly describe these two methods and its limitations.

3.4.1 *Cauchy Condition Surface (CCS) reconstruction method*

The QST Cauchy Condition Surface (CCS) method for the reconstruction of the magnetic last closed flux surface (LCFS) calculates controlled variables for plasma position and shape control such as the poloidal magnetic flux at control points on an isoflux scheme [45] . The CCS method allows a selection up to 19 geometrical points for dexcribing the LCFS and its input parameters are the current in the PF coils, the measurements in the magnetic field and flux sensors and the plasma current. The output signals from the CCS reconstruction method are the magnetic fluxes at the X-point and at the selected geometrical points.

3.4.2 *QST magnetic controller*

The QST magnetic controller uses the PF coils signals to control the plasma current I_p, position and shape, and the FPPC coils signals for plasma position control. The PF coil currents I_{PF-ref} are calculated using an isoflux control approach using proportional-integral(PI) feedback controllers [46]. The controller calculates I_{PF-ref} reducing $\delta\Psi_s$ and $\delta\Psi_x$ according to:

$$I_{PF\_ref}(t+\Delta t) = I_{PF}(t_0) + M^{\dagger}_{PF}\left[G_{SP}\delta\Psi_s(t) + G_{SI}\int_{t_0}^{t}\delta\Psi_s(t)dt + G_{XP}\delta\Psi_X(t) + G_{XI}\int_{t0}^{t}\delta\Psi_x(t)dt\right] , \tag{3.3}$$

where $\delta\Psi_s$ is the residual between the LCFS flux and the control point fluxes, $\delta\Psi_x$ is the difference between the I_p value and its reference, t_0 is the initial time , Δt is the coil control cycle, $M^{\dagger}_{PF}$ is the (m $\times$ (n + 1)) control matrix which is the pseudo-inverse of the Green function M calculated using the SVD method; where m is the number of PF coils , n is the number of control points including the evaluated X-point. G_{SP} and G_{SI} are the respective control gains for the PI plasma position and shape feedback controllers, G_{XP} and G_{XI} are the PI control gains for the I_p feedback control. G_{SP} and G_{XP} are dimensionless and, G_{SI} and G_{XI} are in s^{-1}.

The coils voltage command values ($V_{coil-com}$) are calculated considering the mutual interactions between the PF coils an the plasma,the actual values of the PF coil currents, I_p and the mutual inductances. On a real plasma experiment, the mutual inductances between the plasma and the PF coils are unknown due to the difficulty of measuring them directly. Therefore, they are provided by the CCS method. The controller calculates command values of PF coils voltages according to the following equation:

$$V_{com} = G_{vt}\left[M_{coil}\frac{(I_{coil\_ref} - I_{coil\_meas})}{dt} + \frac{M_{plasma\_now}\cdot I_{p\_now} - M_{plasma\_bfr}\cdot I_{p\_bfr}}{dt}\right] , \tag{3.4}$$

where M_{coil} represents the mutual inductances between the coils, I_{coil_meas} are the measured coil currents, M_{plasma_now} and M_{plasma_bfr} are the mutual inductances between the plasma and the coils at the current and previous time step,I_{p_now} and I_{p_bfr} are the measured plasma current at the current and previous time step and G_{vt} is the voltage transformer gain.

On the other hand,the in-vessel FPPC coils currents (I_{FPPC_ref}) are calculated with an isoflux control approach which uses proportional-differential (PD) feedback control. In order to reduce the residual between the LCFS flux and two specified control points (Ψ_{SF}) the controller calculates (I_{FPPC_ref}) using:

$$I_{FPPC\_ref}(t+\Delta t) = I_{FPPC}(t_0) + M^{\dagger}_{FPPC}\left[G_{FP}\delta\Psi_{SF}(t) + G_{FD}\frac{d}{dt}\delta\Psi_{SF}(t)\right] , \tag{3.5}$$

where $M^{\dagger}_{FPPC}$ is the 2×2 control matrix which is the pseudo-inverse of the Green function M_{FPPC}, G_{FP} and G_{FD} are the respective PD feedback gains for the plasma position control. G_{FP} is dimensionless and G_{FD} is in s.

3.5 SIMULATION RESULTS

The simulations for the JT60-SA CREATE-NL model ,the XSC, the CCS reconstruction method and the QST controller were programmed on top of MATLAB and SIMULINK blocks. This section will address in detail the outcome of the control simulations using a linearized equilibrium given by CREATE-NL for JT60-SA, Scenario 2 at the SOF time frame. The first results to be presented correspond to a gap-based controller using the XSC with different tests cases.

The second part of the results corresponds to isoflux controllers using the XSC with a LCFS reconstruction given by CREATE and also given by the CCS method, as well as the QST controller with the LCFS reconstructed by the CCS method and by CREATE. The figures 3.7 and 3.8 show an overall control block scheme for the simulations. Figure 3.7 corresponds to a configuration using the XSC where the LCFS can be obtained through the CCS method or from the CREATE model. It is worth to point out the existence of the block localized on the bottom part of the scheme called "Vertical Stability Control" along with the XSC. The task of this block is to vertically stabilize the plasma by exploiting the in-vessel coils, which are able to guarantee a faster response due to the fact that the magnetic field generated does not have to penetrate the vessel structures [37]. This controller calculates the voltages at the FPPC coils with the equation:

$$V_{FPPC}(t) = k_1 I_{FPPC}(t) + k_2 \dot{z}_p(t) \tag{3.6}$$

By tuning the gains k_1 and k_2 from equation 3.6 is possible to obtain zero velocity in the vertical plasma direction while maintaining low imbalance currentI_{FPPC} in the in-vessel coils [37, Sec. 4.1]. In addition should also be notice the block "Ip Control" which is a Plasma current Controller, which tracks the desired value of the plasma current [47].

Figure 3.8 depicts a configuration using the QST controller reciving as inputs the magnetic fluxes measured at the control points reconstructed either by the CCS method or by the CREATE linearized model.

3.5.1 *Disturbances*

As far as plasma magnetic control is concerned, the JT60-SA linearized model disturbances have been modeled as variations of β_p and l_i. This disturbances should be in principle rejected by the control systems and maintain in the most accurate possible way the plasma equilibrium. The following set of disturbances have been considered:

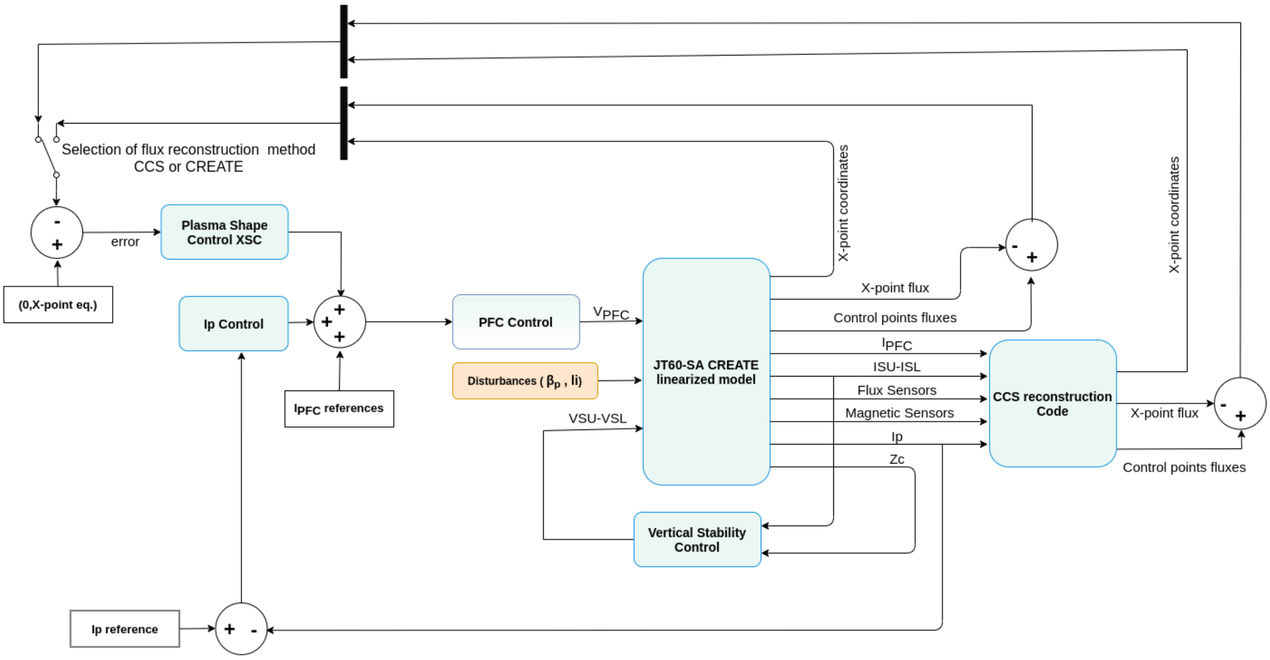

Figure 3.7.: JT-60SA overall control scheme with the CREATE linearized model and the CCS LCFS reconstruction method using the XSC for an isoflux control approach.

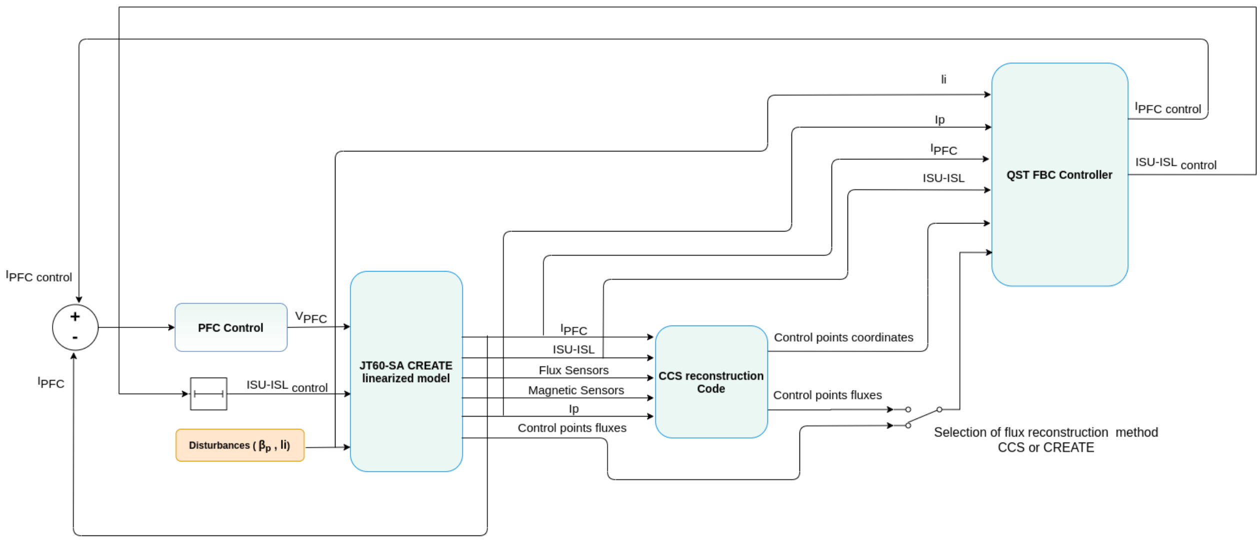

Figure 3.8.: Isoflux control JT-60SA overall scheme with a block for the CREATE JT60-SA linearized model, a block for reconstructing the magnetic fluxes with the CCS method and the QST controller.

- **Disturbance #1** refers to the behavior of β_p and l_i soon after the current flattop is reached, as it was modeled in [48] (in this paper we assume that the flattop is reached at $t \sim 20$ s). As an example, the correspondent time traces are shown in figure 3.9[4].

- **Disturbance #2** refers to the behaviour of β_p and l_i when a compound ELM[5] appears during the flattop. As described in [38, p. 34], an instantaneous drop in β_p of 0.05 $\beta_{p_{eq}}$ is followed by and exponential recovery with a time constant of 0.05 s with a frequency 10 Hz, l_i is described by an instantaneous drop of 0.06 $(l_{i_{eq}} - 0.5)$ followed by and exponential recovery with a time constant of 0.05 s with a frequency 10 Hz. The time traces for β_p and l_i are described in figure 3.10.

- **Disturbance #3** describes an instantaneous drop in l_i of 0.2 $(l_{i_{eq}} - 0.5)$ without recovery, simultaneous with a drop on β_p of 0.2 $\beta_{p_{eq}}$ followed by a recovery exponential time of 1 s [38, p. 34], which are typical of a so called *Minor disruption*. The correspondent time traces for both β_p and l_i are reported in figure 3.11.

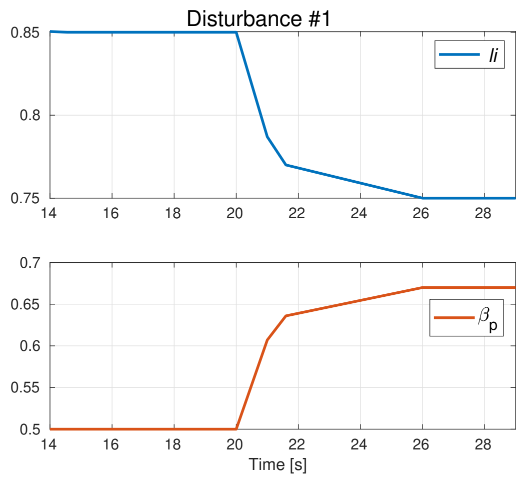

Figure 3.9.: Poloidal beta and internal inductance time traces for Disturbance #1 that models the expected disturbance soon after the plasma current flattop is reached (at $t \sim 20$ s), according to what has been considered in [48].

3.5.2 *Gap-based XSC*

JT-60SA represents a relevant benchmark to further validate the gap-based control approach, given the high beta regimes that are envisaged during its operation, which represent a challenge from the plasma magnetic control perspective. Different test cases are considered to assess the performance of the proposed shape controller, with the aim of defining an optimal set of gaps to be controlled. This

4 The time behavior of both β_p and l_i have been estimated starting from the spatial profiles for both plasma density and temperature envisaged for Scenario 2.
5 A compound ELM is commonly referred as multiple clearly distinguishable crash events causing large energy losses [49].

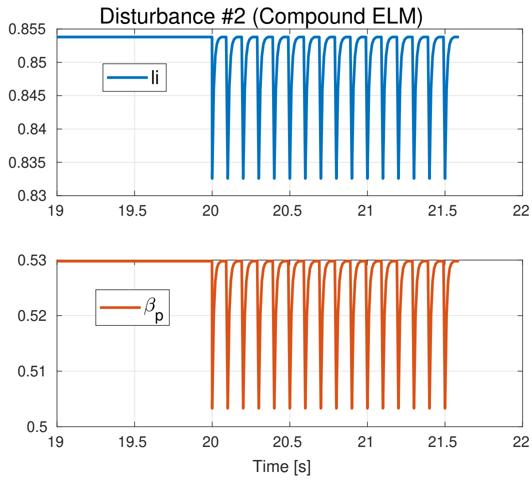

Figure 3.10.: Poloidal beta and internal inductance time traces for Disturbance #2 that models the behavior of these variables due to the presence of a compound ELM as defined in [38].

sections evaluates the steady-state performance of the plasma shape controller under different choices for *gaps* to be controlled.

All around the first wall an equally spaced distribution of 85 gaps was considered as shown in figure 3.5. It should be noticed that all different selections of controlled gaps considered in this paper include the two vertical gaps in the divertor zone, which allows to control the strike-points, and hence the position of the X-point. Other than the whole set of 85 gaps, three additional choices are considered. The first one is reported in figure 3.12a, which consists of 20 gaps equally spaced along the first wall. Moreover, the selection of 8 and 6 gaps that correspond with the control segments considered by the isoflux controllers presented in [50] and [51], respectively, have been also considered (see figures 3.12b and 3.12c). These two latter options are the outcome of preliminary studies aimed at controlling the plasma shape with a set of almost decoupled loops, i.e. SISO, while the XSC approach proposed in this section is intrinsically MIMO. Moreover, it is worth to remark that, although in [50] and [51] the 8 and 6 gap options have been used with an isoflux control approach, here the same control segments have been used to design the XSC adopting a gap-based approach.

The comparison between the various considered gap sets for the different disturbances test cases is summarized in Table 3.1. This table shows the *root-mean-square error* (RMSE) between the reference shape and the shape obtained at steady-state after the occurrence of the disturbances. For all the cases reported in Table 3.1, the RMSE has been computed on the set of 85 gaps shown in figure 3.5, even when not all of them are controlled.

It turns out that, according to this preliminary analysis, the rejection of the disturbances induced by the compound ELMs at steady-state is not an issue at JT-60SA, whatever is the set of gaps that is controlled. Indeed, figure 3.13 shows the RMSE time traces for Disturbance #2 (compound ELMs), being the RMSE computed on the set of 85 gaps shown in figure 3.5 for all the considered options. It turns

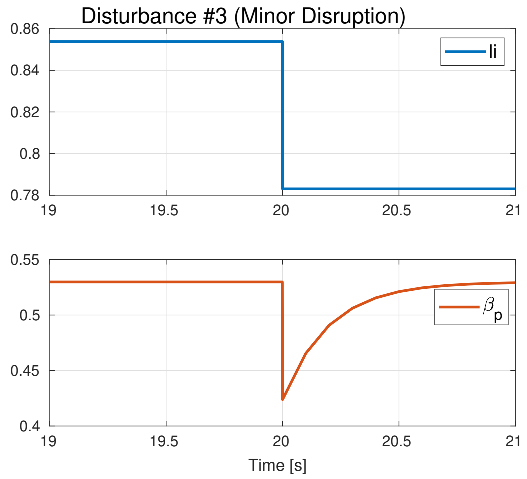

Figure 3.11.: Poloidal beta and internal inductance time traces for Disturbance #3 that models the behavior of these variables due to the presence of a Minor disruption as defined in [38].

Steady-state RMSE mm				
	85 gaps	20 gaps	8 gaps	6 gaps
Disturbance #1	7.7	8.7	31.2	19.8
Disturbance # 2 (compound ELM)	~ 0	~ 0	~ 0	~ 0
Disturbance # 3 (Minor disruption)	6.1	7.8	26.9	16.3

Table 3.1.: Steady-state RMSE values for the different choices of number of controlled gaps and for the different disturbances test cases.

out that, whatever gap set is used, the controller has almost the same behavior, with a slightly worse performance of the 6 and 8 gap options. Being a periodic disturbance, the compound ELMs have been applied only during the first part of the simulation, in order to evaluate the steady-state performance of the controller. However, from figure 3.13 it can be noticed that the rejection of the compound ELMs is not a concern even during the transients, being the maximum RMSE ~ 2 mm.

For the other two considered cases, at steady-state, the selection of 85 and 20 gaps have a considerable better RMSE in comparison with the selection of 8 and 6 gaps. As outlined in Table 3.1, the worst case corresponds to the selection of 8 gaps with the presence of Disturbance #3 (Minor disruption) during the flattop. As an example, figure 3.15 shows a comparison of the steady-state shape obtained for the 8 and 20 gaps options when the Minor disruption in considered. Figure 3.14 shows the RMSE time traces for this disturbance and it can be noticed that the 20 gaps option gives better results with respect to the 8 and 6 gaps cases also during the transient, and not just in steady-state. In particular, in the 6 and 8 gaps cases, being the number of controlled gaps less than the number of the actuators available for plasma shape control, the steady-state error on the controlled gaps is practically zero. However, not being these two sets of gaps *well representative* of the whole plasma boundary, minimizing the error on such sets does not minimize the error on the whole boundary, as shown in figure 3.14.

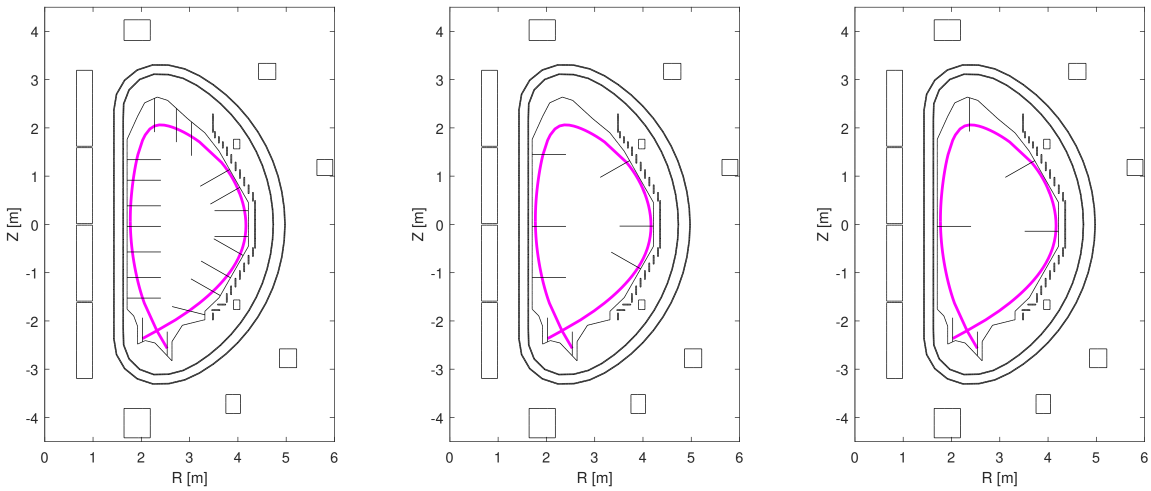

(a) The 20 gaps used to assess the performance of plasma shape controller.

(b) The 8 control segments by the isoflux controller proposed in [50].

(c) The 6 control segments used by the isoflux controller proposed in [51].

Figure 3.12.: Different choices for the set of controlled gaps used for gap controller.

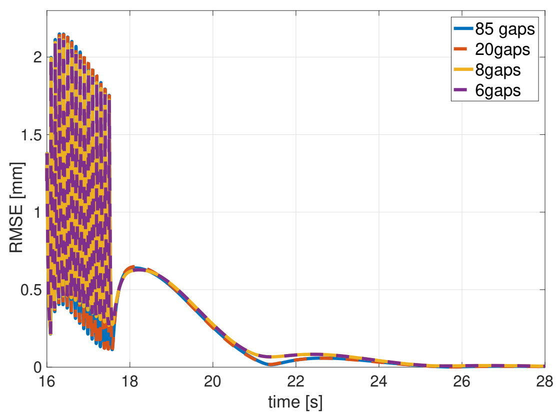

Figure 3.13.: RMSE time traces for the different gaps selections in the presence of Disturbance #2 (compound ELMs). For all the considered cases, the RMSE is computed on the set of 85 gaps shown in figure 3.5.

It should be also noticed that the 6 gaps option considered in [51] gives better performance than the set of 8 gaps chosen in [50]. Indeed, with the latter set, there is a worse control of the plasma top region, as shown in figure 3.15b. Moreover, for the two options with 85 and 20 equally spaced gaps there is no practical difference between the reference shape and the one attained at steady-state. The fact that there is no practical improvement in controlling 85 gaps rather than 20, can be better understood recalling that $\bar{n} < n_{PF}$ singular values are used to compute the control matrix as the pseudo-inverse $C^{\dagger}$ in (3.1). In particular, only the singular values that are greater than the 5% of the greatest one are used to compute $C^{\dagger}$.

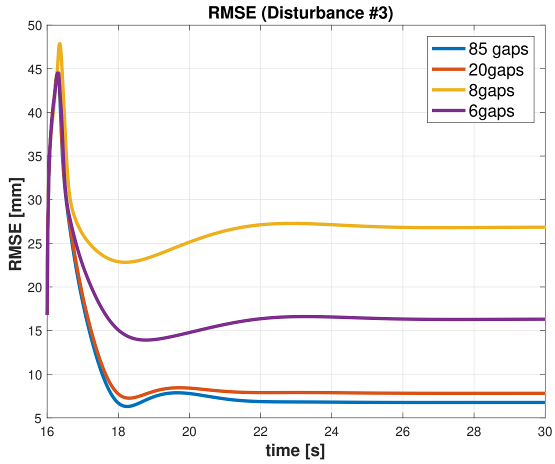

Figure 3.14.: RMSE time traces for the different gaps selections in the presence of Disturbance #3 (Minor disruption). For all the considered cases, the RMSE is computed on the set of 85 gaps shown in Fig. 3.5.

3.5.3 *Isoflux XSC and QST controller*

As mentioned in the previous section, simulations with an isoflux control approach using the CREATE linearized model and the XSC along with the QST reconstruction and control tools were carried out. The same three disturbances (see figure 3.9, 3.10 and 3.11) and JT60-SA equilibrium scenario from the simulations in last section were used for these test cases for a different number of control points. Due to the vast extension of results, this section will focus on analyze the case for 8 control points in the presence of a Minor disruption with the XSC and the QST controller. Figure 3.16 shows the control points configurations used for carrying out the simulations with an isoflux shape controller as well as the LCFS's reconstructed by CREATE and the CCS method at steady-state in the presence of a Minor disruption(Disturbance #3).

For the control and reconstruction points configurations a selection of 19 equally spaced descriptors was used (see figure 3.16a), along with the previous 8 and 6 points configurations used for the gap controller. As mentioned before, the CCS method allows a maximum of 19 points for the fluxes reconstruction and the QST controller a maximum of 10 control points,due to these limitations the 19 segments scenario is only feasible using the XSC.

Figure 3.17 compares the steady-state LCFS's for the same disturbance and equilibrium using both controllers, at first glance it is not possible to identify any visible difference between the two controllers, which allows a first conclusion that both controls reject the disturbance and maintain the reference plasma shape in steady-state. For further study in figures 3.18a and 3.18b is presented the behavior of both controllers at the time instant where their fluxes errors are on their highest value, this happens around 2 ms for the case of the XSC and 65 μs for the QST control after the Minor disruption takes place. From these figures is possible to observe that there is a noticeable plasma shape difference in

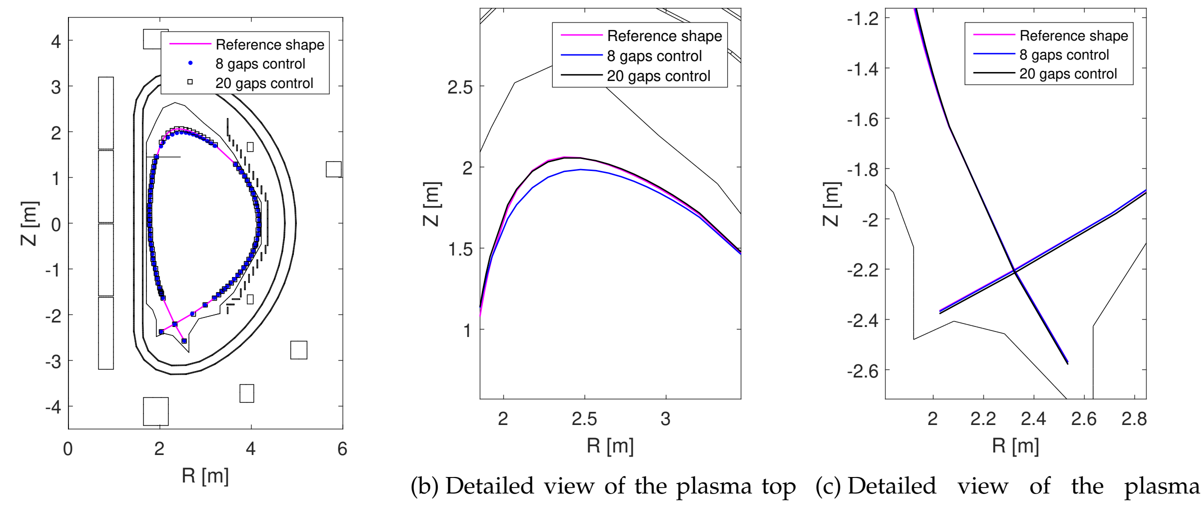

(a) Poloidal cross-section of JT-60SA.

(b) Detailed view of the plasma top region.

(c) Detailed view of the plasma divertor region.

Figure 3.15.: Comparison of the shape controller performance in the presence of Disturbance #3 (Minor disruption). The two cases of 8 and 20 gaps are considered.

comparison with the one from the equilibrium, specially on the radial outer region and secondly is visible that the difference between the equilibrium and the steady-sate shape is smaller for the QST controller case.

Figure 3.19 shows the time traces comparing the flux at the X-point and the 8 control points fluxes, for the XSC and the QST control cases. From these two graphs is noticeable that the QST controller takes around 0.5 s more to reach the steady-state after the disturbance takes place than XSC , but the fluxes at the control points reach a state-state flux value way closer to the X-point flux than the fluxes using the XSC for the simulation, in addition figure 3.20 shows the flux error time traces on the 8 control points for both controllers, on these plots is worth to mention that additionally to a smaller state-state error using the QST control, the maximum error values which are located right after the disturbance takes place are higher for the simulation using the XSC.

In order to summarize all the results from the tested cases, tables 3.3 , 3.5 and 3.7 outline the control points fluxes RMSE and tables 3.3, 3.5 and 3.7 present the X-point radial and vertical position errors in steady-state, these tables summarize results for all the different number of control points with the three different disturbances. Some of the main aspects that are possible to conclude from the tables results are :

(a) For all disturbances the 8 control points selection has the biggest fluxes and X-point position steady-state errors while the cases with 19 control points the lesser ones.

(b) Disturbance #2 (Compound ELM) results present the lesser flux RMSE values in comparison with the other two disturbances. See table 3.4.

(c) The simulations using the QST controller present practically a flux RMSE equal to zero in steady-state for all disturbances while the XSC does not.

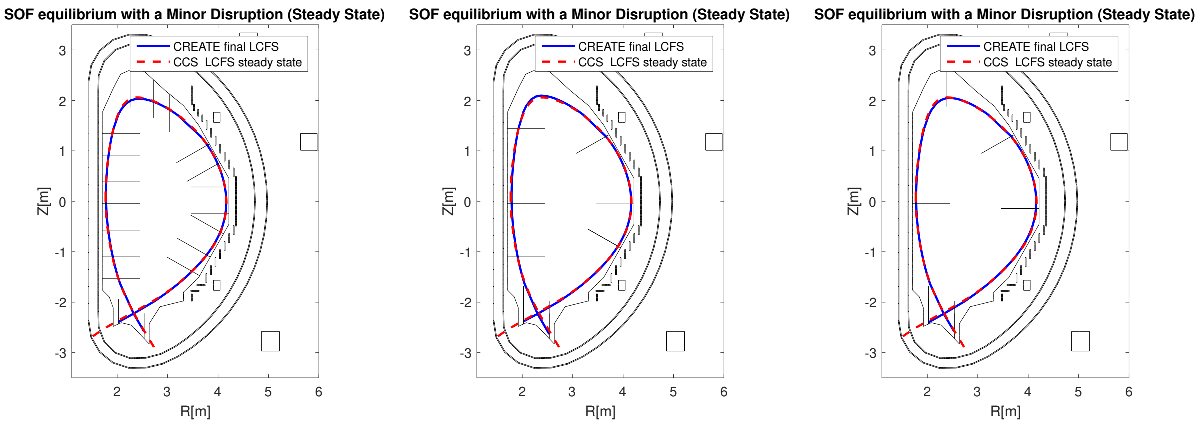

(a) The 19 control segments used to assess the performance of plasma shape controller.

(b) The 8 control segments by the isoflux controller proposed in [50].

(c) The 6 control segments used by the isoflux controller proposed in [51].

Figure 3.16.: LCFS reconstructed by CREATE and the CCS code for the JT60-SA scenario 2 SOF equilibrium with a Minor disruption at steady-state for the three considered selection of control segments using the XSC with an isoflux approach.

Disturbance #1 flux RMSE steady state Wb/2π				
Controller	eXtreme Shape Controller		QST Controller	
LCFS reconstruction method	CCS	CREATE	CCS	CREATE
6 points	0.0116	0.0133	~ 0	~ 0
8 points	0.0166	0.0181	~ 0	~ 0
19 points	0.0085	0.0088		

Table 3.2.: Steady-state flux RMSE values for the different selection of control points for the JT60-SA scenario 2, SOF equilibrium in the presence of Disturbance #1 at $t \sim 20$ s.

(d) For all the scenarios the vertical XSC X-point error is at least %30 greater than the radial position error, while for the QST control the vertical position error tends to be around %50 lesser than the radial position.

(e) As mentioned on the previous section and as it can be observe on the scheme in figure 3.7, the XSC isoflux approach also controls the X-point position, this is noticeable for all the disturbances with 8 control points, where the vertical and horizontal position error values with the QST controller are at least 50% greater than the ones with the XSC .

(f) Despite the X-point control dynamics embedded on the XSC, for the 6 control points scenarios, the radial X-point error positions are similar between the XSC and the QST control simulations, and the vertical X-point error using the XSC is for all disturbances at least 10 times greater than the simulations with the QST controller.

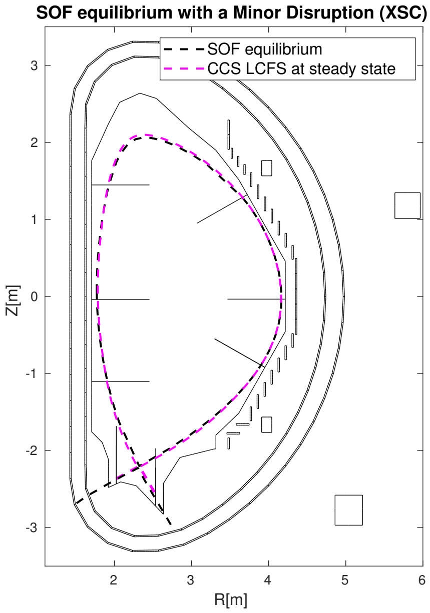

(a) Comparison between the reference shape (i.e., the shape at the considered equilibrium) and the LCFS reconstructed by the CCS code at steady-state in the presence of the Minor disruption using the XSC for the plasma shape, when 8 control segments are considered.

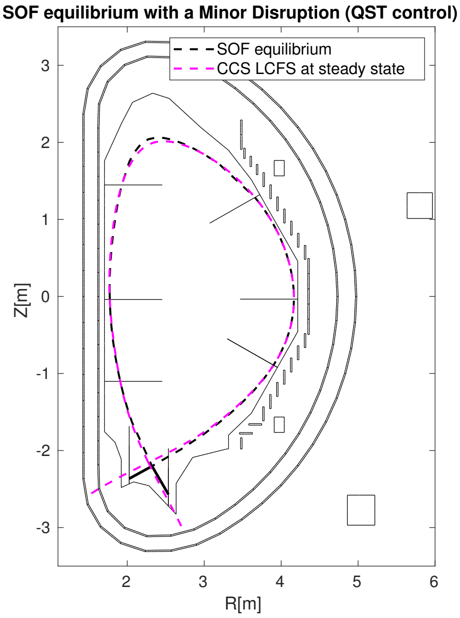

(b) Comparison between the reference shape (i.e., the shape at the considered equilibrium) and the LCFS reconstructed by the CCS code at steady-state in the presence of a Minor disruption using the QST controller for the plasma shape and current and 8 control segments .

Figure 3.17.: CREATE-NL JT60-SA Scenario 2 - SOF equilibrium compared with the LCFS reconstructed by the CCS method for 8 control points in the presence of a Minor disruption at steady-state using both the XSC and the QST control.

3.5.4 *Shape reference change*

A change in the plasma shape for the Scenario 2 - SOF equilibrium has been also considered. In this test scenario closed-loop simulations with the CCS reconstruction method and the isoflux XSC for the plasma shape were performed. Since the configuration with 8 control points seems to be for all cases the one most challenging due to the error values in steady-state obtained on the past subsection, these selection of control points was used for this simulation. The transition time from the initial shape to the target was set equal to 1.5 s. Figure 3.21 shows the equilibrium LCFS (Scenario 2 -SOF), the desired target shape and the LCFS at steady state reconstructed by the CCS method. It can be noticed that the controller is able to track the required shape with negligible error at steady-state, taking $\sim 6\ s$ to reach to it. Figure 3.22 shows the time traces for the fluxes at the 8 control points compared with the X-point flux and figure 3.23 shows the correspondent control flux errors.

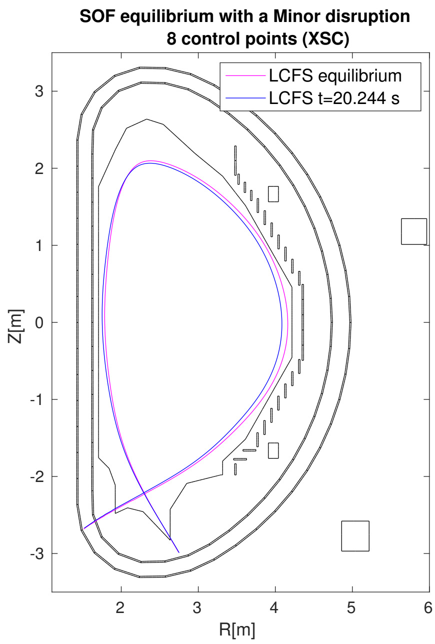

(a) Maximum deviation in plasma shape at t=20.244 s using the XSC for plasma shape.

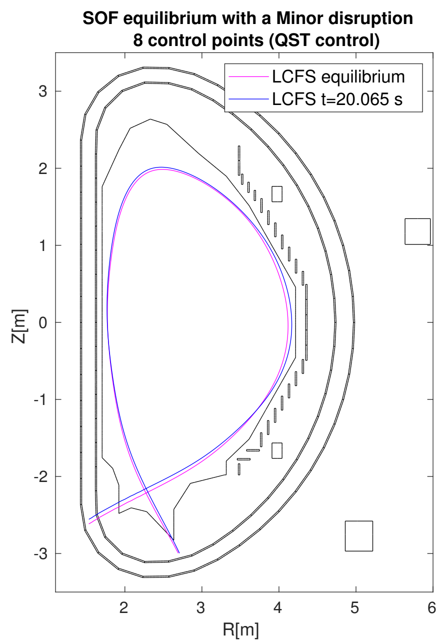

(b) Maximum deviation in plasma shape at t=20.065 s using the QST control for plasma shape.

Figure 3.18.: CREATE-NL JT60-SA Scenario 2 - SOF equilibrium compared with the LCFS reconstructed by the CCS method for 8 control points in the presence of a Minor disruption (Disturbance #3) at the time of maximum deviation for both cases. As shown in figure 3.11, the disturbance occurs at $t \sim 20\ s$

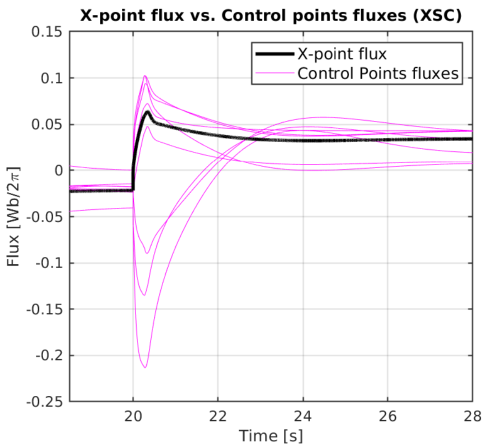

(a) X-point flux compared to the control points fluxes using the XSC.

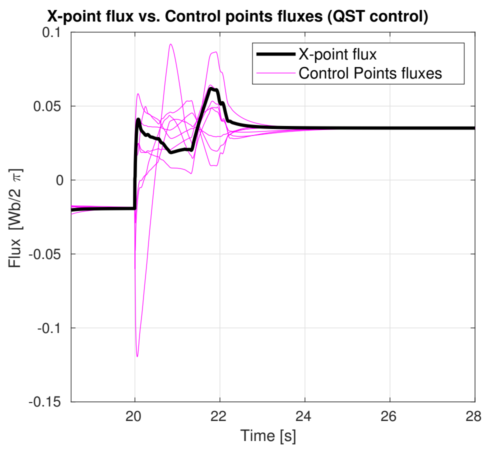

(b) X-point flux compared to the control points fluxes using the QST controller.

Figure 3.19.: Comparison between the flux at the X-point and the fluxes in the 8 control points reconstructed by the CCS method, when a Minor disruption is applaied at t=20 s using the XSC and the QST controller. It should be notice that QST control has a faster performance to reach the steady-state and less error.

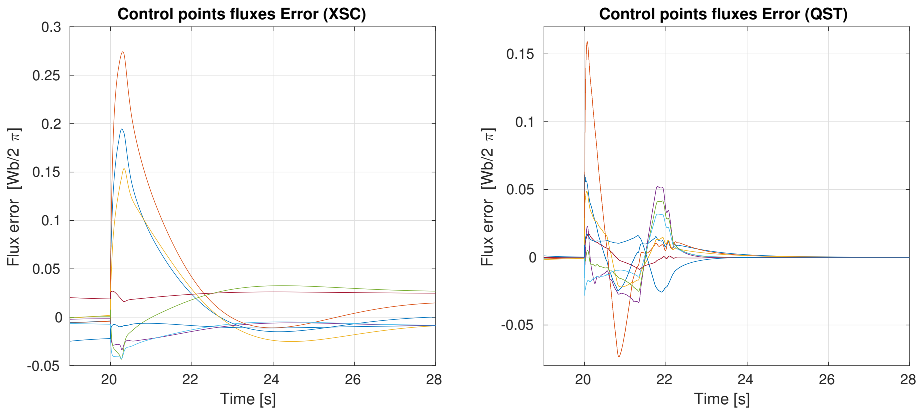

(a) Flux errors using the XSC for 8 control points in the presence of a Minor disruption starting at $t = 20$.

(b) Flux errors using the QST controller for 8 control points in the presence of a Minor disruption starting at $t = 20$.

Figure 3.20.: Flux errors for the case of 8 control points in the presence of a Minor disruption using the XSC and the QST controller. Even though both controllers reject the disturbance, is possible to remark how the QST control has an overall smaller error.

Disturbance #1 steady state X-point position error								
Controller	eXtreme Shape Controller				QST Controller			
LCFS reconstruction method	CCS		CREATE		CCS		CREATE	
	Rx mm	Zx mm	Rx mm	Zx mm	Rx mm	Zx mm	Rx mm	Zx mm
6 points	-4.606	19.96	-3.576	28.16	-1.434	-0.843	-1.16	-0.316
8 points	18.58	21.95	18.96	29.82	49.16	-46.52	59.66	-40.92
19 points	2.62	12.84	2.375	20.51				

Table 3.3.: X-point position steady state error for JT60-SA scenario 2, SOF equilibrium in the presence of Disturbance #1 at $t \sim 20$ s . The XSC and QST controller were used in different simulations for the shape control along with two reconstruction methods for the LCFS.

Disturbance #2 (Compound ELM) flux RMSE steady state Wb/2π				
Controller	eXtreme Shape Controller		QST Controller	
LCFS reconstruction method	CCS	CREATE	CCS	CREATE
6 points	0.0014	0.0022	~ 0	~ 0
8 points	0.0104	0.0101	~ 0	~ 0
19 points	0.0023	0.0028		

Table 3.4.: Steady-state flux RMSE values for the different selection of control points for the JT60-SA scenario 2, SOF equilibrium in the presence of Disturbance #2 (Compound ELM) at $t \sim 20$ s.

Disturbance #2 (Compound ELM) steady state X-point position error								
Controller	eXtreme Shape Controller				QST Controller			
LCFS reconstruction method	CCS		CREATE		CCS		CREATE	
	Rx mm	Zx mm	Rx mm	Zx mm	Rx mm	Zx mm	Rx mm	Zx mm
6 points	0.3968	-2.455	1.3	2.556	-0.481	-0.267	-0.019	0.0143
8 points	15.72	-8.41	16.61	-3.098	50.18	-43.25	54.44	-32.68
19 points	-0.0007	0.0237	-0.1916	-4.69				

Table 3.5.: X-point position steady state error for JT60-SA scenario 2, SOF equilibrium in the presence of Disturbance #2 (Compound ELM) at $t \sim 20$ s . The XSC and QST controller were used in different simulations for the shape control along with two reconstruction methods for the LCFS.

Disturbance #3 (Minor disruption) flux RMSE steady state $\mathbf{Wb/2\pi}$				
Controller	eXtreme Shape Controller		QST Controller	
LCFS reconstruction method	CCS	CREATE	CCS	CREATE
6 points	0.0121	0.0139	~ 0	~ 0
8 points	0.0152	0.0170	~ 0	~ 0
19 points	0.0069	0.0088		

Table 3.6.: Steady-state flux RMSE values for the different selection of control points for the JT60-SA scenario 2, SOF equilibrium in the presence of Disturbance #3 (Minor disruption) at $t \sim 20$ s.

Disturbance #3 (Minor disruption) steady state X-point position error								
Controller	eXtreme Shape Controller				QST Controller			
LCFS reconstruction method	CCS		CREATE		CCS		CREATE	
	Rx mm	Zx mm	Rx mm	Zx mm	Rx mm	Zx mm	Rx mm	Zx mm
6 points	-4.92	20.9	-3.57	28.8	-2.70	-0.105	-2.24	0.369
8 points	17.44	21.56	17.81	29.04	47.08	-46.56	57.61	-41.42
19 points	-5.54	16.78	-4.42	24.41				

Table 3.7.: X-point position steady state error for JT60-SA scenario 2, SOF equilibrium in the presence of Disturbance #3 (Minor disruption) at $t \sim 20$ s . The XSC and QST controller were used in different simulations for the shape control along with two reconstruction methods for the LCFS.

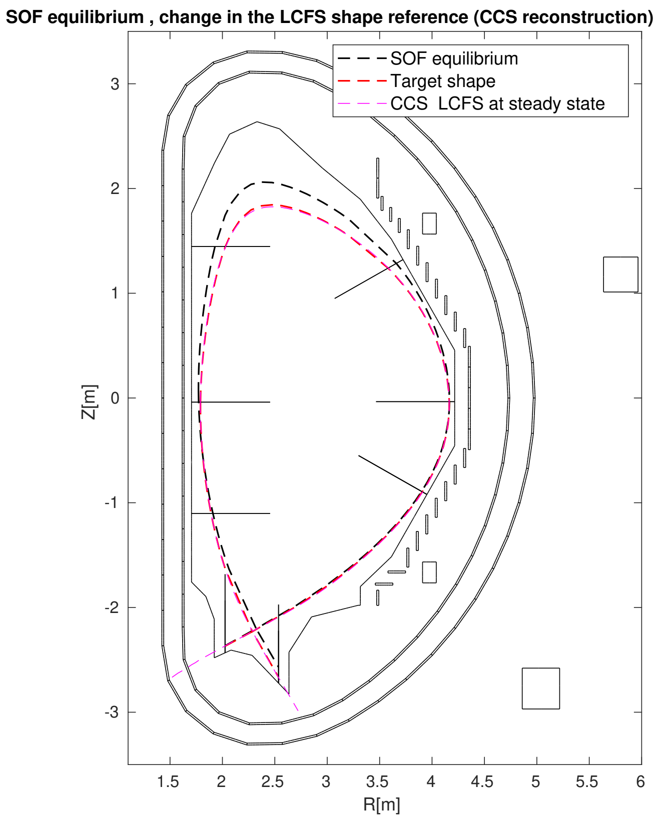

Figure 3.21.: XSC isoflux response to a change of shape request. The dashed black shape is the starting shape, while the red one is the target shape. The magenta dashed shape is the LCFS at steady state.

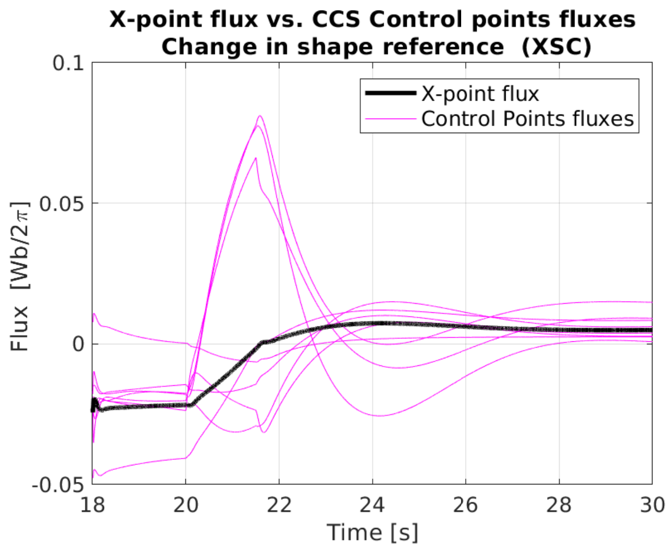

Figure 3.22.: Comparison between the flux at the X-point and the fluxes a

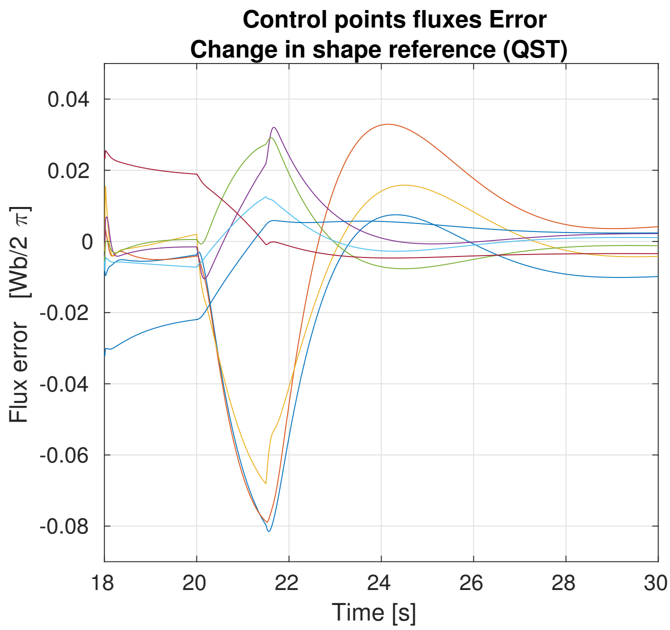

Figure 3.23.: Flux control error for the case of 8 control points for a change in the shape reference between 20 and 21.5 s.

4

ISTTOK

4.1 MACHINE DESCRIPTION

Figure 4.1.: Actual ISTTOK vaccum vessel section with ports.

4.2 DIAGNOSTICS AND ACTUATORS

4.3 ATCA-MIMO-ISOL BOARDS

4.3.1 *Hardware layout*

4.3.2 *Real-time integration software*

4.4 PLASMA CURRENT MAGNETIC FIELD

Retrieving the contribution of the plasma current in tokamaks ...

The methods of correction of the magnetic error fields due to inaccuracies of tokamak manufacturing and assembly are considered. The problems of the plasma position and shape reconstruction based on magnetic field measurements are discussed.

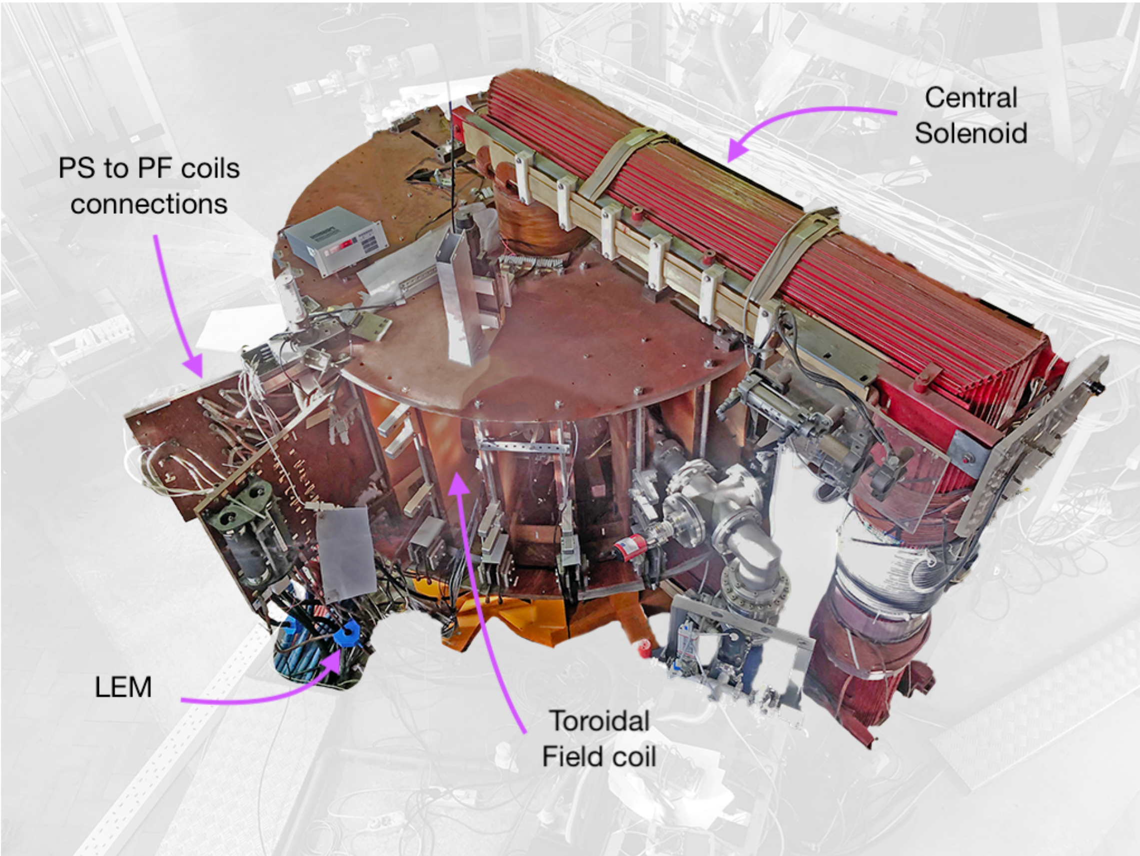

Figure 4.2.: ISTTOK top view in 2020, main elements are indicated with magenta lines.

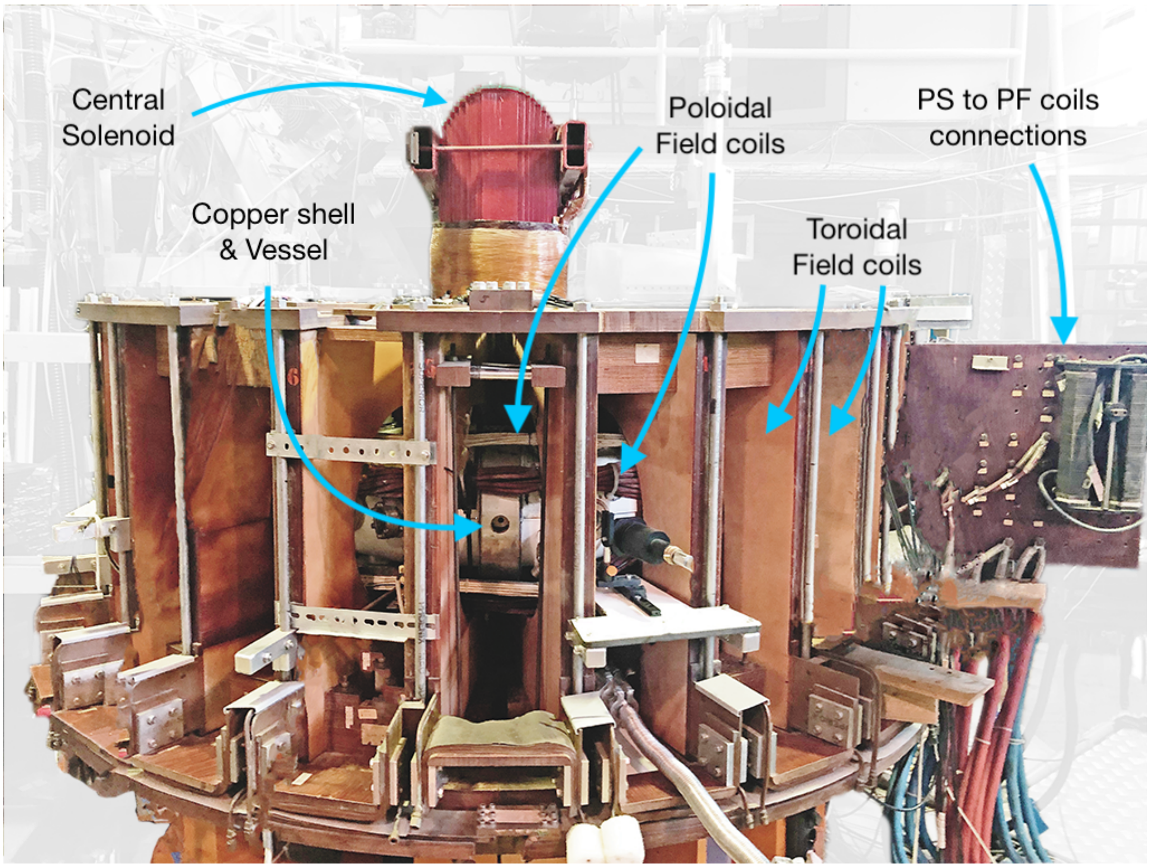

Figure 4.3.: ISTTOK frontal view in 2020, main elements are indicated with blue lines.

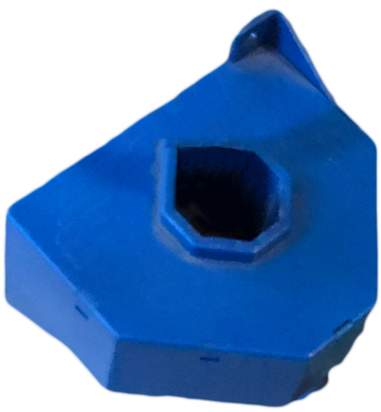

Figure 4.4.: LEM

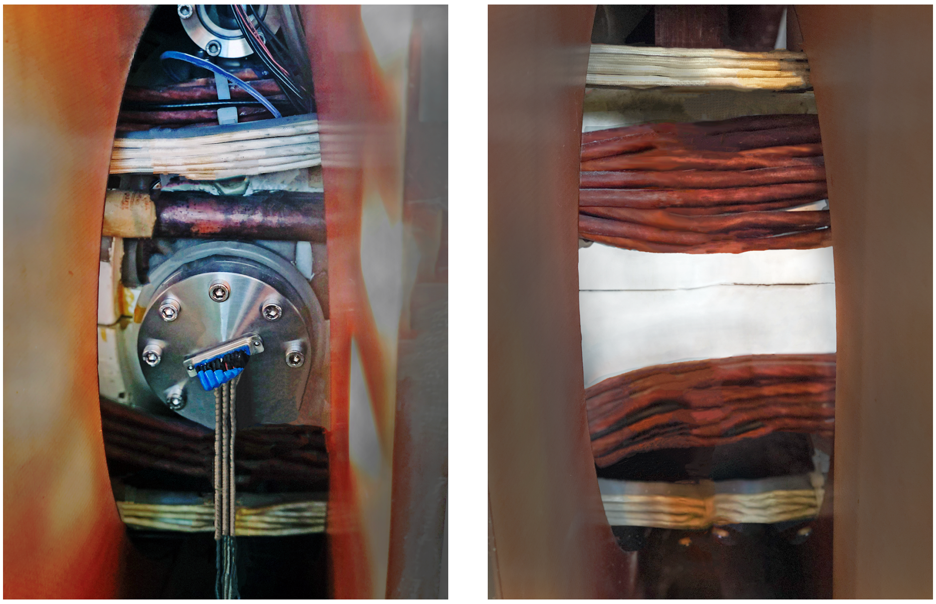

(a) Magnetic probes port whith connection cable to the ATCA adquisition boards, also PF coils and cooper shell are shown.

(b) PF coils close up,primary coils correspond to the white cables and vertical and horizontal to the orange ones.

Figure 4.5.: ISTTOK close up side views.

4.5 PLASMA CENTROID POSITION DETERMINATION

5

ISTTOK RESULTS

This chapter describes the latest implementations in ISTTOK MARTe framework followed by the presentation of the obtained results for control of the current centroid position.

5.1 IMPLEMENTATION OF THE GENERAL APPLICATION MODULES

General Application Modules (GAM)

5.1.1 *PID control implementation*

Proportional-Integrative-Derivative

5.1.2 *Data-driven state-space model retrieving*

Early efforts in finding a real-time equilibrium solver for ISTTOK were performed in the last years. Due to the geometrical conditions it was never retrieve a

5.1.3 *Kalman filter implementation*

5.1.4 *Multiple-Input Multiple-Output control implementation*

5.2 PLASMA CURRUENT CENTROID POSITION CONTROL RESULTS

This section addresses the latest results from the real-time implementation of control algorithms in ISTTOK.

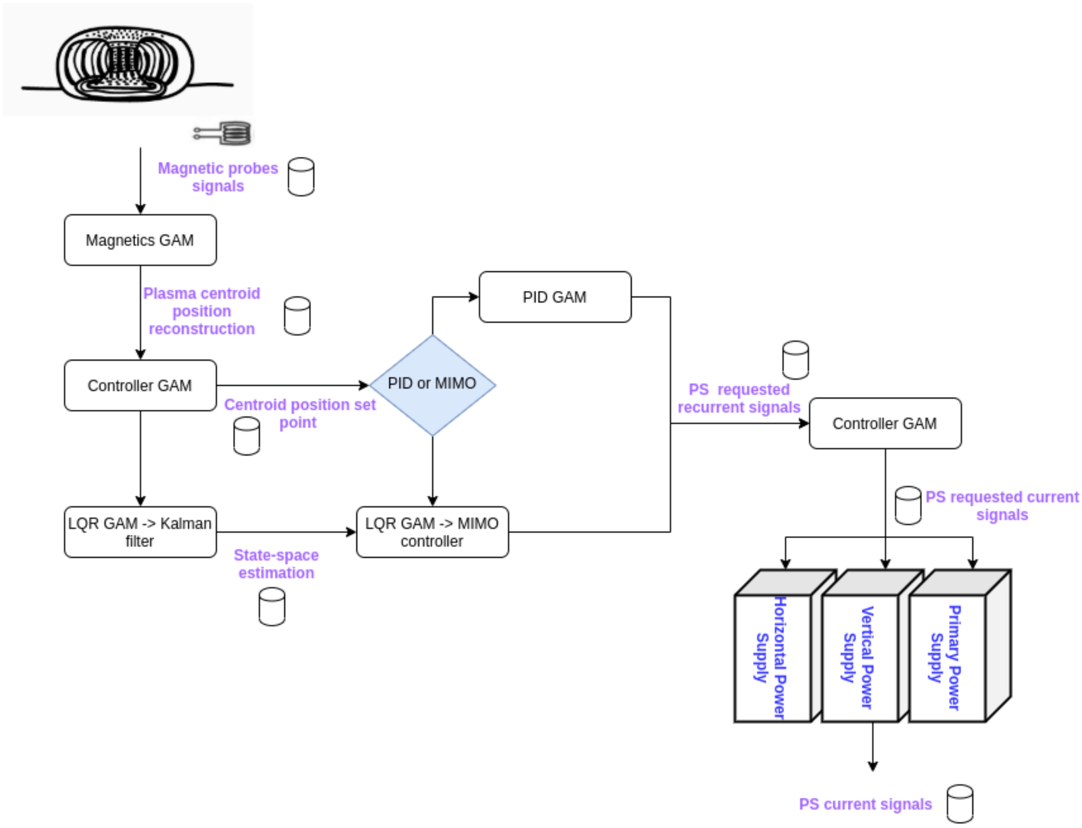

Figure 5.1.: ISTTOK MARTe overall control position scheme

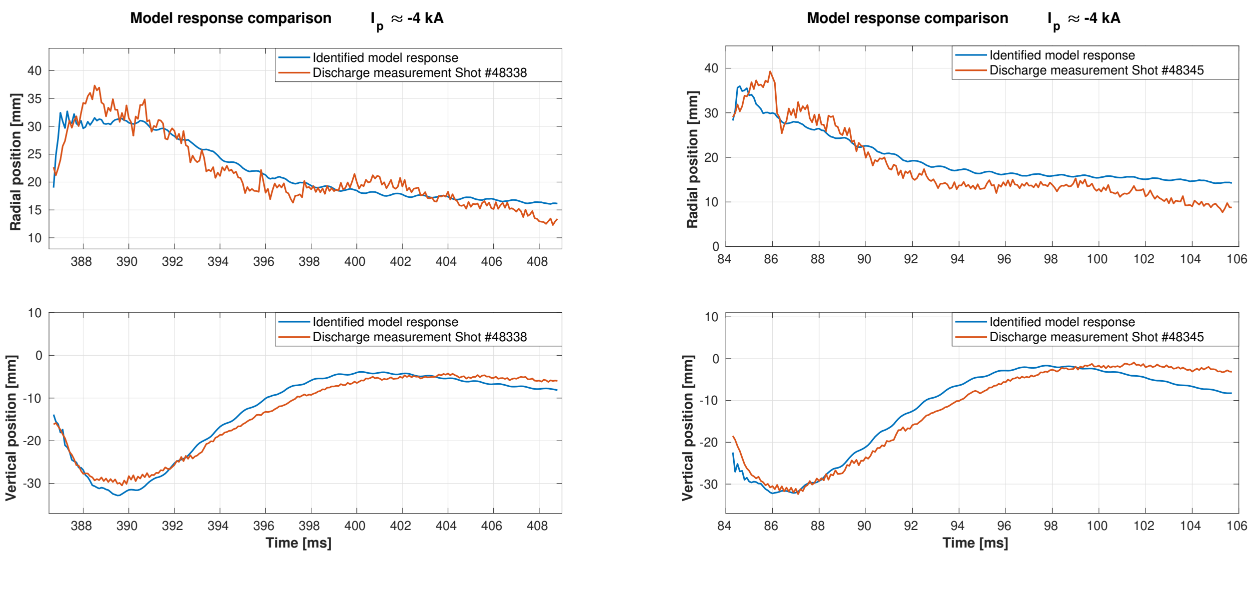

(a) (b)

Figure 5.2.: Fig.

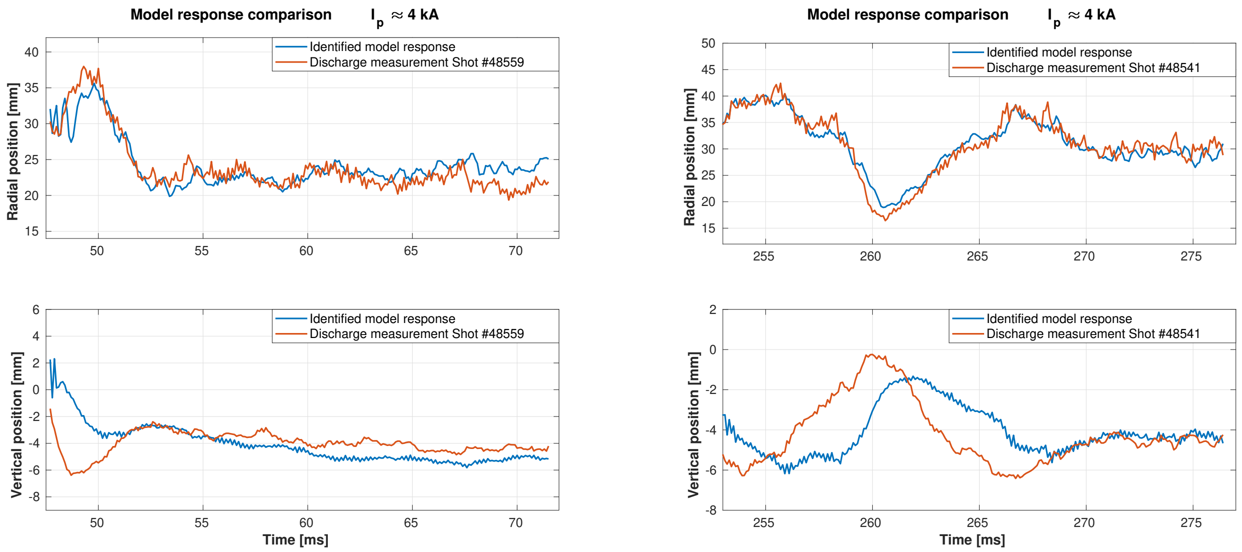

(a) (b)

Figure 5.3.: Fig.

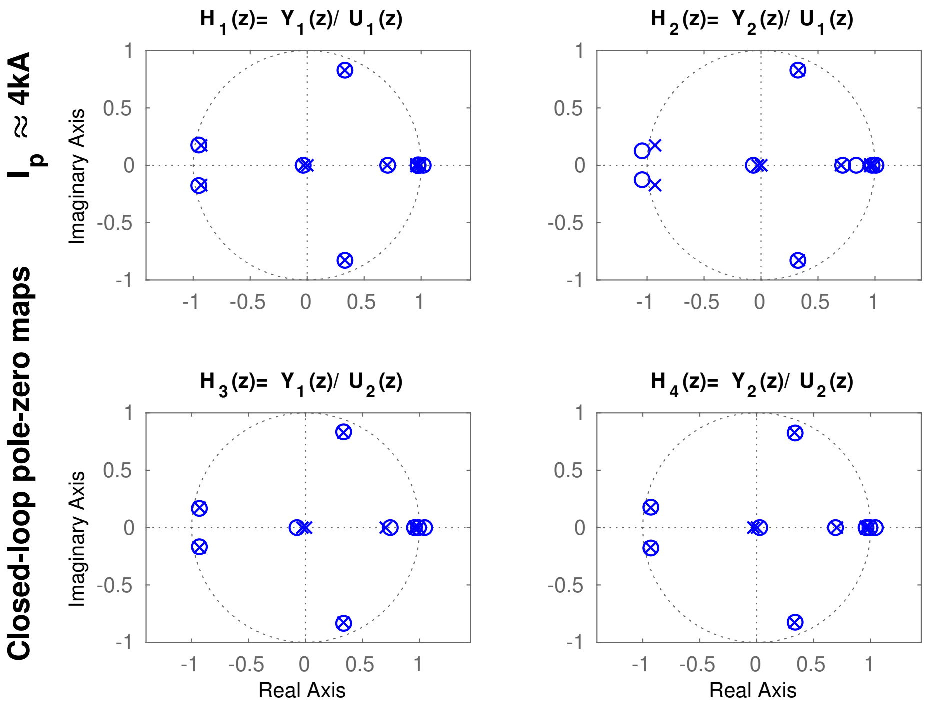

Figure 5.4.: Pole-Zero maps in closed loop for the model when $I_p \approx 4kA$. Superposition of poles and zeros can be seen in the four transfer functions.

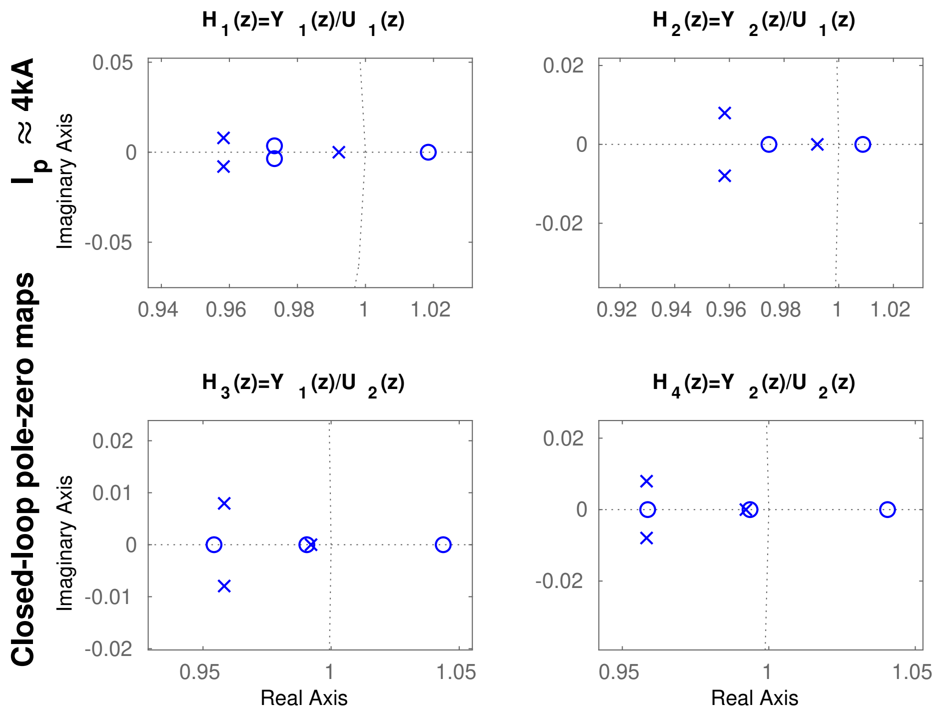
Closed-loop pole-zero maps
Ip ≈ 4kA
H1(z)=Y1(z)/U1(z)
H2(z)=Y2(z)/U1(z)
H3(z)=Y1(z)/U2(z)
H4(z)=Y2(z)/U2(z)
Imaginary Axis
Real Axis

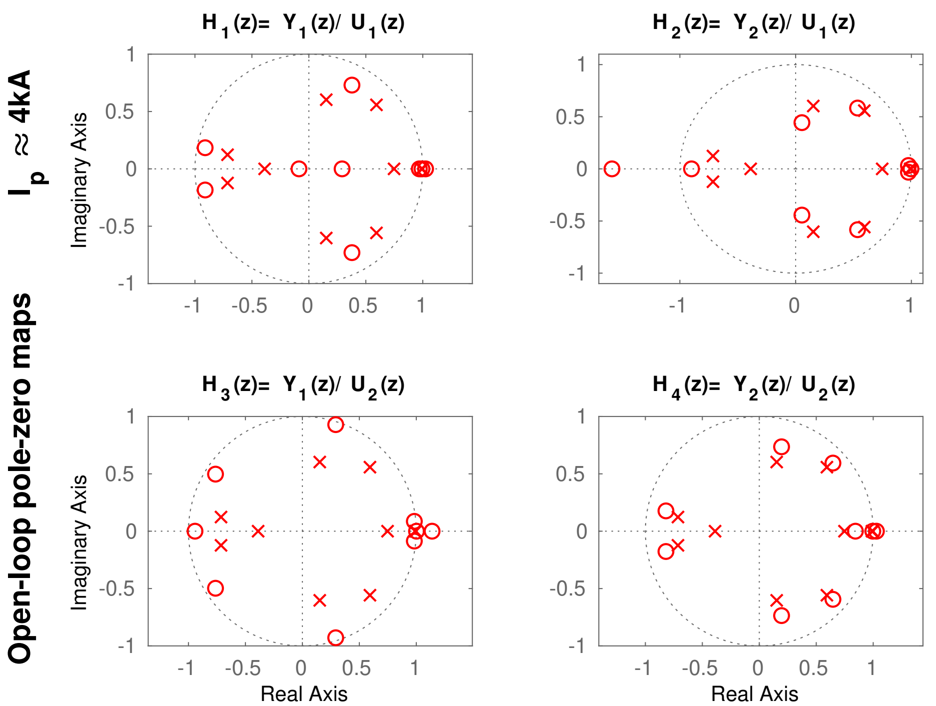
Open-loop pole-zero maps
Ip ≈ 4kA
H1(z)= Y1(z)/ U1(z)
H2(z)= Y2(z)/ U1(z)
H3(z)= Y1(z)/ U2(z)
H4(z)= Y2(z)/ U2(z)
Imaginary Axis
Real Axis

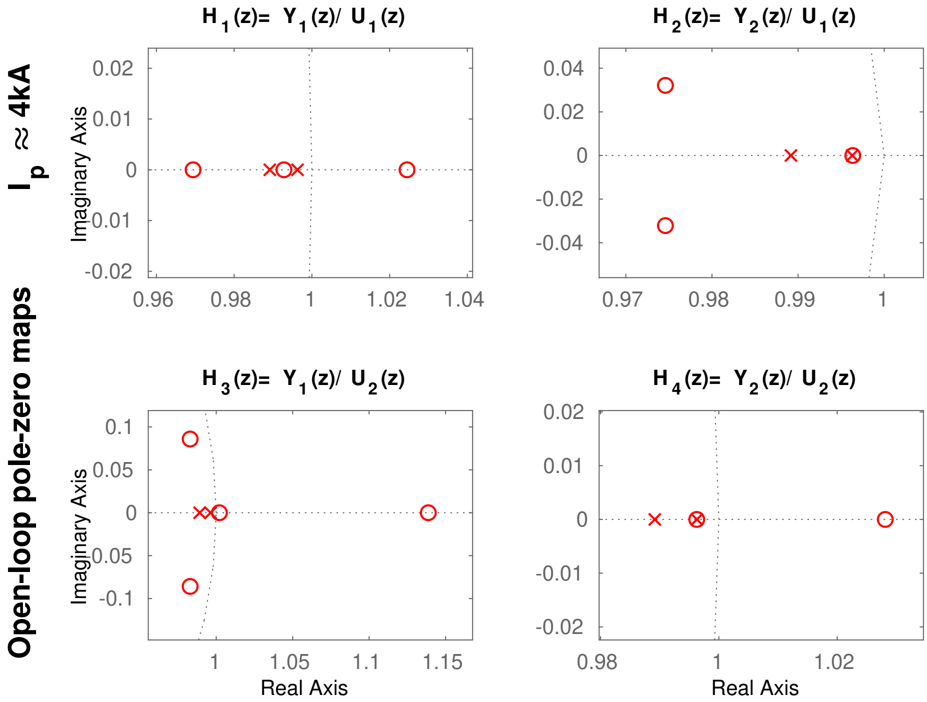
Open-loop pole-zero maps
$I_p \approx 4$kA
$H_1(z) = Y_1(z)/U_1(z)$
$H_2(z) = Y_2(z)/U_1(z)$
$H_3(z) = Y_1(z)/U_2(z)$
$H_4(z) = Y_2(z)/U_2(z)$
Imaginary Axis
Real Axis

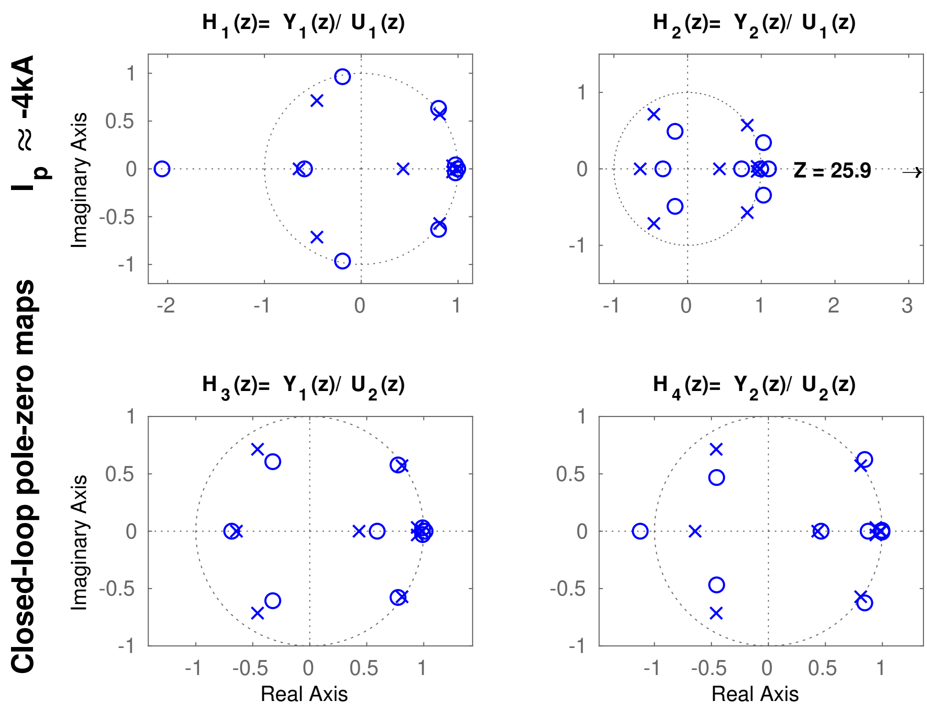
Closed-loop pole-zero maps
$I_p \approx -4$kA
$H_1(z) = Y_1(z)/U_1(z)$
$H_2(z) = Y_2(z)/U_1(z)$
Z = 25.9
$H_3(z) = Y_1(z)/U_2(z)$
$H_4(z) = Y_2(z)/U_2(z)$
Imaginary Axis
Real Axis

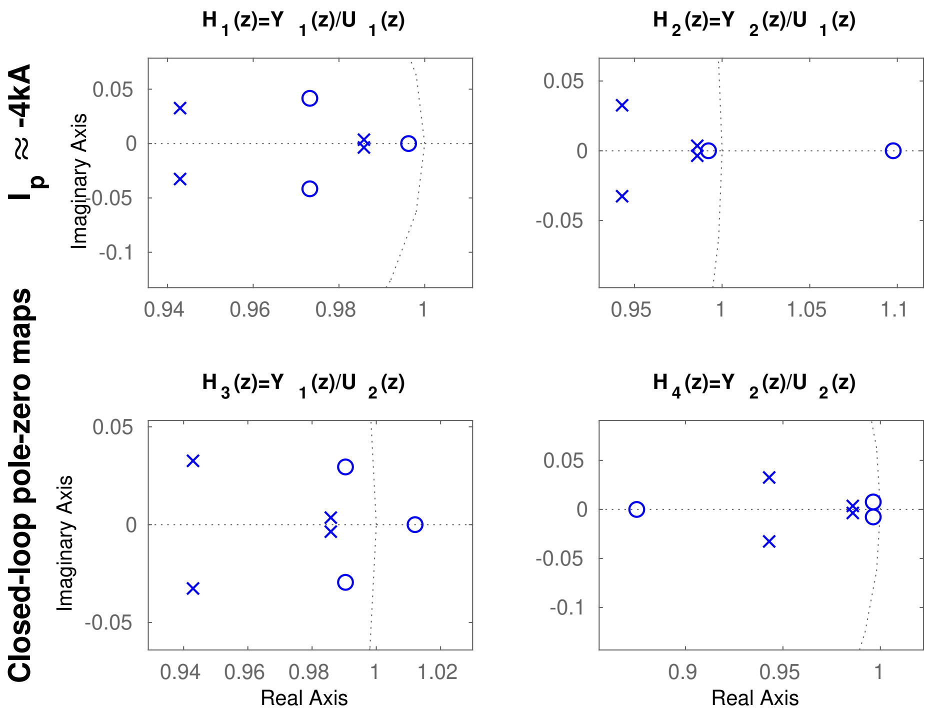
Closed-loop pole-zero maps
$I_p \approx$ -4kA
$H_1(z)=Y_1(z)/U_1(z)$
$H_2(z)=Y_2(z)/U_1(z)$
$H_3(z)=Y_1(z)/U_2(z)$
$H_4(z)=Y_2(z)/U_2(z)$
Imaginary Axis
Real Axis

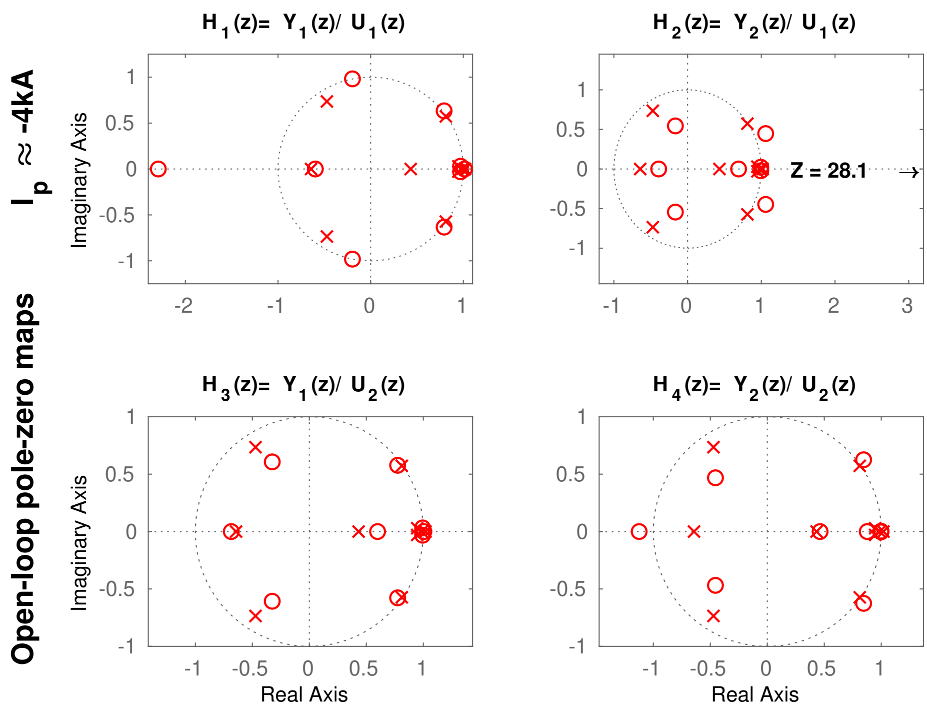
Open-loop pole-zero maps
$I_p \approx$ -4kA
$H_1(z)= Y_1(z)/ U_1(z)$
$H_2(z)= Y_2(z)/ U_1(z)$
Z = 28.1
$H_3(z)= Y_1(z)/ U_2(z)$
$H_4(z)= Y_2(z)/ U_2(z)$
Imaginary Axis
Real Axis

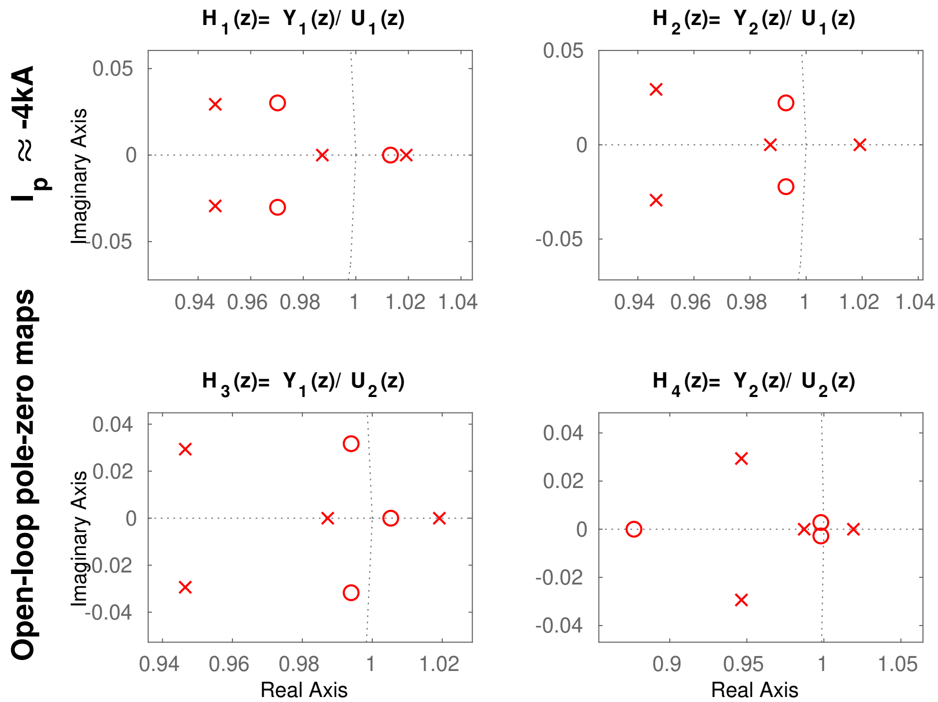

5.2.1 *PID control and LQR control results*

This section addresses obteined the experimental results in ISTTOK's plasma discharges.

Control	Shot #	RMSE (R,z) mm	Set point (R,z) mm	I_p
PID	48564	(13.73, 4.4102)	(24, -5)	$\approx 4kA$
MIMO LQR	48559	(4.2252, 1.4215)	(24, -5)	$\approx 4kA$
PID	48563	(13.6717, 4.1652)	(24, -4)	$\approx 4kA$
MIMO LQR	48561	(8.1047, 3.2752)	(24, -4)	$\approx 4kA$
PID	48556	(12.0315, 3.3217)	(32, -5)	$\approx 4kA$
MIMO LQR	48555	(4.2618, 2.4698)	(32, -5)	$\approx 4kA$
PID	48551	(13.9998, 3.3431)	(27, -5)	$\approx 4kA$
MIMO LQR	48554	(5.9830, 2.0062)	(27, -5)	$\approx 4kA$
PID	48515	(6.0178, 2.6123)	(30, -5)	$\approx 4kA$
MIMO LQR	48541	(5.8372, 1.7664)	(30, -5)	$\approx 4kA$
PID	48544	(4.8745, 2.5167)	(32, -4)	$\approx 4kA$
MIMO LQR	48542	(4.4346, 3.6573)	(32, -4)	$\approx 4kA$
PID	48546	(11.4560, 3.4765)	(27, -7)	$\approx 4kA$
MIMO LQR	48548	(7.6745, 4.1569)	(27, -7)	$\approx 4kA$
PID	48341	(12.0959, 5.7652)	(11, -5)	$\approx -4kA$

MIMO LQR	48324	(15.4768, 14.3436)	(11, -5)	$\approx -4kA$
PID	48340	(11.7701, 5.9599)	(11.2, -5.5)	$\approx -4kA$
MIMO LQR	48338	(11.5260, 12.6226)	(11.2, -5.5)	$\approx -4kA$
PID	48343	(15.7675, 5.7453)	(12, -5)	$\approx -4kA$
MIMO LQR	48342	(14.5168, 14.4329)	(12, -5)	$\approx -4kA$
PID	48346	(12.4228, 6.1541)	(12.2, -5.3)	$\approx -4kA$
MIMO LQR	48345	(9.7513, 13.0338)	(12.2, -5.3)	$\approx -4kA$
PID	48349	(19.3397, 5.5406)	(11.5, -5.6)	$\approx -4kA$
MIMO LQR	48348	(9.1727, 13.1505)	(11.5, -5.6)	$\approx -4kA$
PID	48352	(15.2181, 6.5395)	(10.8, -4.7)	$\approx -4kA$
MIMO LQR	48354	(14.6405, 13.7307)	(10.8, -4.7)	$\approx -4kA$
PID	48351	(13.4078, 5.8769)	(13.2, -5.6)	$\approx -4kA$
MIMO LQR	48350	(13.9320, 14.4940)	(13.2, -5.6)	$\approx -4kA$

Table 5.1.: Centroid position RMSE comparison between PID and MIMO-LQR controlled discharges for different set points and plasma current scenarios.

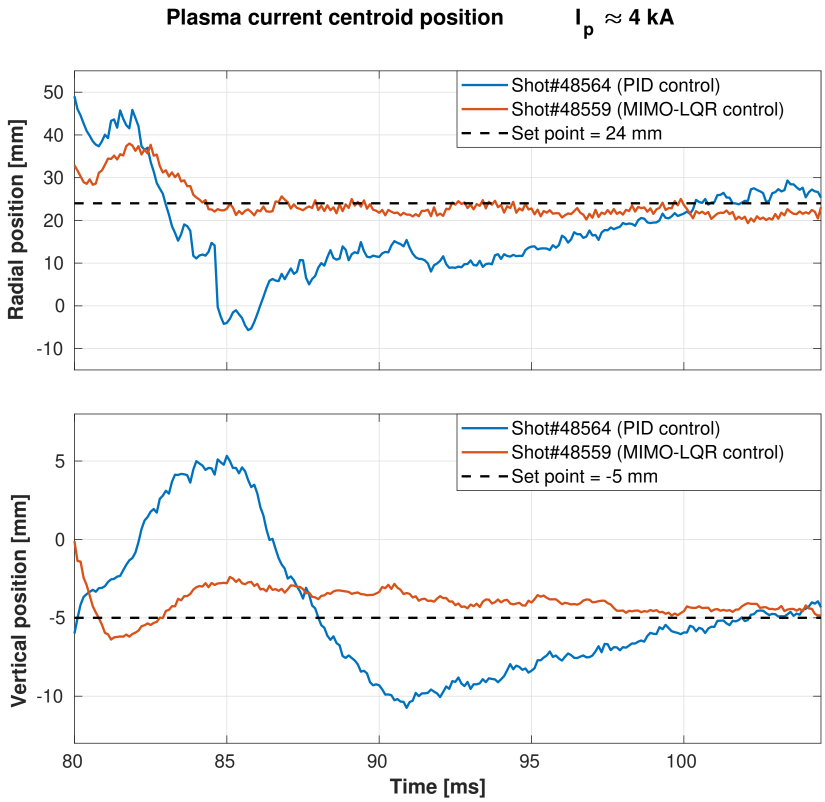
Plasma current centroid position
$I_p \approx 4$ kA
Radial position [mm]
Shot#48564 (PID control)
Shot#48559 (MIMO-LQR control)
Set point = 24 mm
Vertical position [mm]
Shot#48564 (PID control)
Shot#48559 (MIMO-LQR control)
Set point = -5 mm
Time [ms]

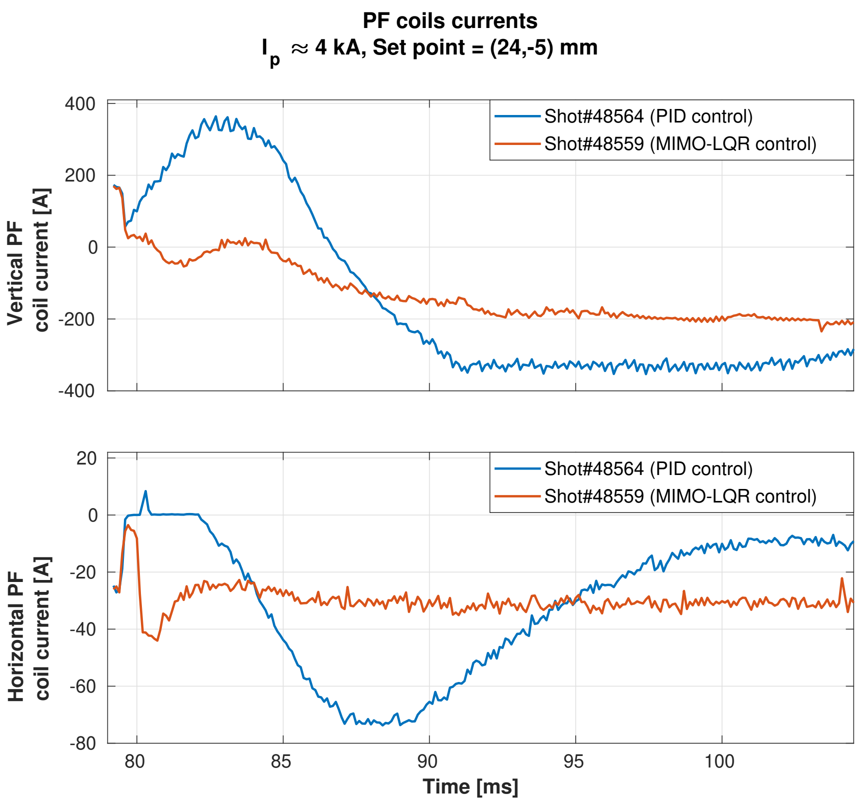
PF coils currents
$I_p \approx 4$ kA, Set point = (24,-5) mm
Vertical PF coil current [A]
Shot#48564 (PID control)
Shot#48559 (MIMO-LQR control)
Horizontal PF coil current [A]
Shot#48564 (PID control)
Shot#48559 (MIMO-LQR control)
Time [ms]

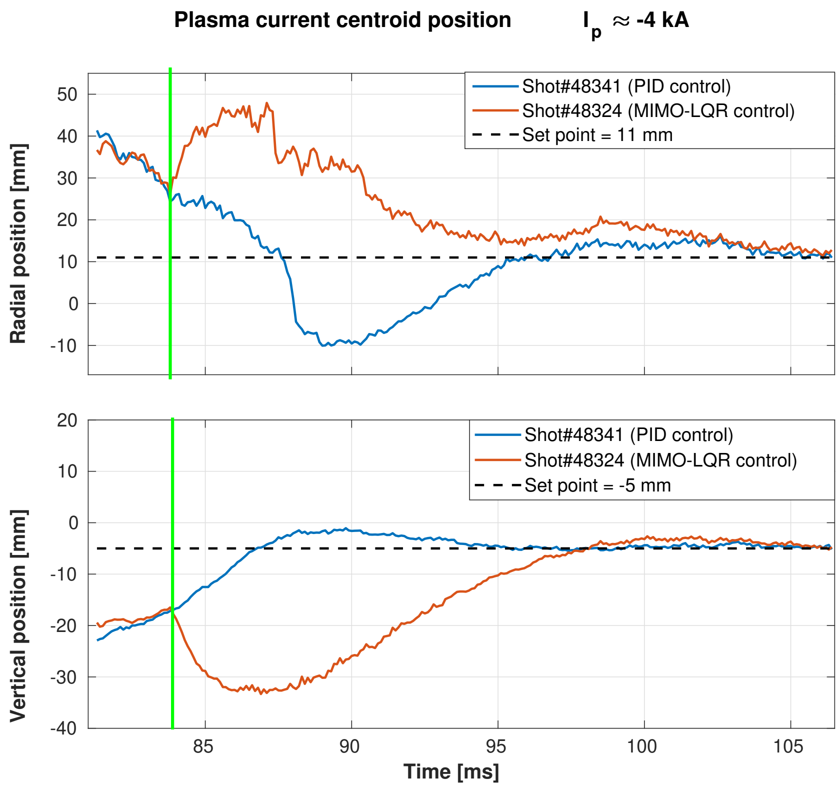
Plasma current centroid position
$I_p \approx$ -4 kA
Shot#48341 (PID control)
Shot#48324 (MIMO-LQR control)
Set point = 11 mm
Radial position [mm]
50
40
30
20
10
0
-10
Shot#48341 (PID control)
Shot#48324 (MIMO-LQR control)
Set point = -5 mm
Vertical position [mm]
20
10
0
-10
-20
-30
-40
85
90
95
100
105
Time [ms]

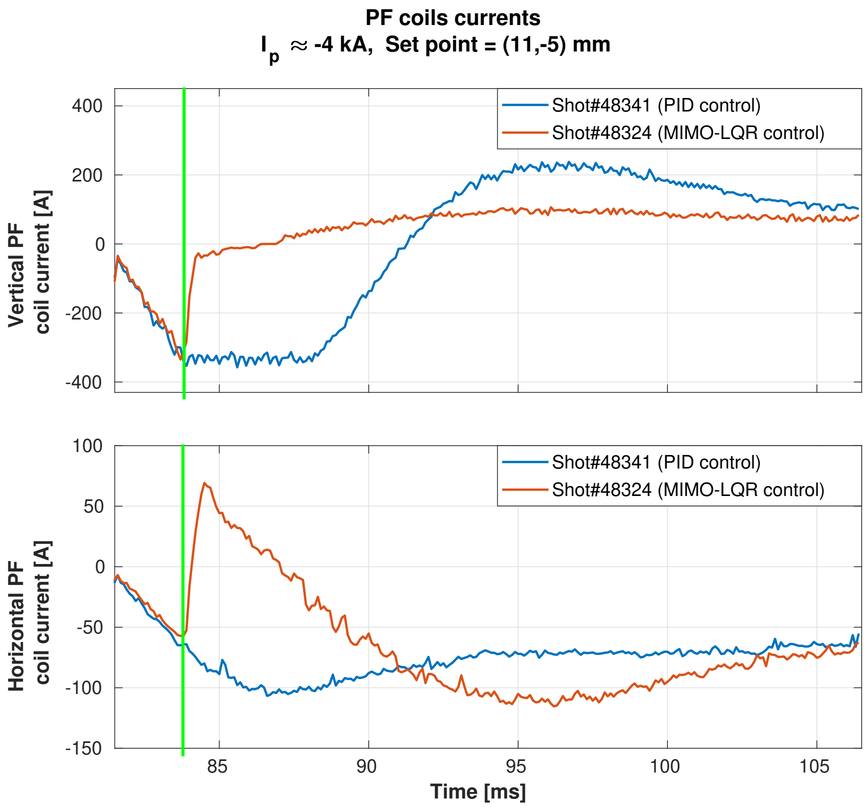
PF coils currents
$I_p \approx$ -4 kA, Set point = (11,-5) mm
Shot#48341 (PID control)
Shot#48324 (MIMO-LQR control)
Vertical PF coil current [A]
400
200
0
-200
-400
Shot#48341 (PID control)
Shot#48324 (MIMO-LQR control)
Horizontal PF coil current [A]
100
50
0
-50
-100
-150
85
90
95
100
105
Time [ms]

6

CONCLUSIONS

bla bla bla

BIBLIOGRAPHY

[1] Andrej A. Kavin Valerij A. Belyakov. *Fundamentals of Magnetic Thermonuclear Reactor Design*. Elsevier, 2018.

[2] F. Janky, M. Hron, J. Havlicek, M. Varavin, F. Zacek, J. Seidl, and R. Panek. Plasma density control in real-time on the COMPASS tokamak. *Fusion Engineering and Design*, 96-97:637–640, 2015.

[3] J. R. Ferron, A. Kellman, E. McKee, T. Osborne, P. Petrach, T. S. Taylor, J. Wight, and E. Lazarus. An advanced plasma control system for the diii-d tokamak. In *[Proceedings] The 14th IEEE/NPSS Symposium Fusion Engineering*, pages 761–764 vol.2, Sep. 1991.

[4] B. G. Penaflor, J. R. Ferron, A. W. Hyatt, M. L. Walker, R. D. Johnson, D. A. Piglowski, E. Kolemen, A. S. Welander, and M. J. Lanctot. Latest advancements in DIII-D Plasma Control software and hardware. *2013 IEEE 25th Symposium on Fusion Engineering, SOFE 2013*, pages 1–4, 2013.

[5] M. Margo, B. Penaflor, H. Shen, J. Ferron, D. Piglowski, P. Nguyen, J. Rauch, M. Clement, A. Battey, and C. Rea. Current State of DIII-D Plasma Control System. *Fusion Engineering and Design*, 150(October 2019), 2020.

[6] Mellanox Technologies. Introduction to InfiniBand. Technical report, 2003.

[7] J. I. Paley, S. Coda, B. Duval, F. Felici, and J. M. Moret. Architecture and commissioning of the TCV distributed feedback control system. *Conference Record - 2010 17th IEEE-NPSS Real Time Conference, RT10*, pages 1–6, 2010.

[8] H. Anand, C. Galperti, S. Coda, B. P. Duval, F. Felici, T. Blanken, E. Maljaars, J. M. Moret, O. Sauter, T. P. Goodman, and D. Kim. Distributed digital real-time control system for the TCV tokamak and its applications. *Nuclear Fusion*, 57(5), 2017.

[9] A. C. Neto, F. Sartori, F. Piccolo, R. Vitelli, G. De Tommasi, L. Zabeo, A. Barbalace, H. Fernandes, D. F. Valcarcel, and A. J. N. Batista. Marte: A multiplatform real-time framework. *IEEE Transactions on Nuclear Science*, 57(2):479–486, April 2010.

[10] G. De Tommasi, F. Piccolo, A. Pironti, and F. Sartori. A flexible software for real-time control in nuclear fusion experiments. *Control Engineering Practice*, 14(11):1387–1393, 2006.

[11] André C. Neto, Diogo Alves, Luca Boncagni, Pedro J. Carvalho, Daniel F. Valcárcel, Antonio Barbalace, Gianmaria De Tommasi, Horácio Fernandes, Filippo Sartori, Enzo Vitale, Riccardo Vitelli, and Luca Zabeo. A survey of recent MARTe based systems. In *IEEE Transactions on Nuclear Science*, volume 58, pages 1482–1489, 2011.

[12] A Neto, D Alves, B B Carvalho, P J Carvalho, H Fernandes, D F Valc, G De Tommasi, Associazione Euratom-enea create, Via Claudio, P Mccullen, A Stephen, Euratom-ccfe Fusion Association, Culham Science Centre, Abingdon Ox, United Kingdom, R Vitelli, Tor Vergata, Via Politecnico, L Zabeo, and Iter Organisation. Marte Framework : a Middleware for Real-Time Applications Development. In *13th International Conference on Accelerator and Large Experimental Physics Control Systems*, number 11, pages 1277–1280, Grenoble, France, 2011.

[13] Yash Gupta. *Software Quality Assurance*, volume 6. 1989.

[14] Andre C. Neto, Filippo Sartori, Riccardo Vitelli, Llorenc Capella, Giuseppe Ferro, Ivan Herrero, and Hector Novella. An agile quality assurance framework for the development of fusion real-Time applications. In *2016 IEEE-NPSS Real Time Conference, RT 2016*, 2016.

[15] I. Neto, A. Herrero. D4 MARTe Project Managment Plan. *F4E Internal Document*, (July):1–4, 2018.

[16] I. Neto, A. Herrero. D4 MARTe Coding Standard. *F4E Internal Document*, (July):1–4, 2018.

[17] I. Neto, A. Herrero. MARTe Quality Assurance Plan. *F4E Internal Document*, (July):1–4, 2018.

[18] V. D. Shafranov and V. S. Mukhovatov. Plasma Equilibrium in a Tokamak. *Nuclear Fusion*, 11(6):605–633, 1971.

[19] L. L. Lao, H. St John, R. D. Stambaugh, A. G. Kellman, and W. Pfeiffer. Reconstruction of current profile parameters and plasma shapes in tokamaks. *Nuclear Fusion*, 25(11):1611–1622, 1985.

[20] M. Fitzgerald, L. C. Appel, and M. J. Hole. EFIT tokamak equilibria with toroidal flow and anisotropic pressure using the two-temperature guiding-centre plasma. *Nuclear Fusion*, 53(11), 2013.

[21] D Mueller, D A Gates, J E Menard, J R Ferron, and S A Sabbagh. Real-time Equilibrium Reconstruction and Isoflux Control of Plasma Shape and Position in the National Spherical Torus Experiment (NSTX) by PRINCETON PLASMA PHYSICS LABORATO. Technical Report August, 2004.

[22] Chiara Piron, Gabriele Manduchi, Paolo Bettini, Federico Felici, Claudio Finotti, Paolo Franz, Ondrej Kudlacek, Giuseppe Marchiori, Lionello Marrelli, J. M. Moret, Paolo Piovesan, Olivier Sauter, and Cesare Taliercio. Integration of the state observer RAPTOR in the real-time MARTe framework at RFX-mod. *Fusion Engineering and Design*, 123:616–619, 2017.

[23] F. Felici, O. Sauter, S. Coda, B. P. Duval, T. P. Goodman, J. M. Moret, and J. I. Paley. Real-time physics-model-based simulation of the current density profile in tokamak plasmas. *Nuclear Fusion*, 51(8), 2011.

[24] Federico Felici, Marco De Baar, and Maarten Steinbuch. A dynamic state observer for real-time reconstruction of the tokamak plasma profile state and disturbances. *Proceedings of the American Control Conference*, pages 4816–4823, 2014.

[25] D. P. O'Brien, J. J. Ellis, and J. Lingertat. Local expansion method for fast plasma boundary identification in JET. *Nuclear Fusion*, 33(3):467–474, 1993.

[26] D. MAZON, J. BLUM, C. BOULBE, B. FAUGERAS, M. BARUZZO, A. BOBOC, S. BREMOND, M. BRIX, P. DE VRIES, S. SHARAPOV, L. ZABEO, and JET-EFDA Contributors. Equinox: a Real-Time Equilibrium Code and Its Validation At Jet. (June):327–332, 2010.

[27] R. Albanese and F. Villone. The linearized CREATE-L plasma response model for the control of current, position and shape in tokamaks. *Nucl. Fus.*, 38(5):723–738, May 1998.

[28] R. Albanese, G. Calabrograve, M. Mattei, and F. Villone. Plasma response models for current, shape and position control at JET. *Fus. Eng. Des.*, 66–68:715–718, 2003.

[29] Farid Golnaraghi and Benjamin C Kuo. *Automatic Control Systems*. Pearson, 9^{nd} edition, 2010.

[30] T. Kailath. *Linear Systems*. Prentice Hall, Englewood Cliffs, 1980.

[31] Chi-Tsong Chen. *Linear System Theory And Design*. Oxford University Press, 3 edition, 1999.

[32] Norman Nise. *Control Systems Engineering*. John Wiley & Sons, Inc., 6 edition, 2011.

[33] Katsuhiko Ogata. *Modern Control Engineering*. Prentice Hall, 5 edition, 2009.

[34] Sigurd Skogestad and Ian Postlethwaite. 2 edition.

[35] William R. Spears. JT-60SA construction status. *IEEE Transactions on Plasma Science*, 2014.

[36] JT-60SA Team. Research objectives and strategy. Technical report, 2018. http://www.jt60sa.org/.

[37] N Cruz, G. De Tommasi, M Mattei, A Mele, Y Miyata, A Pironti, and T Suzuki. Control-oriented tools for the design and validation of the JT-60SA magnetic control system. *Control Engineering Practice*, 63:81–90, 2017.

[38] JT-60SA Team. Plant integration document. Technical report, 2017. https://users.jt60sa.org/?uid=222UJY.

[39] R. Albanese, R. Ambrosino, and M. Mattei. CREATE-NL+: A robust control-oriented free boundary dynamic plasma equilibrium solver. *Fus. Eng. Des.*, 96–97:664–667, Oct. 2015.

[40] R. Albanese, G. Ambrosino, M. Ariola, A. Cenedese, F. Crisanti, G. De Tommasi, M. Mattei, F. Piccolo, A. Pironti, F. Sartori, and F. Villone. Design, implementation and test of the XSC extreme shape controller in JET. *Fusion Engineering and Design*, 74(1-4):627–632, 2005.

[41] H. Anand et al. A novel plasma position and shape controller for advanced configuration development on the TCV tokamak. *Nucl. Fus.*, 57(12):126026, 2017.

[42] E. de la Luna et al. Recent Results on High-Triangularity H-Mode Studies in JET-ILW. In *26th IAEA Fusion Energy Conference*, Kyoto, Japan, October 2016.

[43] G. Ambrosino et al. Design and Implementation of an Output Regulation Controller for the JET Tokamak. *IEEE Trans. Control Syst. Tech.*, 16(6):1101–1111, Nov. 2008.

[44] M. Ariola and A. Pironti. The design of the eXtreme Shape Controller for the JET tokamak. *IEEE Control Sys. Mag.*, 25(5):65–75, Oct. 2005.

[45] H. Urano et al. Y. Miyata. Documents on inputs, outputs of ccs(cauchy condition surface) method. Technical report, 2018.

[46] H. Urano et al. Y. Miyata. Documents on inputs, outputs and control scheme of the qst magnetic controller. Technical report, 2018.

[47] G. De Tommasi et al. Shape Control with the eXtreme Shape Controller During Plasma Current Ramp-Up and Ramp-Down at the JET Tokamak. *J. Fus. Energy*, 33(2):149–157, 2014.

[48] H. Urano et al. Development of operation scenarios for plasma breakdown and current ramp-up phases in JT-60SA tokamak. *Fus. Eng. Des.*, 100:345–356, 2015.

[49] H. Meyer et al. Overview of progress in European medium sized tokamaks towards an integrated plasma-edge/wall solution. *Nuclear Fusion*, 57, 2017.

[50] Y. Miyata et al. Study of JT-60SA Operation Scenario using a Plasma Equilibrium Control Simulator. *Plasma and Fus. Res.*, 8:2405109–2405109, 2013.

[51] Y. Miyata, T. Suzuki, S. Ide, and H. Urano. Study of Plasma Equilibrium Control for JT-60SA using MECS. *Plasma and Fus. Res.*, 9:3403045–5, 2014.

A

EXTENDED CONTROL RESULTS

This appendix contains the corresponding plots of the ISTTOK discharges from table 5.2.1.

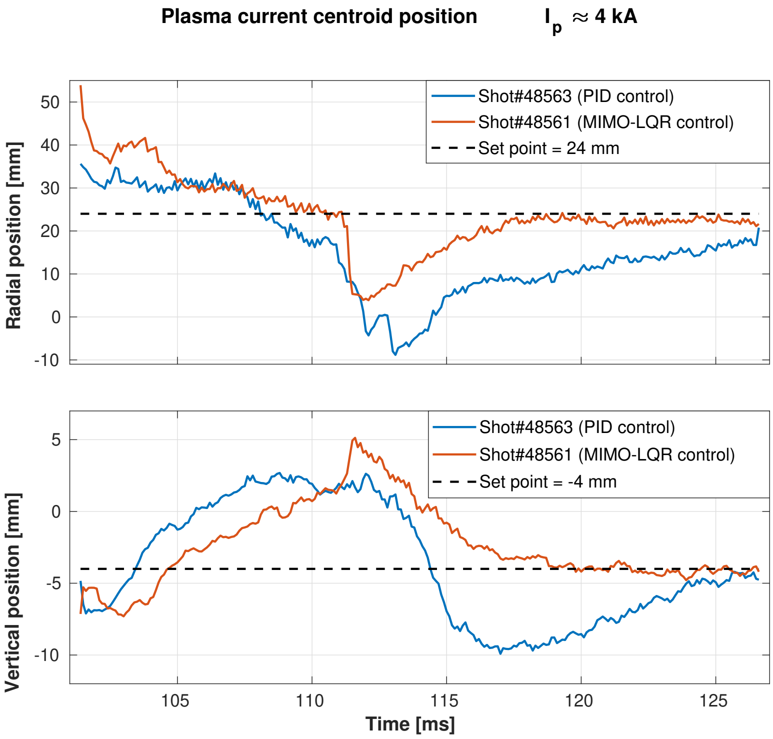

Figure A.1.: Plasma centroid position Shot# 48563 Shot# 48561

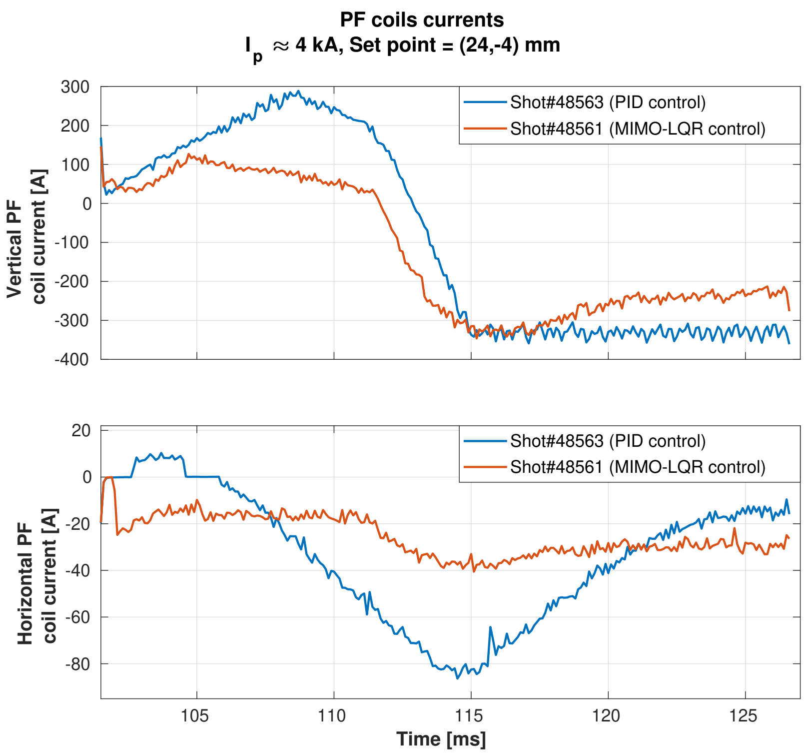

Figure A.2.: lalala Shot# 48563 Shot# 48561

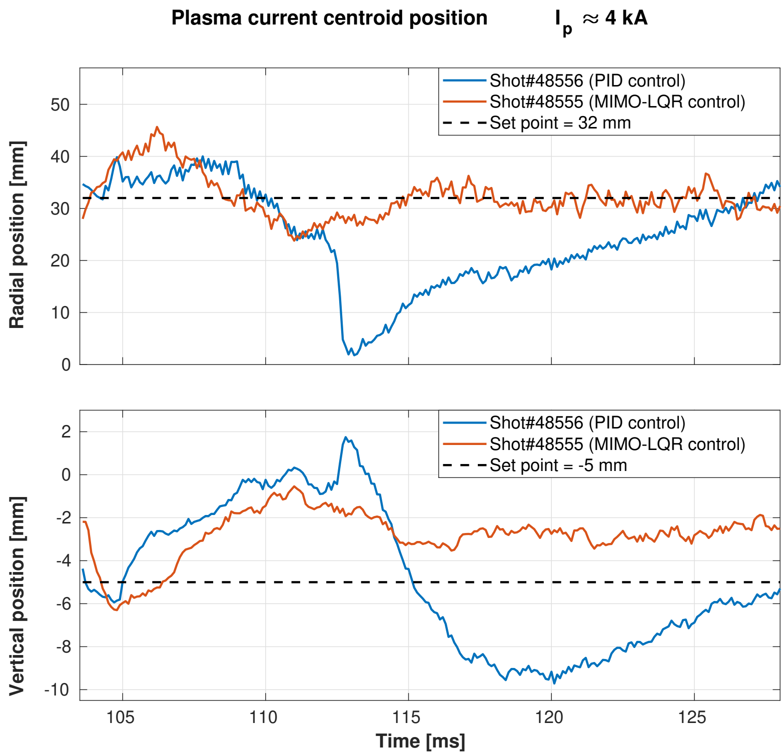

Figure A.3.: Plasma centroid position Shot# 48556 Shot# 48552

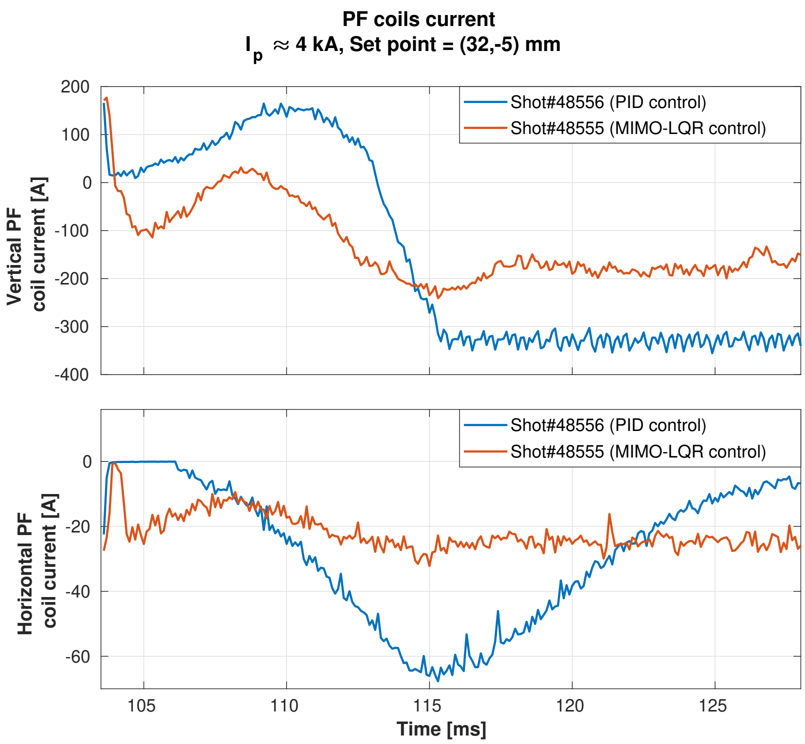

Figure A.4.: lalala Shot# 48556 Shot# 48552

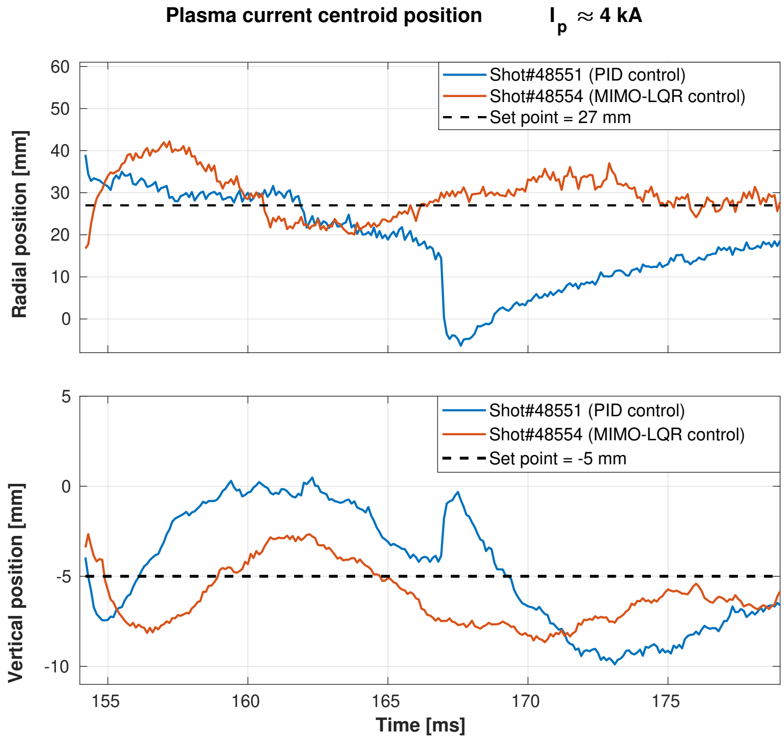

Figure A.5.: Plasma centroid position Shot# 48551 Shot# 48554

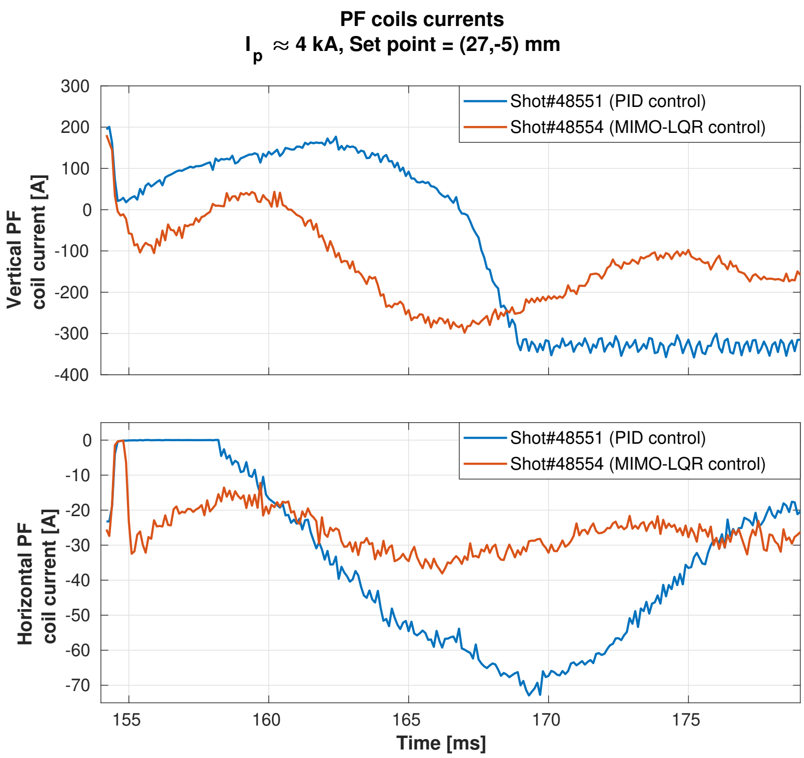

Figure A.6.: lalala Shot# 48551 Shot# 48554

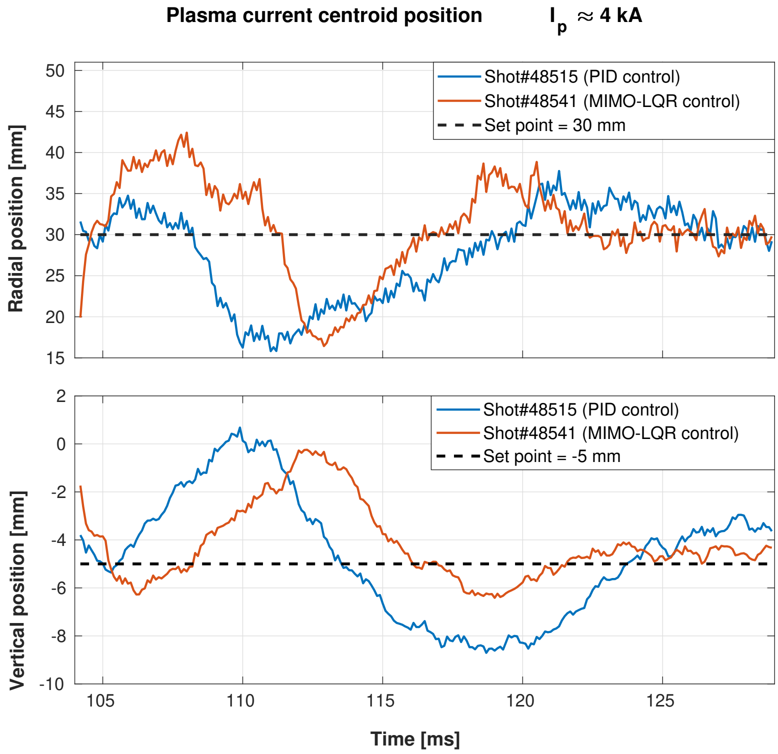

Figure A.7.: Plasma centroid position Shot# 48515 Shot# 48541

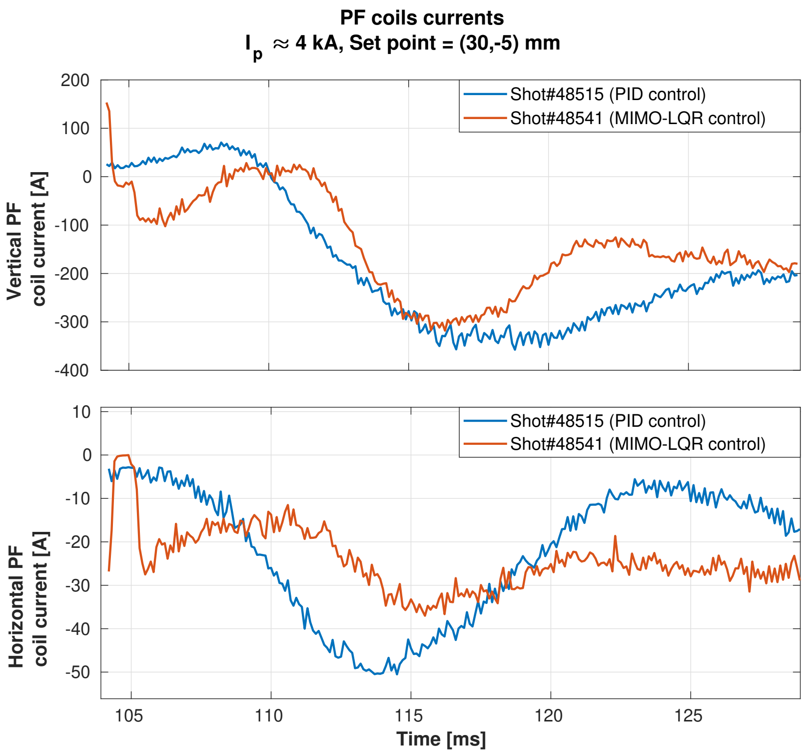

Figure A.8.: lalala Shot# 48515 Shot# 48541

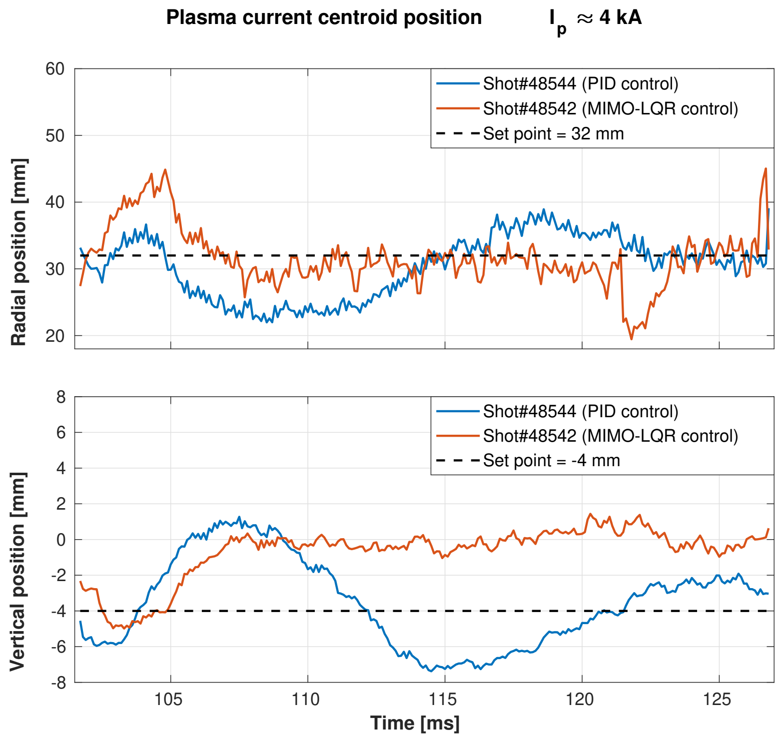

Figure A.9.: Plasma centroid position Shot# 48544 Shot# 48542

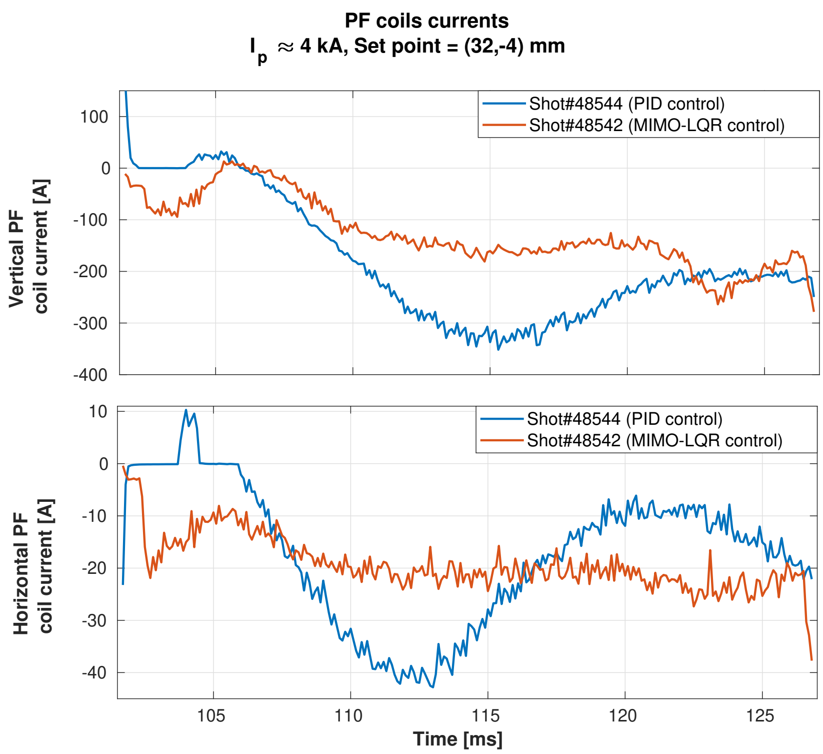

Figure A.10.: lalala Shot# 48544 Shot# 48542

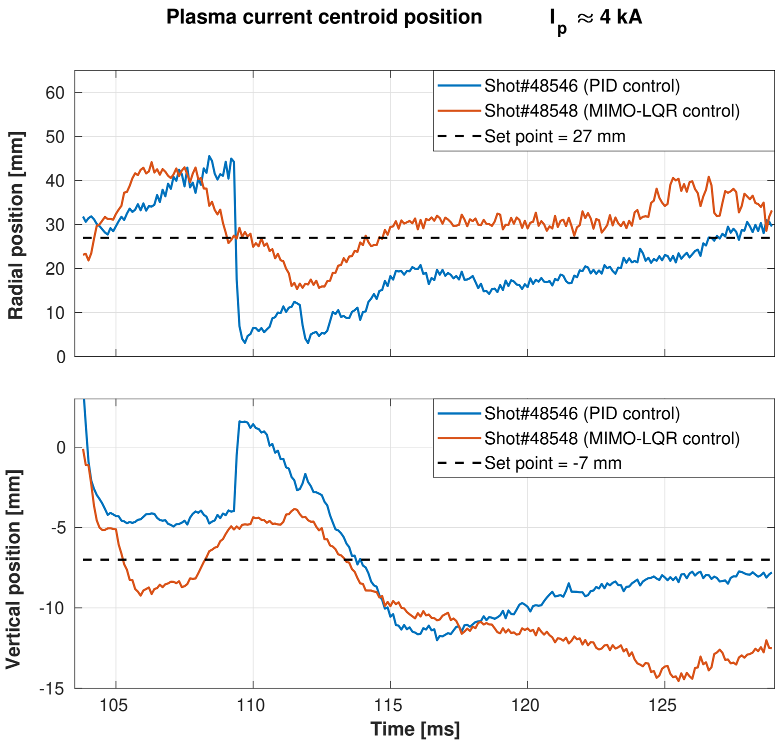

Figure A.11.: Plasma centroid position Shot# 48546 Shot# 48548

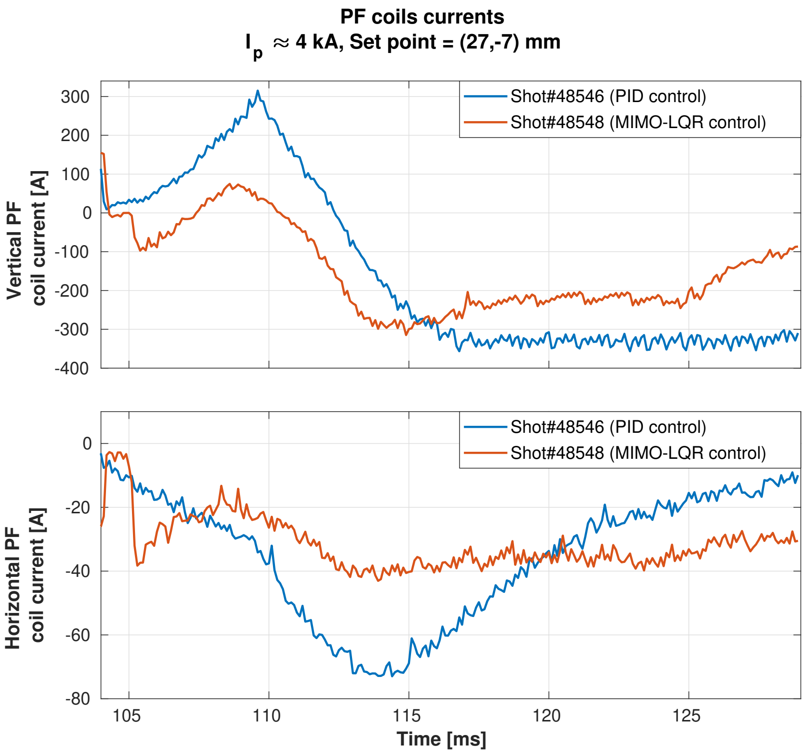

Figure A.12.: lalala Shot# 48546 Shot# 48548

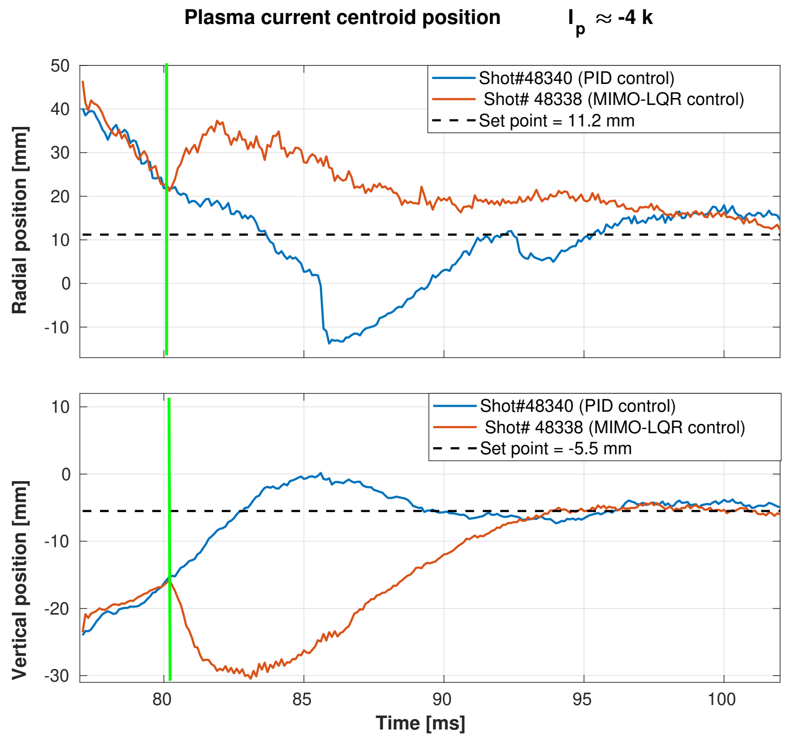

Figure A.13.: Plasma centroid position Shot# 48340 Shot# 48338

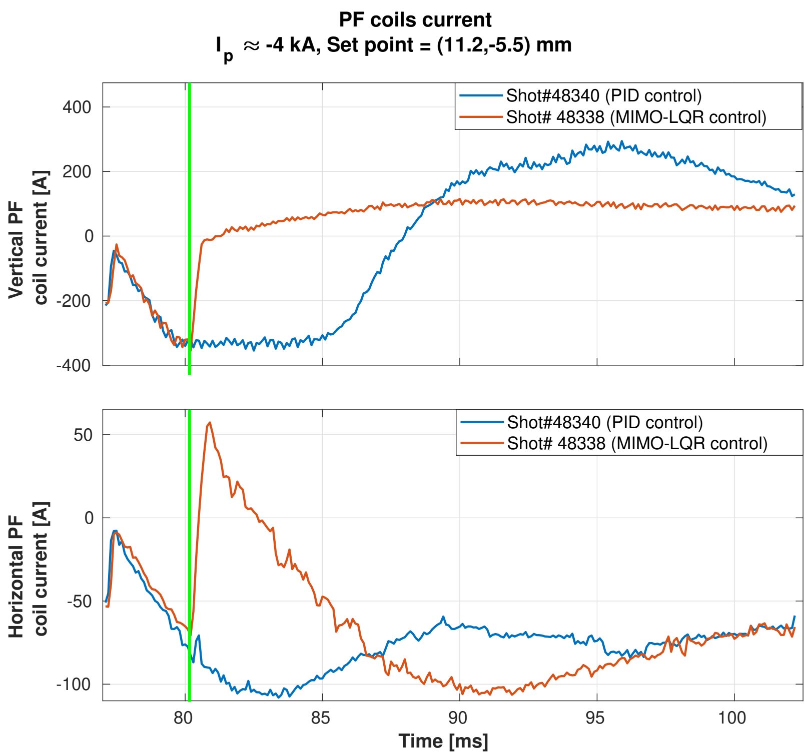

Figure A.14.: lalala Shot# 48340 Shot# 48338

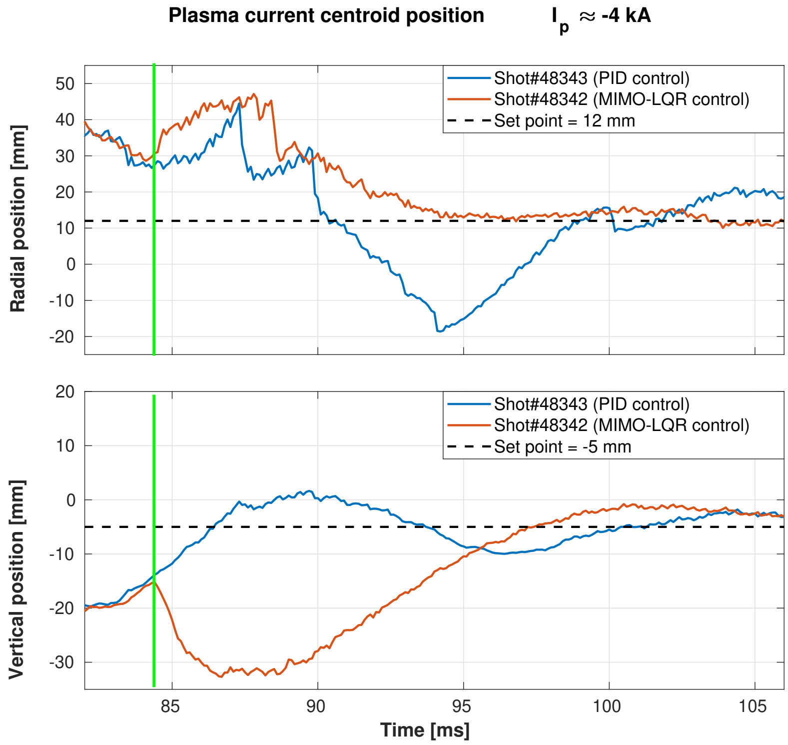

Figure A.15.: Plasma centroid position Shot# 48343 Shot# 48342

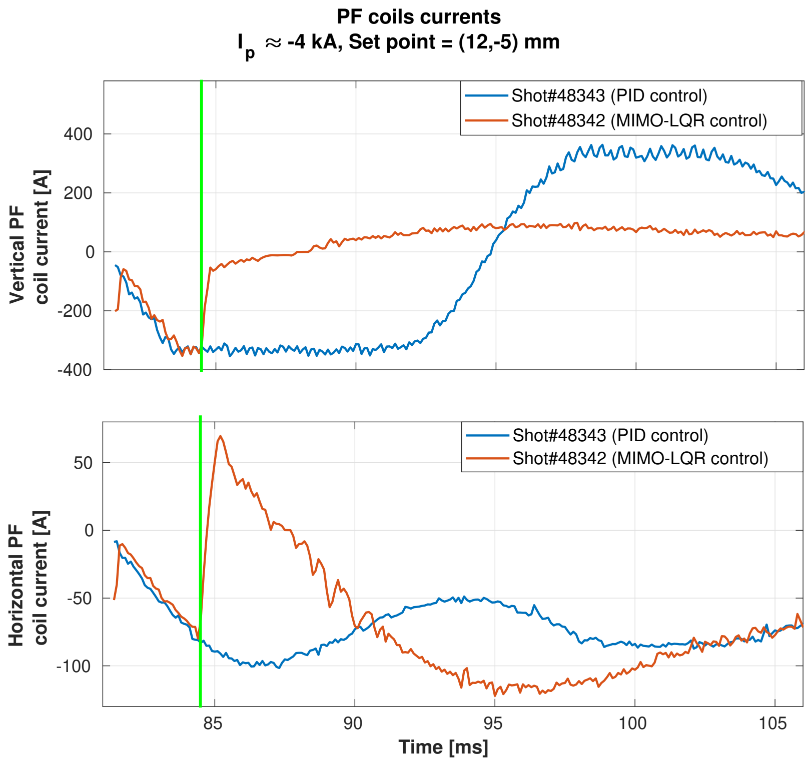

Figure A.16.: lalala Shot# 48343 Shot# 48342

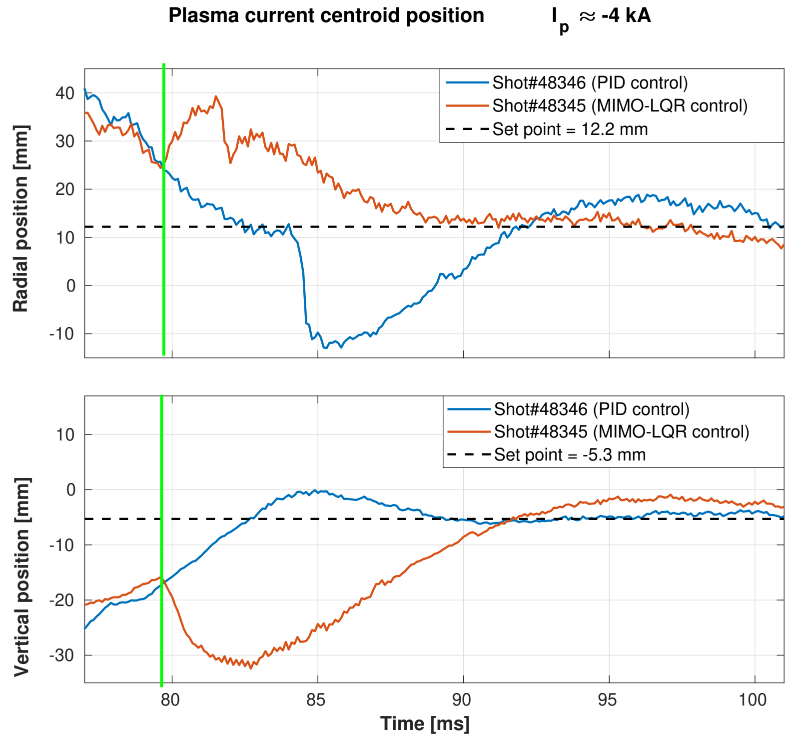

Figure A.17.: Plasma centroid position Shot# 48346 Shot# 48345

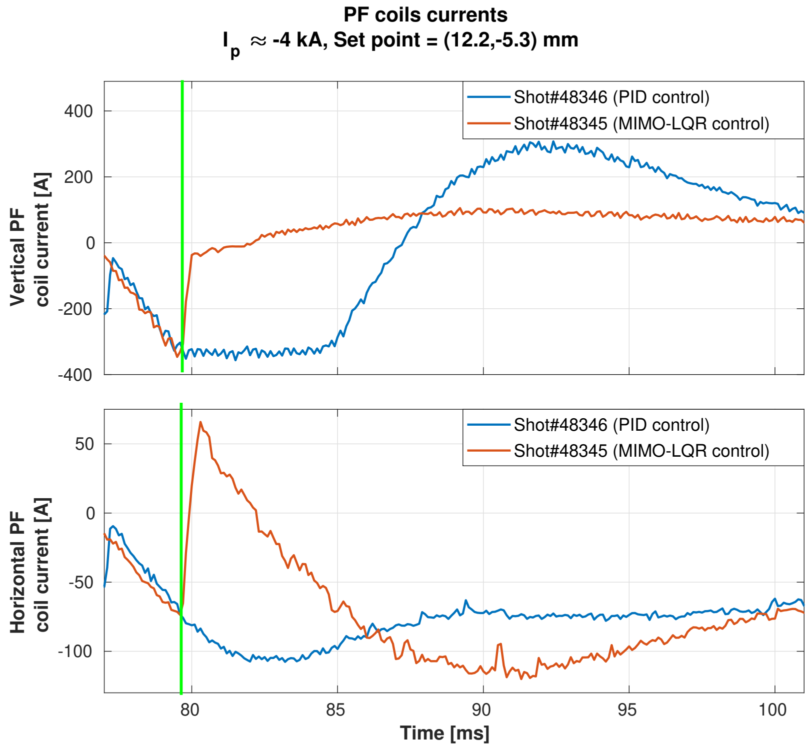

Figure A.18.: lalala Shot# 48346 Shot# 48345

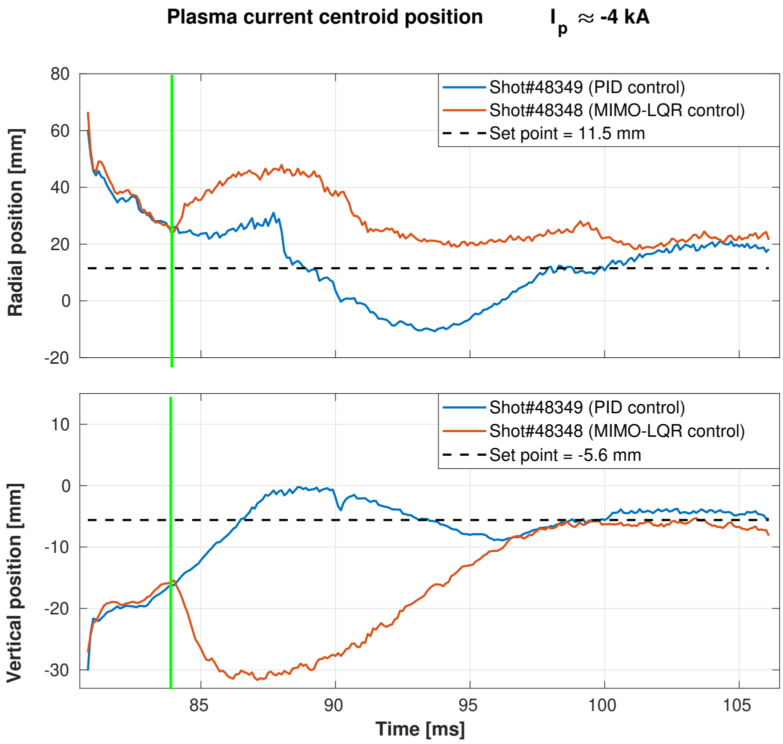

Figure A.19.: Plasma centroid position Shot# 48349 Shot# 48348

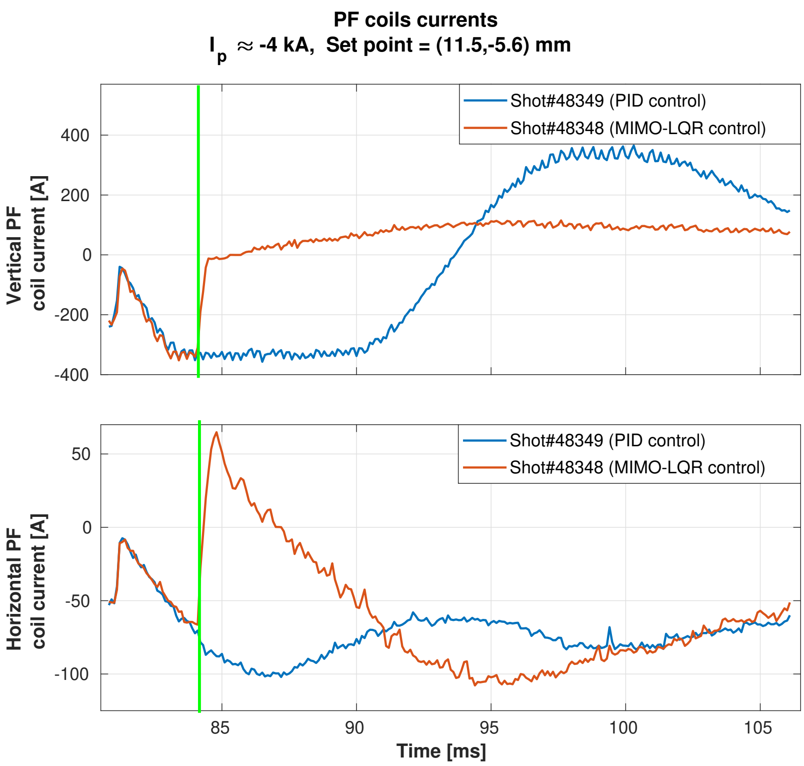

Figure A.20.: lalala Shot# 48349 Shot# 48348

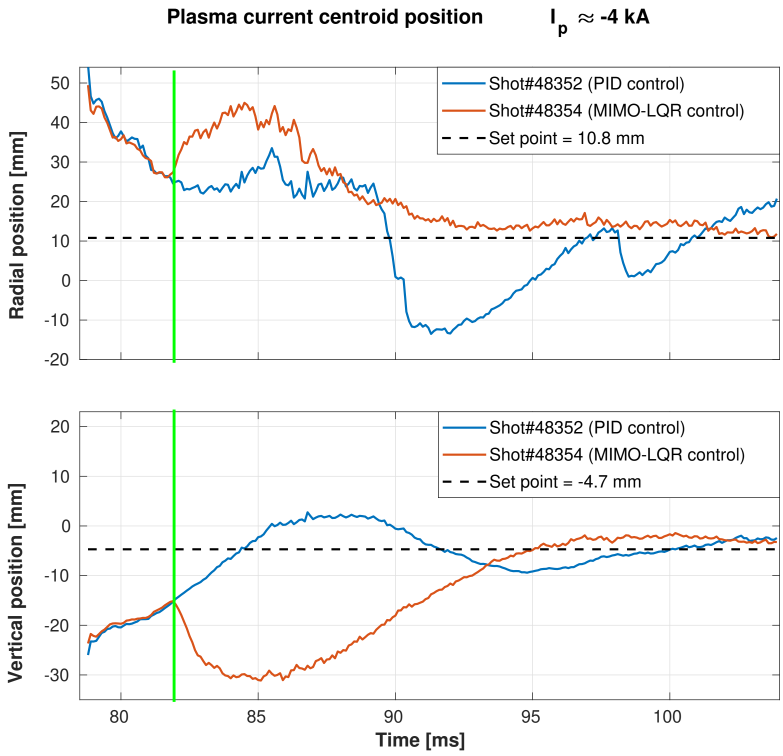

Figure A.21.: Plasma centroid position Shot# 48352 Shot# 48354

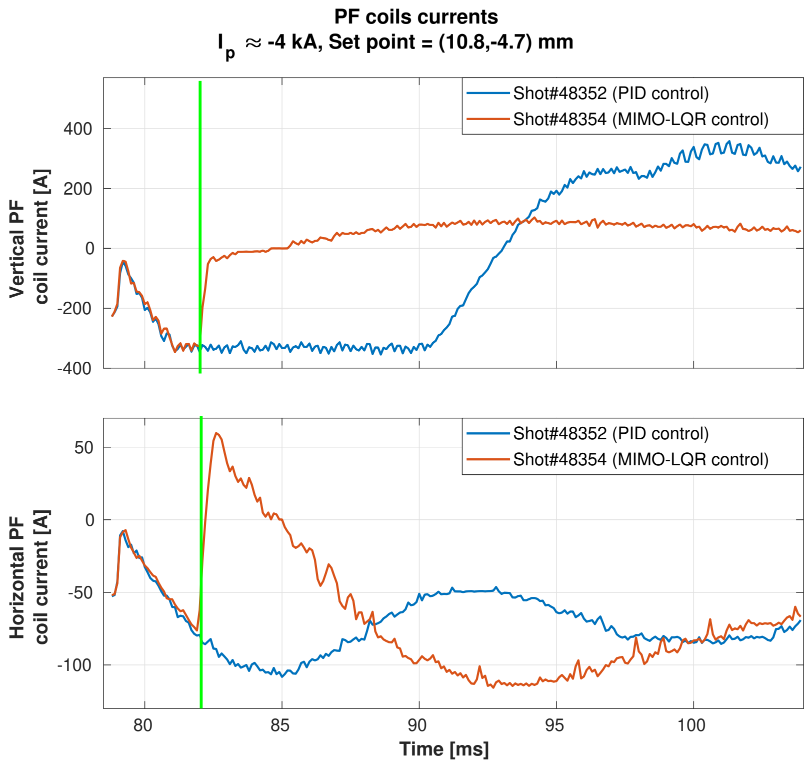

Figure A.22.: lalala Shot# 48352 Shot# 48354

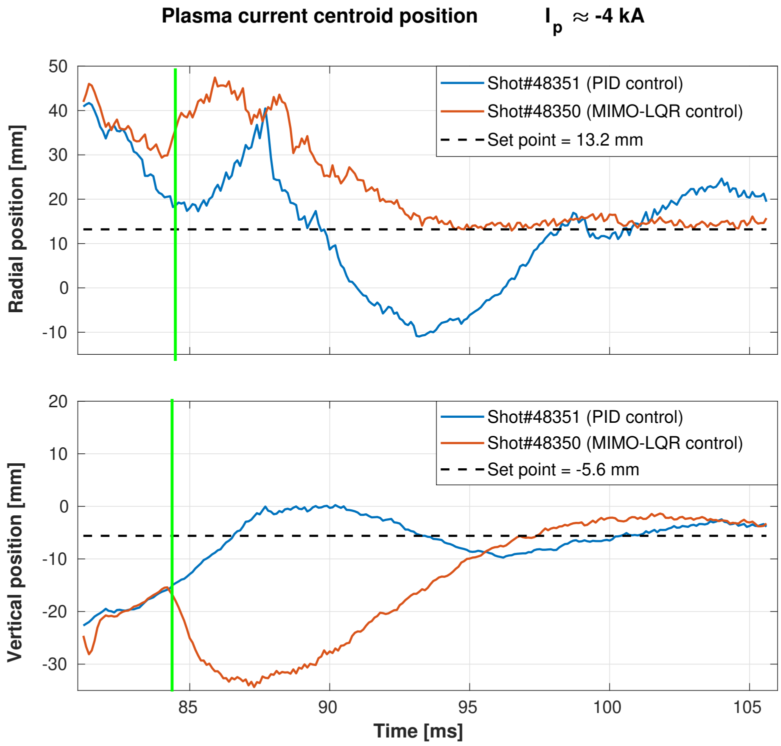

Figure A.23.: Plasma centroid position Shot# 48351 Shot# 48350

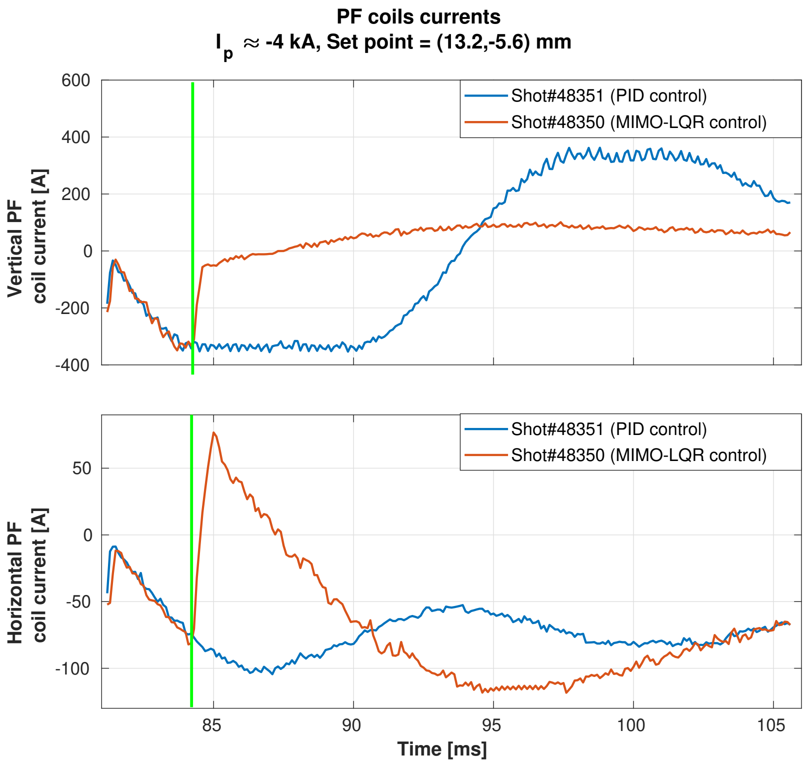

Figure A.24.: lalala Shot# 48351 Shot# 48350

B

JT60-SA PICTURES

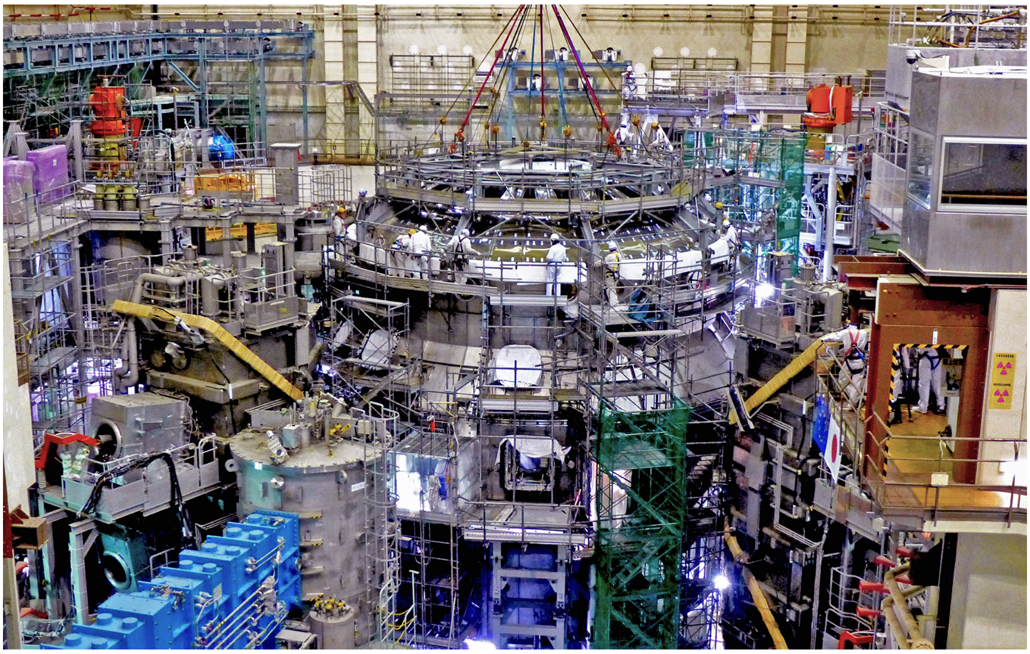

Figure B.1.: JT60-SA assembly when the cryostat top part was installed, 2018.

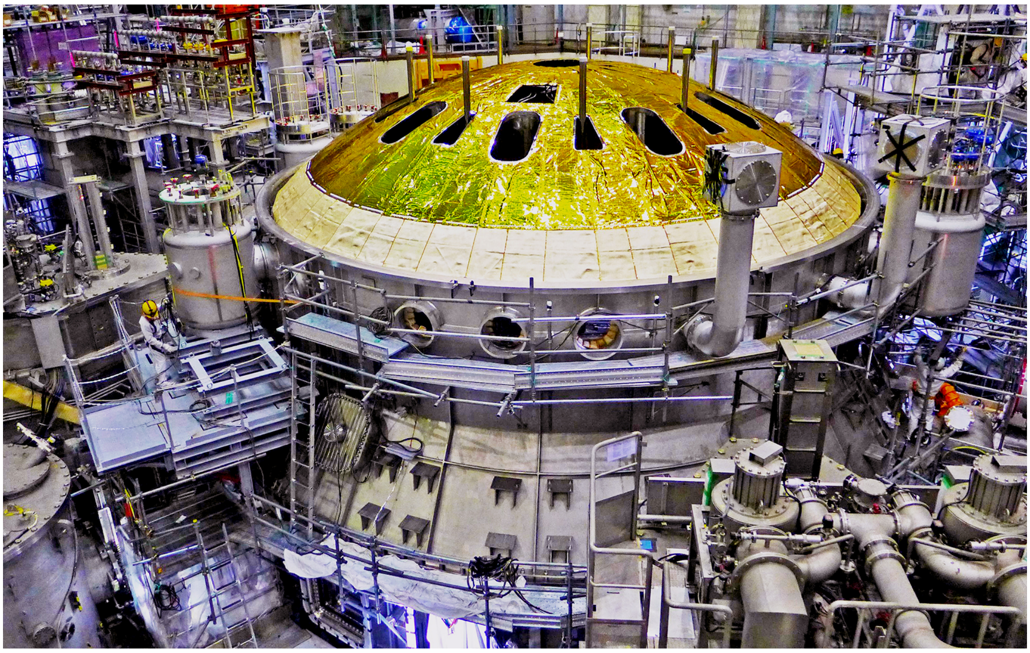

Figure B.2.: JT60-SA assembly in 2019.JT60-SA

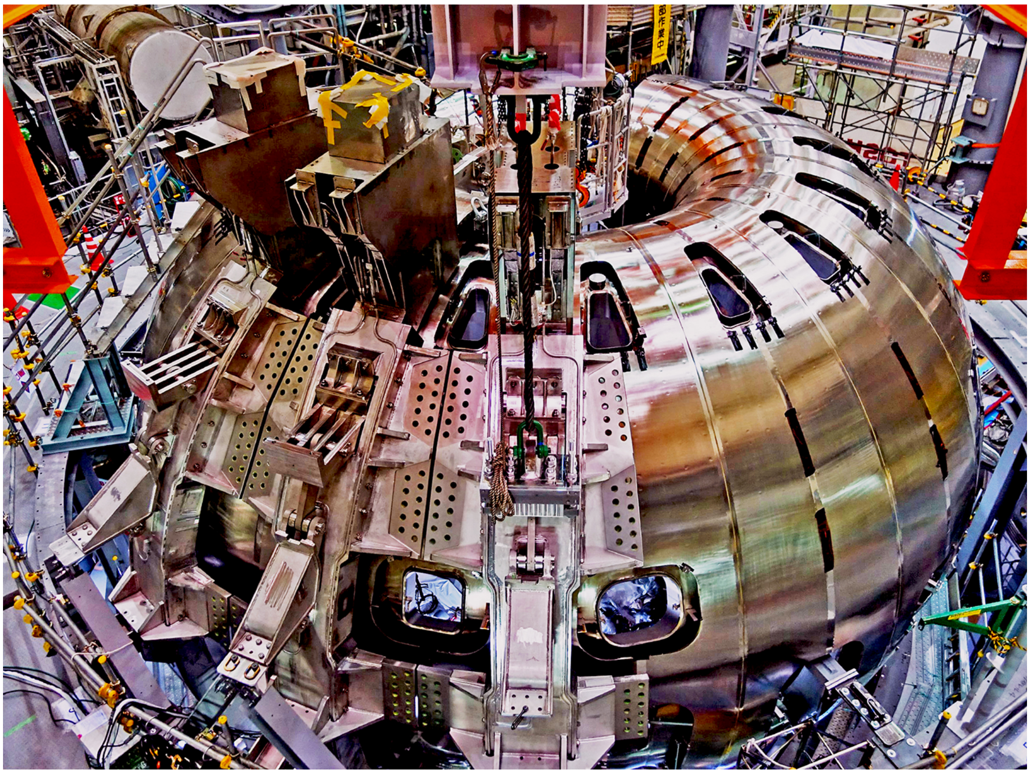

Figure B.3.: JT60-SA insertion of TF coil in 2018.

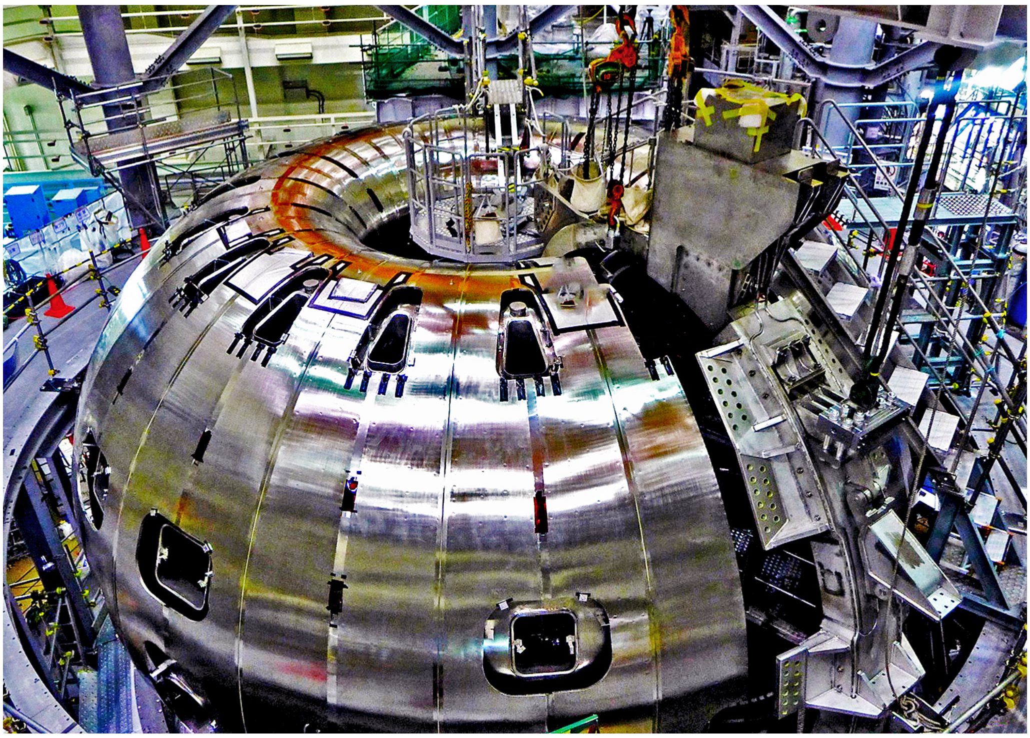

Figure B.4.: JT60-SA insertion of TF coil in 2018.

Figure B.5.: JT60-SA transportation of the first PF coil in 2019.